Atomic, Molecular, and Optical Physics in the Early Universe: From Recombination to Reionization

Simon C.O. Glover*, Jens Chluba[†], Steve R. Furlanetto[‡], Jonathan R. Pritchard[§], Daniel Wolf Savin[¶]

[*]Institut für Theoretische Astrophysik, Universität Heidelberg, Heidelberg, Germany
[†]Department of Physics and Astronomy, Johns Hopkins University, Baltimore, Maryland, USA
[‡]Department of Physics and Astronomy, University of California at Los Angeles, Los Angeles, California, USA
[§]Astrophysics Group, Imperial College, London, United Kingdom
[¶]Columbia Astrophysics Laboratory, Columbia University, New York, USA

Contents

Abstract

Our knowledge of the evolution of the early Universe hinges, in part, on our understanding of the underlying atomic, molecular, and optical (AMO) processes occurring during that epoch. Here we review the relevant AMO physics from when it first became important at a redshift of $z \sim 6000$, some 18,000 years after the Big Bang when electrons and ions began to recombine. The review continues through the formation of the first stars and galaxies and concludes after the radiation from these first objects has reionized the Universe at a $z \sim 10$, about a billion years after the Big Bang.

1. INTRODUCTION

Cosmology—the study of the origin, history, and fate of the Universe—is one of the oldest of the sciences, and yet the past few decades have seen a transformation of our understanding of the subject. We now have solid observational evidence that we live in an expanding Universe that is homogeneous and isotropic on the largest scales. We also know that visible matter and radiation make up only a small part of the total energy content of the Universe, with far more being contributed by dark matter—some form of nonbaryonic matter that does not interact electromagnetically—and by a cosmological constant or some other form of "dark energy." In addition, we now have a good understanding of how stars and galaxies first formed in this Universe and how they then affected their surroundings. Nevertheless, many questions remain unanswered. In this review, we explore the important role that atomic, molecular, and optical (AMO) physics plays in helping us to answer some of these questions.

As many of our readers will be unfamiliar with the field of cosmology, we will use the remainder of this introduction to briefly sketch out the main features of the current "standard model" of cosmology, the ΛCDM concordance model, which we define below. Space constraints limit our

treatment here to the barest essentials, and we refer any readers in search of a more detailed introduction to the excellent textbooks of Peacock (1999), Dodelson (2003), and Ryden (2003).

1.1 The Expanding Universe

Our cosmological standard model is based on two fundamental assumptions: that our Universe is isotropic, that is, the same (on average) in all directions, and that our place in the Universe is not particularly special. Together, these assumptions imply that the Universe must also be homogeneous when averaged on large scales. Observational tests of homogeneity and isotropy give strong support for both, giving us confidence that our basic model is correct.

Einstein's theory of general relativity (GR) tells us that mass, energy, and momentum all cause space to curve, and that this is responsible for the phenomenon that we perceive as gravity. In a homogeneous, isotropic Universe, the value of this curvature averaged on very large scales must be the same everywhere, meaning that there are only three possibilities for the "global" geometry of space: it can be positively curved, meaning that the angles of a triangle add up to more than 180° and that parallel lines eventually meet; it can be negatively curved, meaning that the angles of a triangle add up to less than 180° and that parallel lines diverge; or it can be flat. In practice, observations of the cosmic microwave background (CMB) strongly suggest that the Universe that we live in is flat (Hinshaw et al., 2013; Planck Collaboration et al., 2013).

Within our homogeneous, isotropic, and flat Universe, we have an additional degree of freedom. We can allow the distances between points to expand or contract as time passes, provided that the amount of expansion or contraction depends only on the current time and not on our position in space. Although it may seem simpler to assume that the distances between widely separated points do not change, GR tells us that this is an unstable situation, and that the slightest perturbation will lead to expansion or contraction. Moreover, it is easy to show that if the Universe is contracting, the light from distant galaxies will be shifted to shorter wavelengths (blueshifted) before reaching us, while if it is expanding, the light will be shifted to longer wavelengths (redshifted). The fact that we observe distant galaxies to be redshifted is therefore *prima facie* evidence that the Universe is presently expanding.

We can quantify the expansion of the Universe in terms of a time-dependent scale factor $a(t)$, where t is time and $a = 1/(1+z)$ is the cosmic scale factor normalized to unity at the present-day redshift of $z = 0$. In a homogeneous, isotropic, and flat Universe, the evolution of a is governed by

$$H^2 = H_0^2 \left[\Omega_r a^{-4} + \Omega_m a^{-3} + \Omega_\Lambda \right]. \tag{1}$$

Here $H \equiv \dot{a}/a$ is a quantity known as the Hubble parameter, the dot denotes a time derivative, and H_0 is the value of H at the present time, often referred to as the Hubble constant, and $\dot{a}$ the time derivative of a. The quantities Ω_r, Ω_m, and Ω_Λ are dimensionless density parameters, defined as

$$\Omega_m \equiv \frac{\rho_m}{\rho_{crit}}, \quad \Omega_r \equiv \frac{\rho_r}{\rho_{crit}}, \quad \Omega_\Lambda \equiv \frac{\Lambda}{3H_0^2}. \tag{2}$$

The term ρ_m denotes the present-day mean mass density of nonrelativistic matter (i.e., matter with thermal and bulk velocities that are both much less than the speed of light) and ρ_r denotes the present-day mean density of relativistic matter and radiation, expressed in units of mass density. Since the CMB makes the largest contribution to ρ_r, the latter is usually referred to simply as "radiation," although in practice the contribution from relativistic neutrinos is also significant. The critical density needed to halt the expansion of the Universe, ρ_{crit}, is given by

$$\rho_{crit} \equiv \frac{3H_0^2}{8\pi G}, \tag{3}$$

where G is the gravitational constant. Finally, Λ denotes the cosmological constant. This is a constant term that can be added to the gravitational field equations without significantly affecting the theory's predictions on scales where it has already been tested. In Eq. (1), Λ behaves in the same fashion as a fluid with a negative equation of state. The physics responsible for the appearance of this term remains extremely unclear, but its presence in our models seems to be unavoidable if we are to fit all of the available observational data.

By combining information from a variety of different observations, in particular the measurements of fluctuations in the CMB made by the *WMAP* and *Planck* satellites (Hinshaw et al., 2013; Planck Collaboration et al., 2013), we have been able to accurately determine the values of the main cosmological parameters. In this review, when specific values are required, we use the present-day values determined by *WMAP*, namely:

$$H_0 = 69.7 \, \text{km s}^{-1} \, \text{Mpc}^{-1},$$
$$\Omega_m = 0.282,$$
$$\Omega_\Lambda = 0.718.$$

The contribution to Ω_r made by photons can be constrained by accurate measurements of the CMB temperature and is found to be (Fixsen and Mather, 2002)

$$\Omega_{\text{r,photons}} = 5.08 \times 10^{-5}. \tag{4}$$

Measurements of the CMB anisotropy power spectrum constrain the contribution to Ω_{r} made by relativistic neutrinos to be approximately (Planck Collaboration et al., 2013)

$$\Omega_{\text{r,neutrinos}} \simeq 3.8 \times 10^{-5}. \tag{5}$$

Therefore, the total density in radiation at the present time is approximately

$$\Omega_{\text{r}} = \Omega_{\text{r,photons}} + \Omega_{\text{r,neutrinos}} = 8.9 \times 10^{-5}. \tag{6}$$

From Eq. (1), we see that these values imply that the expansion of the Universe at the present time is dominated by the effects of the cosmological constant. However, if we look back in time, so that a decreases, we see that the influence of the matter and radiation components becomes increasingly important. The expansion of the Universe first became dominated by the cosmological constant at the time when the scale factor satisfied

$$a_\Lambda = \left(\frac{\Omega_{\text{m}}}{\Omega_\Lambda}\right)^{1/3} \simeq 0.73. \tag{7}$$

We can also write this in terms of a redshift z. Light emitted by a galaxy at a time when the scale factor equaled a_{em} will have redshifted by an amount $z_{\text{em}} = a_{\text{em}}^{-1} - 1$ by the time that it reaches us, that is, its wavelength will have increased by a factor of $(1 + z_{\text{em}})$. The redshift at which the effects of matter and the cosmological constant are approximately equal is therefore $z_\Lambda \simeq 0.37$.

As we move to much higher redshifts, the influence of the cosmological constant becomes negligible, but the influence of the radiation grows faster than that of the nonrelativistic matter. Matter and radiation contribute equally to H at the redshift of matter–radiation equality,

$$z_{\text{eq}} = \frac{\Omega_{\text{m}}}{\Omega_{\text{r}}} \simeq 3200. \tag{8}$$

At $z > z_{\text{eq}}$, the Universe is dominated by radiation, while at $z_{\text{eq}} > z > z_\Lambda$ it is dominated by matter.

1.2 The Thermal History of the Universe

The radiation energy density in the Universe is dominated by the CMB, which has a spectrum which is extremely close to that of a perfect blackbody (Fixsen and Mather, 2002). As the Universe expands, this radiation field retains its perfect blackbody shape. However, its temperature decreases with decreasing z as $T_{\text{r}} \propto (1 + z)$. At redshifts $z > 100$, efficient transfer of energy via Compton scattering keeps the matter temperature

very close to the radiation temperature. At lower redshifts, this scattering becomes too slow to keep the two temperatures together, and the matter (i.e., gas) temperature starts to evolve as $T \propto (1 + z)^2$, due simply to adiabatic expansion (Zeldovich et al., 1968).

We therefore see that the Universe must have started in an extremely hot, dense state, and that since then it has been progressively evolving toward lower densities and lower temperatures. The change in the mean temperature of the Universe over time leads to a series of changes in the composition of the matter within it. Of these changes, the two that are most relevant for our current review are primordial nucleosynthesis, which we discuss briefly here, and recombination, which is the topic of Section 2 of this review.

In the very early Universe, when $k_B T_r > 80\,\text{keV}$, where k_B is the Boltzmann constant, all of the protons and neutrons in the Universe existed in the form of free particles, as any heavier nuclei that did manage to form by fusion (deuterium, tritium, ^{3}He, ^{4}He, etc.) were rapidly destroyed by gamma-ray absorption. However, once the radiation temperature dropped below this value, which occurred a few minutes after the beginning of the Universe, these heavier nuclei could survive, and the process known as primordial nucleosynthesis could begin. Protons and neutrons first fused to form deuterium, and from there, most of the neutrons went on to form helium. A small amount of this helium was then converted to ^{7}Li, but the production of heavier elements was greatly hampered by the fact that no stable elements with atomic weights $A = 5$ or 8 exist. Most of the neutrons therefore remained in the form of helium. Detailed calculations show that this process naturally leads to an elemental composition of primordial matter that is roughly 76% hydrogen and 24% helium, by weight (Cyburt et al., 2003; Olive et al., 2000; Pospelov and Pradler, 2010; Walker et al., 1991). In addition, trace amounts of other light elements (deuterium, ^{3}He, and ^{7}Li) are also produced, with abundances that depend sensitively on the baryon-to-photon ratio η. Measurements of the primordial abundances of these light elements therefore allow us to constrain this value. Measuring the current CMB temperature allows us to determine with high accuracy the current number density of photons, and theory tells us that this evolves with redshift as $n_\gamma \propto (1 + z)^3$. We can therefore convert our constraint on η into a constraint on the present-day ratio of the baryon density to the critical density Ω_b. The value we derive from this is consistent with the measurement that we can make using the observed CMB fluctuations, namely $\Omega_b = 0.0461$ (Hinshaw et al., 2013).

1.3 The Need for Dark Matter

If we compare Ω_b with the value quoted earlier for the mean matter density, $\Omega_m = 0.282$, we see that there is a large discrepancy. Baryons can make up no more than ~16% of the total matter density. The way that we resolve this discrepancy is to posit that the remaining matter is actually some form of nonbaryonic matter. Moreover, if this matter could interact electromagnetically, we would already have detected it; since we have not, we can conclude that it does not interact in this way with baryons or photons. We therefore term this curious nonbaryonic component "dark" matter.

The dark matter hypothesis explains why Ω_b and Ω_m differ, and also provides a simple explanation for two other puzzles. The fluctuations that we see in the CMB probe the state of the Universe at a redshift $z \sim 1000$, and the small size of these fluctuations tells us that the distribution of baryons and radiation was still extremely smooth at this point. In fact, the distribution is too smooth to explain the later growth of dense structures such as galaxies and clusters of galaxies if the Universe contained only matter and radiation. The presence of dark matter allows us to avoid this problem. Since the dark matter does not couple directly to the radiation, but only affects it indirectly via gravity, the perturbations in the dark matter component at $z \sim 1000$ can be larger than those in the baryonic matter or radiation components without violating the CMB observational constraints. Larger perturbations require less time to grow and hence allow galaxies and larger structures to form earlier, in agreement with what we observe.

The existence of some dark matter component was already suggested by measurements of the mass–to–light ratio for the Coma galaxy cluster carried out by Zwicky in 1933 (Zwicky, 1933, 1937). By comparing the virial mass to the mass seen in galaxies, Zwicky found that the gravitating component of the Coma cluster must be about 400 times greater than expected from the galaxies' luminosities. While this value is significantly lower in modern versions of these early measurements, the basic conclusion remains the same (Carlberg et al., 1996, 1997).

The other puzzle that dark matter solves is the mystery of galactic rotation curves. In the late 1970s, Vera Rubin and others were able to measure the orbital velocity of gas at various distances from the centers of spiral galaxies (see, e.g., Sofue and Rubin, 2001, for a good review of this work). They showed that at large distances from the center, the orbital velocity becomes approximately constant (i.e., the rotation curve becomes flat). This is not what one would expect if the gravitational potential of the galaxy was determined only by the contribution from the visible stars

and gas. However, it can be explained very easily if one assumes that the visible parts of galaxies are surrounded by a much larger halo of dark matter. Moreover, the amount of dark matter that is required is consistent with the amount that we need to explain the discrepancy between Ω_b and Ω_m.

Although we do not know what this dark matter actually is, we can put some constraints on its properties. It cannot interact strongly with radiation or with ordinary baryonic matter. We also know from the clustering pattern of galaxies that it must have a low velocity dispersion, leading to it being termed "cold" dark matter or CDM for short. When we refer to the ΛCDM model, we therefore mean a model in which there is a nonzero cosmological constant (Λ) and a significant amount of mass present in the form of this CDM.

1.4 The Role of AMO Physics

In the very early Universe, during the Plasma Era, the temperature is too high to allow bound atoms or molecules to exist. As we move to redshifts of $z \lesssim 6000$, this starts to change and AMO physics becomes important. First, neutral hydrogen and helium atoms form in a process known as cosmological recombination (Section 2). Next, these atoms and the remaining ions and free electrons can take part in chemical reactions, either in the diffuse pregalactic gas (Section 3) or in the much denser gas that begins to accumulate once the first protogalaxies start to form (Section 4). As we will see later, the formation within these early protogalaxies of the first stars (so-called Population III stars) depends sensitively on the amount of molecular hydrogen that is available, and hence AMO physics plays an important role in determining the nature of the very first stars to form. The epoch between hydrogen recombination at $z \sim 1000$, which formed the CMB, and the light from the first stars is sometimes called the Dark Ages due to the lack of any luminous objects during this time. At $z \lesssim 100$–200, the matter and radiation temperatures decouple and it becomes possible to probe the evolution of the Universe by studying the emission or absorption produced by the 21-cm hyperfine structure line of neutral hydrogen (Section 5). Finally, the first generation of stars, plus the subsequent generation that follows it (Population II stars), produce large amounts of ionizing radiation. This radiation eventually reionizes the Universe, converting the intergalactic gas back into a highly ionized plasma (Section 6).
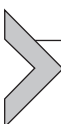
1.5 Distance Measurements

Because of the expansion of the Universe, distances in cosmology require some care: the separation between two objects fixed relative to the rest frame

of the Universe evolves over time. The separation, as measured at a single instant in time, is known as the *proper* or *physical* distance. This is convenient for an observer situated at that time, but we must bear in mind that the proper distance will evolve as the Universe expands. The *comoving* distance, on the other hand, remains constant with time: if we imagine overlaying a grid on the Universe and allowing that grid to expand with space–time itself, the comoving distance would be the number of grid cells separating two points. Operationally, we measure the spacing of the comoving grid using present-day coordinates. Thus, the comoving distance between two objects is the distance between them as it would be measured today, if they remained fixed relative to the grid between the time of interest and today.

1.6 Acronyms and Variables

Acronyms and variables used throughout this chapter are given in Appendix A and Appendix B, respectively. Concerning the variables, this review brings together many different subfields within AMO physics and astrophysics. The usage of symbols is not uniform across these areas. To maximize the ease of going from this review to the original literature, we have attempted to keep the notation particular to each subfield. This results in some variables being used for multiple quantities or multiple variables being used for the same quantity. Appendix B defines all variables and lists the sections where each is used.

2. COSMOLOGICAL RECOMBINATION

The physical ingredients to describe the cosmological recombination process are amazingly simple and well understood. This allows us to consider a large variety of processes, which in most other astrophysical and laboratory environments are completely negligible. We can do this in extreme detail, thereby challenging our understanding of atomic physics, radiative transfer, and cosmology. These processes have important and potentially measurable consequences on the CMB energy spectrum and temperature anisotropies. This section describes the physics of cosmological recombination,[1] giving a taste of some of the significant recent refinements introduced to the pioneering works on this problem originally carried out by Zeldovich et al. (1968) and slightly later by Peebles (1968).

---

[1] People frequently complain that it should actually be called "cosmological combination," as this never happened before. However, it seems the jury decided against this.

2.1 What Is Cosmological Recombination All About?

Within the standard Big Bang picture, after the end of the electron–positron annihilation epoch ($z \lesssim 2 \times 10^6$) and before $z \gtrsim 10^4$, the Universe was sufficiently hot and dense that initially all the baryonic matter was completely ionized. On the other hand, it is clear that at later stages the medium was practically neutral, at least before the Universe was reionized by the first sources of energetic photons igniting close to redshift $z \sim 10$. The transition from the plasma to neutral phase is what is commonly called the cosmological recombination era, studies of which help to constrain the early conditions of the Universe.

2.1.1 Initial Conditions and Main Aspect of the Recombination Problem

Before talking in more detail about the three recombination epochs (Fig. 1), let us briefly look at the main physical condition during recombination.
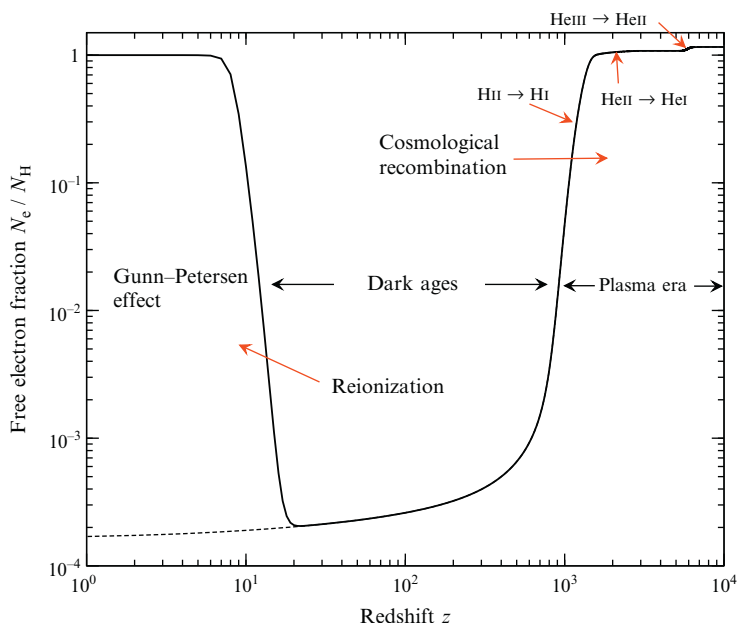
Fig. 1. Sketch of the cosmological ionization history as a function of redshift z. Here N_e is the number density of free electrons and N_H the number density of hydrogen nuclei. At high z, the Universe was completely ionized. As it expanded and cooled down, it went through several stages of recombination, starting with He III $\rightarrow$ He II recombination ($z \sim 2000$), and ending with the recombination of hydrogen ($z \sim 1000$). At low redshift ($z \lesssim 10$), the medium eventually was reionized by the first sources of radiation that appeared in the Universe. *Adapted from Sunyaev and Chluba (2009).*

Throughout recombination the primordial plasma can be thought of as completely isotropic and homogeneous, without any of the complications added much later when the first structures formed at $z \sim 20$. Furthermore, the medium is globally neutral and expanding at a rate that can be computed using a small set of precisely known cosmological parameters. The baryons in the Universe are immersed in a bath of CMB blackbody photons, which today have a temperature of $T_0 = 2.726\,\mathrm{K}$ and a number density of $N_{\gamma,0} \sim 411\,\mathrm{cm}^{-3} \propto T_0^3$ (Fixsen et al., 2011). The total number of available electrons is mainly determined by the abundance of hydrogen and helium. Although Big Bang Nucleosynthesis produced trace amounts of the light elements D, ^{3}He, and Li at $z \sim 2 \times 10^8$, their contributions to the electron number are insignificant during this epoch (Ali-Haïmoud et al., 2010; Switzer and Hirata, 2008b). Furthermore, throughout recombination there are no significant amounts of heavy metals or dust. At this epoch, the number density of hydrogen nuclei $N_{\mathrm{H}} \approx 1.9 \times 10^{-7}(1 + z)^3\,\mathrm{cm}^{-3}$ and the corresponding fractional number density of helium nuclei is $N_{\mathrm{He}}/N_{\mathrm{H}} \approx 8\%$. These numbers yield a helium mass fraction of $Y_{\mathrm{p}} = 0.24$, a ratio for the free electrons per baryon of 0.88, and ~ 1.16 electrons per hydrogen nucleus, where $\sim 2 \times 8\%$ of the electrons are contributed by primordial helium. This summarizes the main factors that make the cosmological recombination problem so simple, but also very special, as we show below.

2.1.2 The Three Stages of Recombination

As the Universe slowly expands and cools down, the free electrons in the plasma start recombining to form neutral atoms, marking the beginning of cosmological recombination. At first, only tiny amounts of singly ionized helium exist in equilibrium with fully ionized helium until the temperature of the Universe decreases to about 16,400 K, some 18,000 years after the Big Bang. At that time, doubly ionized helium ions capture a free electron, recombining to He II. Meanwhile hydrogen and neutral helium atoms remained ionized due to ionizations by the ubiquitous CMB photons. The transition from He III $\rightarrow$ He II happened rather rapidly, with the abundance of He III and He II ions closely described by the corresponding Saha equation (e.g., Seager et al., 2000) and only very small corrections caused by nonequilibrium effects (Switzer and Hirata, 2008b).

As the Universe expands further, it next passes through the epoch of neutral helium recombination, at a redshift of $z \sim 2000$, roughly 130,000 years after the Big Bang. At this time, the temperature of the medium was $\sim$5500 K, which is very similar to the temperature in the photosphere of

our Sun. However, the free electron number density of about $1600\,\mathrm{cm}^{-3}$ is orders of magnitudes smaller than in the Solar photosphere and closer to densities found in many H II regions. In contrast to He III $\rightarrow$ He II recombination, neutral helium forms much more slowly, pretty far from Saha equilibrium. The main reason for this delay is that the energetic photons produced by recombination continue to interact with neutral helium atoms, so that He I remained singly ionized significantly longer.

In the final stage, the Universe entered the epoch of hydrogen recombination. When the temperature of the medium had dropped to about 3500 K at $z \sim 1300$, half of all hydrogen atoms had already recombined. The remaining free electron and proton number densities were $N_\mathrm{e} = N_\mathrm{p} \sim 230\,\mathrm{cm}^{-3}$. The recombination of hydrogen also proceeded far out of equilibrium (see Fig. 2). Again, the energetic photons produced by recombination delayed the relaxation of captured electrons into the ground state. However, hydrogen eventually finished recombining some 700,000–800,000 years after the Big Bang, when the number density of
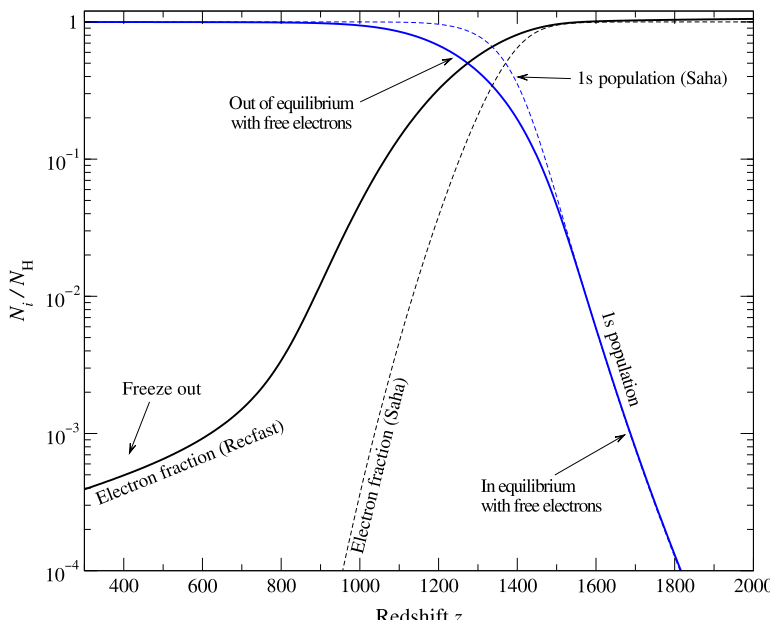
**Fig. 2.** Hydrogen recombination history compared to Saha equilibrium. N_i denotes the electron number density ($i = \mathrm{e}$) and ground-state hydrogen atoms ($i = 1\mathrm{s}$). Hydrogen recombination is strongly delayed due to the "bottleneck" created in the Lyman-α resonance and the slow 2s–1s two-photon transition (see Section 2.4 for details). *Adapted from Sunyaev and Chluba (2009).*

free electrons and protons practically froze out, leaving only a tiny residual fraction of free electrons $N_e/N_H \sim$ a few $\times 10^{-4}$ relative to the total number density of hydrogen nuclei in the Universe. This freeze-out marks the end of the cosmological recombination epoch. It occurs because at those low densities,[2] the average recombination time for a hydrogen atom became comparable to the Hubble time, and free electrons and protons hardly had any partners left to collide with. At even lower redshifts ($z \lesssim 10$), the Universe finally was reionized once the first sources of energetic photons appeared (see Section 6).

2.1.3 What Is So Special About Cosmological Recombination?

One important reason for the simplicity of cosmological recombination is the extremely large specific entropy of our Universe: there are roughly 1.6×10^9 photons per baryon. The reader might have already noticed that all the atomic species recombined when $k_B T_\gamma$ was several times smaller than the ionization potential of the recombining atomic species, where T_γ is the CMB blackbody temperature. For example, in the case of He III $\rightarrow$ He II recombination at redshift $z \sim 6000$, one has $k_B T_\gamma \sim 1.4$ eV. This is about 39 times below the ionization potential of hydrogenic helium ions, $\chi_{He II} = 54.4$ eV. The reason is the huge excess of CMB photons over baryons, so that the total number of energetic (i.e., ionizing) photons far out in the Wien tail of the CMB blackbody spectrum is sufficiently large to keep atoms from recombining.

The second implications of the large photon number is that the free electrons remain tightly coupled to the ambient radiation field, due to the tiny energy exchange associated with Compton scattering events. This causes the thermodynamic temperature of electrons to equal the CMB blackbody temperature with very high precision until $z \sim 200$ (Zeldovich et al., 1968). Without this strong interaction between photons and electrons, the temperature of the electrons would decrease as $T_e \propto (1+z)^2$, while the temperature of the photon field drops as $T_\gamma \propto (1+z)$. In addition, very fast Coulomb interactions and atom–ion collisions result in the full thermodynamic equilibrium between the photons, electrons, ions, and neutral atoms. Only below $z \sim 200$ does the matter temperature start to drop faster than the radiation temperature, a fact that is also very important in connection with the 21-cm signals coming from high redshifts (Pritchard

---

[2] At redshift $z \sim 700$, there are ~ 0.1 cm^{-3} free electrons and protons left in the gas.

and Loeb, 2008), before the Universe became reionized at $z \sim 10$ (Madau et al., 1997, see also Sections 5 and 6).

Finally, the huge excess of CMB photons over baryons implies that processes occurring in the baryonic sector are unable to strongly affect any of the radiation properties down to redshifts where the first stars and galaxies appear. This means that the atomic rates are largely dominated by radiative processes, including stimulated recombination, induced emission, and absorption of photons. In addition, the slow expansion of the Universe allows us to consider the evolution of the atomic species along a sequence of quasi–stationary stages, where the populations of the excited levels are nearly in full equilibrium with the radiation field, but only subsequently and very slowly drop out of equilibrium, finally leading to recombination and the release of additional photons in uncompensated bound-bound and free-bound transitions.[3]

2.2 Why Should We Bother?

Cosmological recombination is interesting and important because during this epoch several signals are imprinted onto the CMB that today can teach us about the early conditions of our Universe (see Fig. 3). In this respect, the CMB temperature and polarization anisotropies are probably the most well known; however, the three recombination epochs also introduce some tiny spectral distortions in the CMB blackbody, which might become observable in the future. Below we provide more details about each of these signals. For more about the formation of CMB anisotropies we recommend the book of Dodelson (2003), while for the cosmological recombination radiation Sunyaev and Chluba (2009) provide an in–depth overview and additional references.

2.2.1 *Importance of Recombination for the CMB Anisotropies*

For $z \gtrsim 10^4$, well before the recombination epoch, the Universe was completely optically thick to CMB photons. In this era, the baryons and photons behaved as a single fluid, with baryons being gravitationally attracted by the overdensities of the medium while at the same time feeling the pressure exerted by the photons. Under these conditions, acoustic oscillations in the photon–baryon fluid were created which today are visible as CMB temperature and polarization anisotropies (Peebles and

---

[3] In full thermodynamic equilibrium transitions between level $A \to B$ are fully compensated by the inverse transition $B \to A$. The term "uncompensated transition" therefore means that the net rate between two levels does not vanish.
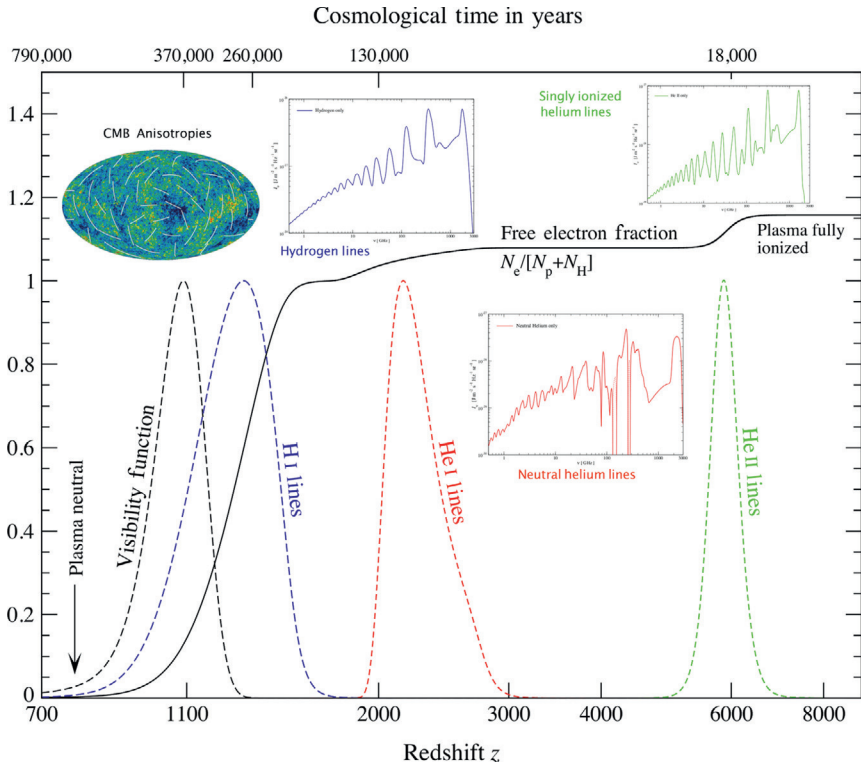
Fig. 3. Ionization history of the Universe (solid black curve) and the origin of different CMB signals (dashed lines and inlays). The observed temperature anisotropies in the CMB temperature are created close to the maximum of the Thomson visibility function around $z \sim 1089$, whereas the direct information carried by the photons in the cosmological hydrogen recombination spectrum is from slightly earlier times. The photons associated with the two helium recombination epochs were released at even higher redshifts. Finding the traces of these signals in the cosmological recombination spectrum could therefore allow us to learn about the state of the Universe at $\sim 130,000$ and $\sim 18,000$ years after the Big Bang. Furthermore, the cosmological recombination radiation may offer a way to tell if something unexpected occurred before or during the cosmological recombination epoch (e.g., energy release due to annihilating dark matter or decaying relic particles). *Adapted from Sunyaev and Chluba (2009).*

Yu, 1970; Sunyaev and Zeldovich, 1970a). After subtracting the dipole anisotropy caused by our motion with respect to the CMB rest frame ($\Delta T_0 / T_0 \sim 10^{-3}$), one is left with whole sky directional variations of only $\Delta T_0 / T_0 \sim 10^{-5}$ in the CMB temperature around a mean value of $T_0 = 2.726\,\mathrm{K}$ (Fixsen et al., 2011). These have been measured in orbit by *COBE* (Smoot et al., 1992) and *WMAP* (Bennett et al., 2003a; Page et al., 2003).

Furthermore, many ground-based and balloon-borne CMB experiments provided additional high-quality data, such as MAXIMA (Hanany et al., 2000), Boomerang (Netterfield et al., 2002), DASI (Halverson et al., 2002), ARCHEOPS (Benoît et al., 2003), CBI (Pearson et al., 2003), and VSA (Rubiño-Martin et al., 2003). All together, these data sets form one of the major pillars for the cosmological concordance model (Bennett et al., 2003a).

However, this is not the end of the story. The *Planck* satellite (The Planck Collaboration, 2006) has scanned the whole CMB sky, producing new data with unprecedented precision, while at small angular scales both ACT (e.g., see Das et al., 2011; Dunkley et al., 2011; Hajian et al., 2011) and SPT (Lueker et al., 2010; Vanderlinde et al., 2010) have refined the measurements of the temperature anisotropies. In the near future, many additional experiments are going to produce an increasing body of high-precision CMB data. These experiments include SPTPOL (McMahon et al., 2009), ACTPOL (Niemack et al., 2010), QUIET (QUIET Collaboration et al., 2011), SPIDER (Crill et al., 2008), POLARBEAR (The Polarbear Collaboration et al., 2010), and LiteBIRD (Matsumura et al., 2013). With all these data sets, it will become possible to constrain the key cosmological parameters with incredible precision in the range $\sim$0.1–1%. One of these parameters is the total density of the Universe Ω_{tot} relative to the critical density necessary to halt the expansion of the Universe where "total" encompasses dark energy, dark matter, baryons, neutrinos, etc. Another is the quantity $\Omega_{\text{b}} h^2$, where $h = H_0/(100\,\text{km}\,\text{s}^{-1}\,\text{Mpc}^{-1})$. Such precision will also allow us to ask detailed questions about the underlying inflationary model that is responsible for the initial perturbation power spectra. Constraining the epoch of inflation is one of the most important goals of the investigations with *Planck*, and the imperative is to make sure that we have under control all systematic effects which could potentially undermine the science return of the mission.

Current and future CMB anisotropy measurements also allow us to directly constrain the effective number of neutrinos, the primordial helium abundance, and even the neutrino mass (e.g., Abazajian et al., 2013; Calabrese et al., 2013) through measurements in the CMB damping tail at small scales. These constraints will reach incredible precision with upcoming CMB polarization data because the CMB damping tail is less contaminated by foregrounds; however, all these constraints strongly depend on our understanding of the cosmological recombination process, again underlining its importance for cosmology.

But where does cosmological recombination enter into all this? It was already realized long ago by Sunyaev and Zeldovich (1970a) and Peebles and Yu (1970) that the ionization history (i.e., N_e as a function of redshift) is one of the key ingredients for theoretical predictions of the CMB temperature and polarization anisotropies. The physics that goes into these CMB predictions is well understood and today can be carried out in a few seconds with the widely used Boltzmann codes CMBFAST (Seljak and Zaldarriaga, 1996) and Camb (Lewis et al., 2000). However, $N_e(z)$ is computed separately, for example, using Recfast (described in more detail below; Seager et al., 1999). The ionization history determines the precise shape and position of the Thomson visibility function, which defines the surface of last scattering, or in other words, how the baryons and photons decouple dynamically as the Universe became transparent once the free electrons disappeared and ceased to impede CMB photons on their way through the Universe. Thus, for the interpretation of high-precision CMB data, it is crucial to understand the recombination history with very high precision, especially close to the maximum of the Thomson visibility function at $z \sim 1089$. Any change in its position or width will produce significant uncertainty in the determination of major parameters of the Universe, as the new data sets will be sensitive to modifications of N_e at a 0.1% level. It is therefore necessary to understand the process of recombination with the highest possible precision.

2.2.2 Spectral Distortions from the Recombination Era

The dynamics of both neutral helium and hydrogen recombination are strongly affected by the production of energetic photons in the recombination process. Recombination of hydrogen leads to a total energy density release of $\Delta\rho_\gamma \sim 13.6\,\mathrm{eV}\,N_H$ in form of photons. For the moment, we are not interested in how this energy is distributed among the different lines of hydrogen (and consequently over frequency), but it is important that this energy can no longer be thermalized (for an overview on thermalization, see Chluba and Sunyaev, 2012, and references therein). Hence, all of the energy should still be present as CMB spectral distortion. Assuming that this energy is released close to $z \sim 1000$, with a photon energy density $\rho_\gamma \sim 0.26\,(1+z)^4\,\mathrm{eV\,cm^{-3}} \sim 2.7\,k_B T_0\,N_{\gamma,0}(1+z)^4$, and recalling $T_0 = 2.726\,\mathrm{K}$ and $N_{\gamma,0} \simeq 411\,\mathrm{cm^{-3}}$ for the CMB energy density, one therefore expects an average distortion of $\Delta\rho_\gamma/\rho_\gamma \sim 10^{-9}$–$10^{-8}$.

For helium, the energy release per atom is significantly larger, but because the amount of helium relative to hydrogen is only $\sim 8\%$, in

total we find $\Delta\rho_\gamma \sim [54.4 + 24.6]\, 0.08\,\text{eV}\, N_H \sim 6.3\,\text{eV}\, N_H$ from both helium recombination epochs. (Here 54.4 and 24.6 eV are the ionization potentials of singly ionized and neutral helium, respectively.) This is roughly half the energy released during hydrogen recombination. This sounds surprisingly large; however, the recombination of He I takes place close to $z \sim 2000$, while He II recombines at $z \sim 6000$. At these times, the energy density of the CMB is much larger so that the average contributions are only $\Delta\rho_\gamma/\rho_\gamma \sim 7 \times 10^{-10}$ and $\Delta\rho_\gamma/\rho_\gamma \sim 5 \times 10^{-10}$, respectively, which together are an order of magnitude smaller than for hydrogen.

These estimates again demonstrate how hard it is to perturb the CMB by energy release from baryons. However, the recombination photons are not evenly distributed over the CMB spectrum, but emitted in spectral lines with different strengths. This significantly increases the relative distortions from both the hydrogen and helium recombination epoch in certain frequency bands. For example, all the photons connected with the H I Lyman-α (Lyα) transition and the 2s–1s two-photon continuum appear in the Wien part of the CMB spectrum today, where the number of photons in the CMB blackbody is exponentially small. This makes these distortions very large, exceeding the CMB blackbody by orders of magnitude (Peebles, 1968; Zeldovich et al., 1968). Furthermore, transitions among highly excited levels of hydrogen can produce additional low-energy photons (Dubrovich, 1975), which after redshifting today reach us in the cm- and dm-spectral bands.

The spectral distortions produced by both hydrogen (Chluba and Sunyaev, 2006a; Kholupenko et al., 2005; Rubiño-Martín et al., 2006) and helium (Chluba and Sunyaev, 2010a; Rubiño-Martín et al., 2008) can also be obtained using detailed recombination computations coupled with the measured CMB anisotropies. As an example, in Fig. 4 we show the hydrogen results including all shells up to the $n = 100$ principle quantum number (Chluba and Sunyaev, 2006a). These calculations also include the previously neglected free-bound component of the recombination radiation. The photons corresponding to this spectral distortion were emitted mostly at redshifts $z \sim 1300$–1400 and therefore reach the observer today redshifted by $\sim 10^3$ (see inset in Fig. 3). These calculations included free-bound and bound-bound atomic transitions among 5050 atomic levels resolved by their orbital angular momentum l value. More recently, computations have been carried out with $\sim 61,000$ levels including the effects of l- and n-changing collisions (Chluba et al., 2010). In addition, new efficient
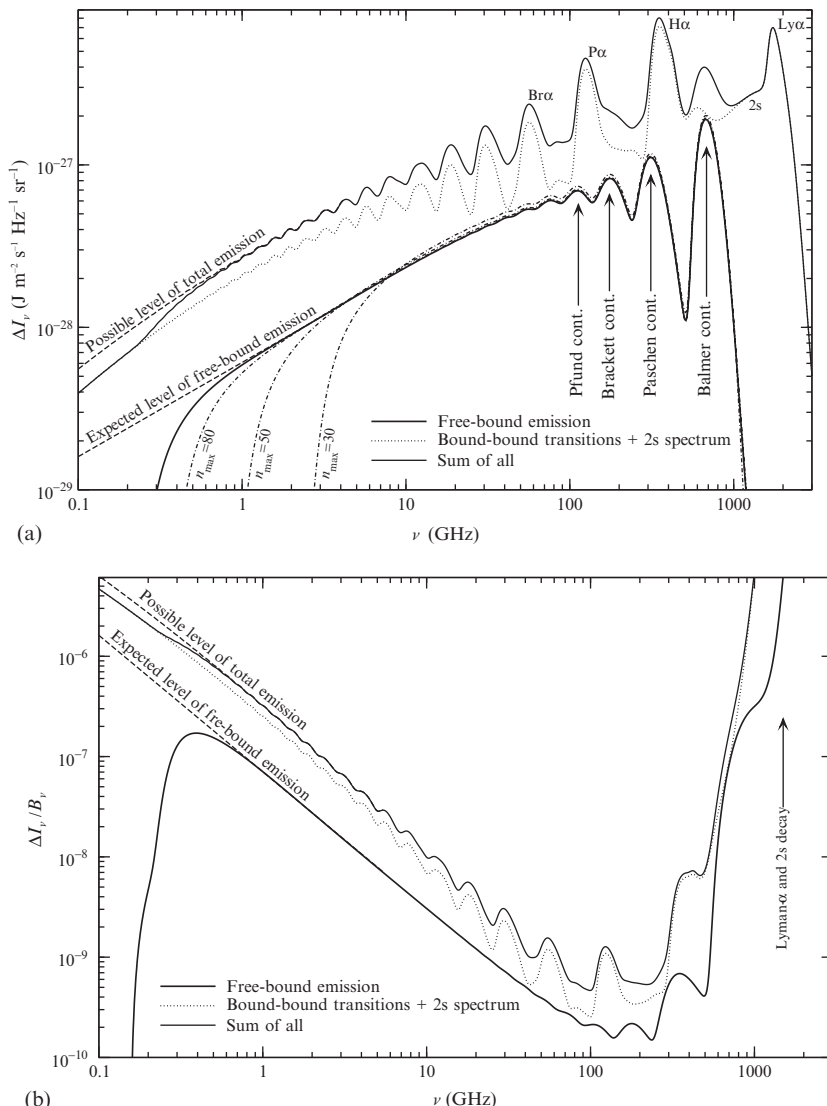
Fig. 4. (a) The hydrogen recombination emission, ΔI_ν, for an $n_{max} = 100$ shell model, including the free-bound emission. The dashed lines indicate the expected level of emission for an $n_{max} = \infty$ model. The dashed-dotted curves show the free-bound continuum spectrum for $n_{max} = 30$, 50, and 80. (b) The resulting distortion relative to the CMB blackbody spectrum B_ν. *Adapted from Chluba and Sunyaev (2006a).*

methods for computing the recombination radiation have been developed (Ali-Haïmoud, 2013), preparing us for parameter estimation with the CMB spectrum.

In Fig. 4a, at high frequencies one can clearly see the features connected with the Lyα line, the Balmer continuum and Balmer-α line (Hα), the Paschen-α line (Pα), and the Brackett-α line (Brα). At photon frequencies of $\nu \lesssim 1$ GHz, lines coming from transitions between highly excited levels start to merge into a continuum. Also distinct are the features due to the Balmer and the 2s–1s two-photon continua. Overall H$\textsc{i}$ free-bound recombination emission contributes about 20–30% to the spectral distortion at each frequency. A total of $\sim$5 photons per H atom are released in the full hydrogen recombination spectrum (Chluba and Sunyaev, 2006a). Figure 4b also shows that the relative distortion grows in both the high-frequency (Wien) and low-frequency (Rayleigh-Jeans) regions of the CMB blackbody spectrum. In the vicinity of the Lyα line, the relative distortion exceeds unity by several orders of magnitude. But unfortunately at these frequencies, the cosmic infrared background due to submillimeter, dusty galaxies renders a direct measurement very hard. Similarly, around the CMB blackbody maximum at $\sim$150 GHz it will likely be hard to measure these distortions with current technology, although there the spectral variability of the recombination radiation is largest. However, at lower frequencies ($\nu \lesssim 2$ GHz), the distortion in the intensity of the emission relative to the CMB blackbody spectrum exceeds a level of $\Delta I_\nu / B_\nu \sim 10^{-7}$ and has a well-defined frequency-dependent variability at the several percent level. This is hard to mimic by systematic effects or astrophysical foregrounds. Future observations in this frequency band may allow detection of these spectral features from the H$\textsc{i}$ recombination epoch, with possible experimental concepts such as PIXIE (Kogut et al., 2011) and PRISM (André et al., 2014) being currently discussed.

Probably, the most interesting aspect of this radiation is that it has a very peculiar but well-defined, quasi-periodic spectral dependence, and that the photons come from high z, before the formation of the CMB temperature anisotropies, the latter of which occurs close to the maximum of the Thomson visibility function. Thus, measuring these distortions in the CMB spectrum would provide the possibility of testing our understanding of the recombination epoch with direct experimental evidence. We also note that, although the simple estimates from above suggest that helium can be neglected, because of nontrivial superposition of distortions (Rubiño-Martín et al., 2008) and reprocessing of energetic

helium photons (Chluba and Sunyaev, 2010a) the effect of helium on the recombination radiation can exceed ∼30% at certain frequencies (Sunyaev and Chluba, 2009).

The recombination radiation may open another independent way to determine key parameters of the Universe, such as the average CMB temperature T_0, the number density of baryons $\propto \Omega_b h^2$ (or alternatively the specific entropy), and the primordial helium abundance (e.g., Chluba and Sunyaev, 2008a). If something unexpected happened during or before the recombination epoch, then this may leave observable traces in the cosmological recombination radiation, which could help to place tighter constraints on the thermal history of the Universe and the physics of cosmological recombination. For example, energy released by annihilating or decaying relic particles could directly ionize neutral atoms (Chen and Kamionkowski, 2004; Padmanabhan and Finkbeiner, 2005; Peebles et al., 2000), leading to additional photons in the recombination radiation (Chluba, 2010). Furthermore, primordial distortions of CMB (Sunyaev and Zeldovich, 1970b) lead to uncompensated cycles of atomic transitions (Lyubarsky and Sunyaev, 1983) before the beginning of recombination, a process that results in additional photon production and absorption (Chluba and Sunyaev, 2009b). And finally, the possible variation of fundamental constants would affect atomic transition rates and frequencies which could leave potentially observable signatures in the recombination radiation (Chluba, 2010). In particular, a combination of CMB anisotropy and spectral distortion measurement may help to shed new light on these possibilities.

2.3 Why Do We Need Advanced Atomic Physics?

It probably already is apparent that, for precise recombination calculations, detailed atomic models are required for hydrogen and helium. In general, the situation is extremely good for hydrogen and hydrogenic helium, though some issues do remain which we highlight later. In the nonrelativistic limit, the wavefunctions of unperturbed states can be calculated analytically, and consequently the transition frequencies and dipole transition rates are easily evaluated using recursion relations (Karzas and Latter, 1961; Storey and Hummer, 1991). To emphasize the sensitivity of the recombination computation to the atomic data, we mention that neglecting the effect of the reduced mass of hydrogen on the transition frequencies results in an acceleration of hydrogen recombination close to $z \sim 1100$ by $\Delta N_e / N_e \sim 0.6\%$, while the difference in the transition frequencies is merely

$|\Delta\nu/\nu| \sim 0.05\%$. More recent computations have also considered the effects of low-probability quadrupole transitions to the ground state (Grin and Hirata, 2010) and among excited states (Chluba et al., 2012), but found negligible effects on the recombination dynamics.

These kind of calculations can be carried out after completing an upper-level undergraduate course on quantum mechanics. However, solving the hydrogen recombination problem also requires handling two-photon emission and absorption, as well as Raman scattering events from excited s- and d-states (Chluba and Sunyaev, 2008b; Hirata, 2008). Again, it is in principle no problem to compute the corresponding line profiles and differential transition rates using second-order perturbation theory. But, a consistent formulation of the associated radiative transfer problem requires a special interpretation of these transition within the multilevel atom approach.

For the Rydberg states in hydrogen, it is also important to understand the effect of collisions. These can help push highly excited shells into full statistical equilibrium, with number densities for atoms in a given nl level proportional to the appropriate statistical weight, that is, $N_{nl} = (2l + 1)N_n/n^2$, where N_n is the total number density of H atoms with an electron in the nth shell.[4] This affects the flow of electrons toward lower levels and hence the recombination dynamics as well as the associated spectral distortions. Unfortunately, the estimates for collisional rates commonly used in stellar atmosphere calculations (Mashonkina, 1996) do not reach the 0.1–1% accuracy required here. Thus, even the most detailed computations of the effect of collisions during hydrogen recombination still remain uncertain by at least an order of magnitude (Chluba et al., 2010). Fortunately, the effect of collision on the CMB power spectra is found to be small, but for the recombination spectrum at low frequencies computations are still needed for precise predictions.

For neutral helium, the situation is not as good as for hydrogenic atoms. Here one faces a three-body problem (2 electrons and an α-particle). Full analytic solutions for the wavefunctions cannot be given. For the innermost shells, the coupling between the spins of the two electrons strongly affects the wavefunctions, leading to singlet and triplet state, with antiparallel and parallel spins, respectively. A perturbative approach has to be used to compute the level energies and transition rates (Drake, 2006). Going to

---

[4] One does not have to worry about the magnetic quantum number m since these are always fully mixed by collisions and radiative transitions, and because of the nearly perfect isotropy of the medium.

higher n, the singlet and triplet states are no longer well separated and start to mix, slowly becoming more hydrogenic.[5]

For recombination calculations, this means that many different approximations for the atomic data of helium had to be stitched together (Porter et al., 2009; Rubiño-Martín et al., 2008; Switzer and Hirata, 2008a), implying that the overall uncertainty is worse than for hydrogen, especially for the He I recombination spectrum. Only recently have highly accurate and user-friendly tables for the main transitions and energies of levels with $n \leq 10$ been published (Drake and Morton, 2007). These include some low-probability singlet–triplet transitions and put this part of the helium model atom on much more solid footing. However, the available atomic data for neutral helium are still rather sparse, even if in principle much more accurate rates and transition frequencies could be computed. This is especially true for levels with intermediate principle quantum number, $10 \leq n \lesssim 30$, and small orbital quantum numbers, $l \lesssim 5$. For levels with $n \gg 1$, the nonhydrogenic aspects of the wavefunctions become very small, so that only transition frequencies have to be computed precisely, while hydrogenic formulae can be used to approximate the transition rates. Nevertheless, for the recombination calculations it would be very useful to have one database that provides all the transition rates and frequencies, as well as the differential photon–ionization cross sections for helium with j-resolved levels up to $n \sim 50$–100, where j denotes the total angular momentum of the electrons wave function. Similar statements apply to the available data for collisional transitions. All this shows that for the neutral helium recombination problem, atomic physics becomes important at a much more basic level than for hydrogen.

2.4 Simple Model for Hydrogen Recombination

We begin with a very simple H atom model (see Fig. 5) with three bound states (1s, 2s, and 2p) and the continuum (free electrons and protons plus some free electrons from helium). We can then ask how the electrons reach the ground state. It was already realized at the end of the 1960s (Peebles, 1968; Zeldovich et al., 1968) that during the epoch of cosmological hydrogen recombination, any direct recombination of electrons to the ground state is immediately followed by the ionization of a neighboring

---

[5] When thinking about neutral helium, we are always assuming that one of the electrons is in the ground state. For the second electrons far from the nucleus, this means that the charge of the nucleus is shielded by the inner electron, and the wavefunction starts to become hydrogenic for sufficiently large n.
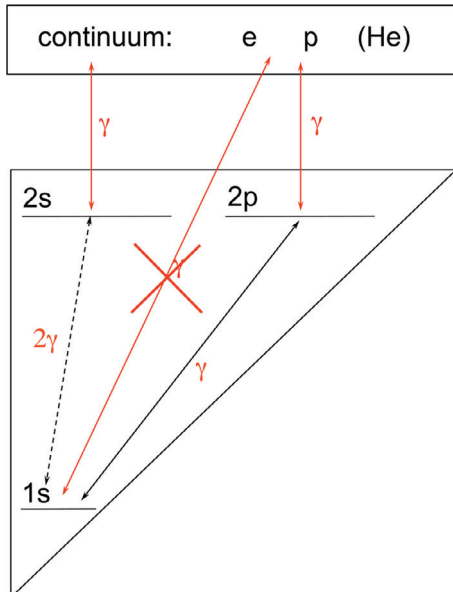
Fig. 5. Simple model for hydrogen with three bound levels and continuum. Direct recombinations to the ground state can be neglected, while the effective transition rate in the Lyα channel is suppressed by ∼8 orders of magnitude. This makes the 2s–1s two-photon channel crucial for recombination calculation. Here γ signifies a single-photon transition and 2γ a two-photon transition.

neutral atom due to reabsorption of the newly released Lyman–continuum photon. At the redshift $z = 1100$, a photon emitted just above the Lyman–continuum threshold is absorbed within a mean free path given by $(\sigma_{1sc} N_{1s})^{-1} \sim 7.3 \times 10^{14}\,\mathrm{cm} \sim 2.4 \times 10^{-4}\,\mathrm{pc} \sim 49\,\mathrm{AU}$, which at this epoch corresponds to a redshifting by $\Delta z/z \sim \Delta \nu/\nu \sim 10^{-9}$ (e.g., see Chluba and Sunyaev, 2010a). Here σ_{1sc} is the H I 1s photoionization cross section. This mean free path is very close to the distance between the Sun and the dwarf planet Pluto at its aphelion, which on cosmological scales is tiny. For the cosmological recombination problem, direct recombinations to the ground state can therefore be safely neglected. The overall uncertainty caused by this approximation is $|\Delta N_e/N_e| \lesssim 10^{-6}$ (Chluba and Sunyaev, 2007).

   Having excluded direct recombinations to the ground state, the next possibility to consider is recombination to the 2p level followed by a Lyα transition. Here a similar problem arises. The Lyα photons are trapped inside the resonance line and, despite a low H I number density, scatter $\sim 10^8$–10^9 times before redshifting sufficiently far into the red wing of

the line, thereby escaping the interaction with neutral hydrogen atoms.[6] This means that per emission only about 10^{-9}–10^{-8} transitions result in the settling of the electron into the ground state, giving an effective Lyα transition rate of $A_{21}^* \sim 1$–$10\,\mathrm{s}^{-1}$. This rate also takes into account the large number of CMB photons in the Balmer continuum, making an excitation to the second shell practically equivalent to an ionization event. Thus, this strongly reduced, effective 2p–1s transition rate significantly slows down recombination.

It is because of these very peculiar circumstances that the low probability 2s–1s two-photon channel, with a transition rate $A_{2s1s} \sim 8.22\,\mathrm{s}^{-1}$ (e.g., Labzowsky et al., 2005; Spitzer and Greenstein, 1951), is able to substantially control the dynamics of cosmological hydrogen recombination (Peebles, 1968; Zeldovich et al., 1968). Despite having a transition rate 8 orders of magnitude lower than the vacuum Lyα rate, about 57% of all hydrogen atoms in the Universe recombine through the 2s–1s channel (Chluba and Sunyaev, 2006a). The two photons that are released in the 2s–1s two-photon continuum largely do not interact with neutral hydrogen atoms, as most of the photons appear far below the optically thick Lyα resonance.

As explained below, refinements of this simple picture are necessary. However, we can already understand that the competition between the 2s–1s and 2p–1s radiative channels is very important for the cosmological recombination process. Changes in the efficiencies of these two channels directly translate into changes of the recombination history, and a detailed description is required. Furthermore, any additional channel that leads to the ground state of hydrogen with an effective transition rate at the level of $\sim 10^{-2}\,\mathrm{s}^{-1}$–$10\,\mathrm{s}^{-1}$ should be carefully considered (i.e., comparable to $\gtrsim 0.1\%$ of the Lyα channel).

2.5 Multilevel Recombination Model and RECFAST

The simple picture explained in the previous section was already developed in the late 1960s (Peebles, 1968; Zeldovich et al., 1968). With these approximations, one can write down two ordinary differential equations that can be solved numerically (one for the evolution of the free proton number density and one for the matter temperature). Amazingly, the state-of-the-art formulation of the recombination problem can be distilled down

---

[6] Photons in the blue wing of the Lyα resonance will eventually reach the line center because of redshifting. This will increase the net ionization rate. Therefore, "escape" is defined by the rate at which photons move to very far below the resonance wavelength, where they cannot return to the line center anymore.

with only a few additional equations (Ali-Haïmoud and Hirata, 2011; Chluba and Thomas, 2011). However, it is clear that physically the simple recombination model requires several refinements.

First of all, electrons can enter the hydrogen atom via higher levels (see Fig. 6). In the early calculations, this was included via the approximation that all excited levels are in equilibrium with the $n = 2$ shell and an effective recombination rate could be computed. However, this assumption is not entirely correct and the evolution of excited levels has to be considered more carefully (Chluba et al., 2007; Seager et al., 2000). Furthermore, electrons reaching any of the np-states in principle can directly transition to the ground state, opening up additional routes for recombination to happen. Here again, the emitted photons are trapped in the resonance and the effective recombination rate is strongly reduced, as for the Lyα resonance (Seager et al., 2000).

In addition, helium was neglected in the first considerations of the recombination problem. Doubly ionized helium recombines at times much
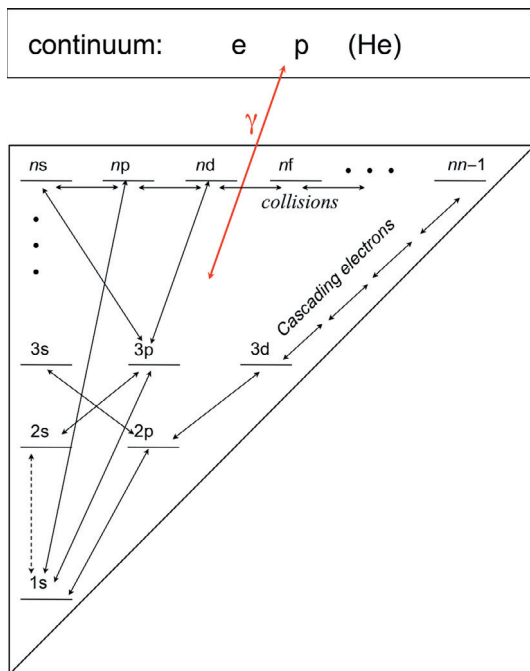

Fig. 6. Schematic of the multilevel H atom with bound levels and continuum. Resolving all levels in n and l implies a total of $\sim n^2/2$ levels. As n increases, this makes a numerical solution of the system of rate equations extremely demanding.

before the last scattering surface, and consequently does not affect the CMB anisotropies at a significant level, so that one can simply use the simple Saha equation to approximate the He II recombination history (e.g., see Switzer and Hirata, 2008b). However, it is the slight deviations from equilibrium which generates the He II recombination spectrum, and to accurately calculate this spectrum requires a multilevel treatment (Chluba et al., 2007; Rubiño-Martín et al., 2008), though here we omit these complications. For neutral helium, the physical problem is very similar to the one of hydrogen: direct recombinations to the ground state are negligible; the slow 2^1S_0–1^1S_0 two-photon channel competes with the inhibited 2^1P_1–1^1S_0 resonance; and recombinations to excited levels have to be included (Seager et al., 2000). The notation used here for this two-electron system is n^SL_J, where n is the principle quantum number of the active electron, S the total electron spin of the system, L the total orbital angular momentum, and J the total angular momentum.

The computations carried out by Seager et al. (2000) considered most of these extensions to the simple hydrogen recombination model. They considered a 300-shell atomic model for hydrogen, with the assumption of full statistical equilibrium among the angular momentum sublevels and implemented a neutral helium model consisting of 100 individual levels (with singlet and triplet states). Also, a simple chemical network for the late recombination history was included, and the temperature equation for the electrons was evolved.

All this boosted the numerical burden when calculating $N_e(z)$ by a large factor. For predictions of the CMB power spectra, it became necessary to find a faster method to compute the recombination problem. This lead to the development of Recfast (Seager et al., 1999), which provided an efficient way of representing the numerical results obtained with the more elaborate multilevel code by just three ordinary differential equations (one for the free proton number density, one for He II number density, and one for the matter temperature) and introducing an appropriate fudge factor for the effective recombination coefficient of hydrogen.

Recfast was a great improvement over earlier, more simplistic analytic approximations (Jones, 1985; Peebles, 1968; Zeldovich et al., 1968). It allowed very fast and efficient computation of the ionization history with a precision that is still sufficient even for the precision data from *WMAP* (Rubiño-Martín et al., 2010; Shaw and Chluba, 2011). However, for CMB data from *Planck*, several more subtle refinements are required, as we discuss below.

2.6 Detailed Recombination Physics During H I Recombination

Here we give a brief overview of the additional physical processes that have been considered for the hydrogen recombination problem. We focus on modifications arising because of two–photon transitions, Raman scattering events, and collision, as these three are likely to be of greatest interest to the AMO physics community. Other processes which have been considered include the effect of deviations from full statistical equilibrium in the angular momentum substates (Chluba et al., 2007, 2010; Grin and Hirata, 2010); stimulated 2s–1s two-photon decay (Chluba and Sunyaev, 2006b); reabsorption of Lyα photons in the 1s–2s two-photon transition (Ali-Haïmoud and Hirata, 2011; Fendt et al., 2009; Hirata, 2008; Kholupenko and Ivanchik, 2006); feedback in the H I Lyman series (Ali-Haïmoud and Hirata, 2011; Ali-Haïmoud et al., 2010; Chluba and Sunyaev, 2007, 2010a; Kholupenko et al., 2010); and partial frequency redistribution by the Lyα resonance (Ali-Haïmoud and Hirata, 2011; Chluba and Sunyaev, 2009a; Chluba and Thomas, 2011; Grachev and Dubrovich, 2008; Hirata and Forbes, 2009), as well as by electron scattering (Ali-Haïmoud et al., 2010; Chluba and Sunyaev, 2009a; Chluba et al., 2012). For more in-depth overview, we refer the interested reader to Fendt et al. (2009), Rubiño-Martín et al. (2010), and Sunyaev and Chluba (2009).

The superposition of all effects discussed in the literature thus far leads to an ambiguity in the ionization history during the cosmological hydrogen recombination epoch that clearly exceeds the 0.1% level, even reaching $|\Delta N_e/N_e| \sim 3\%$ close to the maximum of the Thomson visibility function at $z \sim 1100$ where it matters the most (see Fig. 7). All the above mentioned corrections should therefore be taken into account in the detailed analysis of future CMB data (Rubiño-Martín et al., 2010; Shaw and Chluba, 2011).

2.6.1 Two-Photon Transitions from Higher Levels

One of the most interesting corrections to the recombination problem is due to coherent two-photon transitions[7] of excited hydrogen levels to the ground state, as initially proposed by Dubrovich and Grachev (2005). The estimated effect very close to the maximum of the Thomson visibility function was anticipated to be as large as ∼5% and therefore would have had a large impact on the theoretical predictions for the CMB power spectra (Lewis et al., 2006). However, it turns out that the estimates of

---

[7] That is, two photons emitted simultaneously in one quantum act.
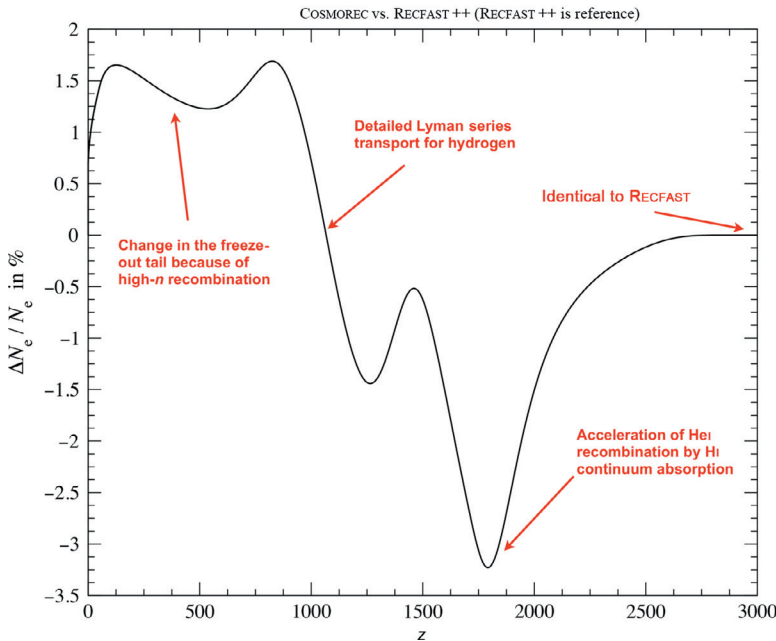
Fig. 7. Modifications to the cosmological ionization history during hydrogen ($z \sim 1100$) and neutral helium ($z \sim 2000$) recombination. We show here the relative difference between COSMOREC (Chluba and Thomas, 2011) and the recombination model implemented by Seager et al. (1999) computed using RECFAST++.

Dubrovich and Grachev (2005) only captured part of the modification related to the two–photon problem, overestimating the effect by about one order of magnitude.

In extremely low–density plasmas, the cascade of permitted transitions (e.g., the chain 3s→2p→1s) is unperturbed by collisions and should be considered as a coherent two–photon process with two resonances (Göppert-Mayer, 1931). The two–photon decay profiles can be computed using second–order perturbation theory. In Fig. 8, we show those for the 3s–1s and 3d–1s transitions. Comparing the profile shapes with a normal Lorentzian, it is clear that the differential absorption and emission probabilities are modified. These changes are purely quantum mechanical in nature and most strong in the distant damping wings. This means that the net transition rates of electrons from the upper levels should also be affected, once these corrections are included in the radiative transfer calculation. The problem for the 3d–1s and 3s–1s two–photon transitions was considered in detail by Chluba and Sunyaev (2010b). This analysis demonstrated that
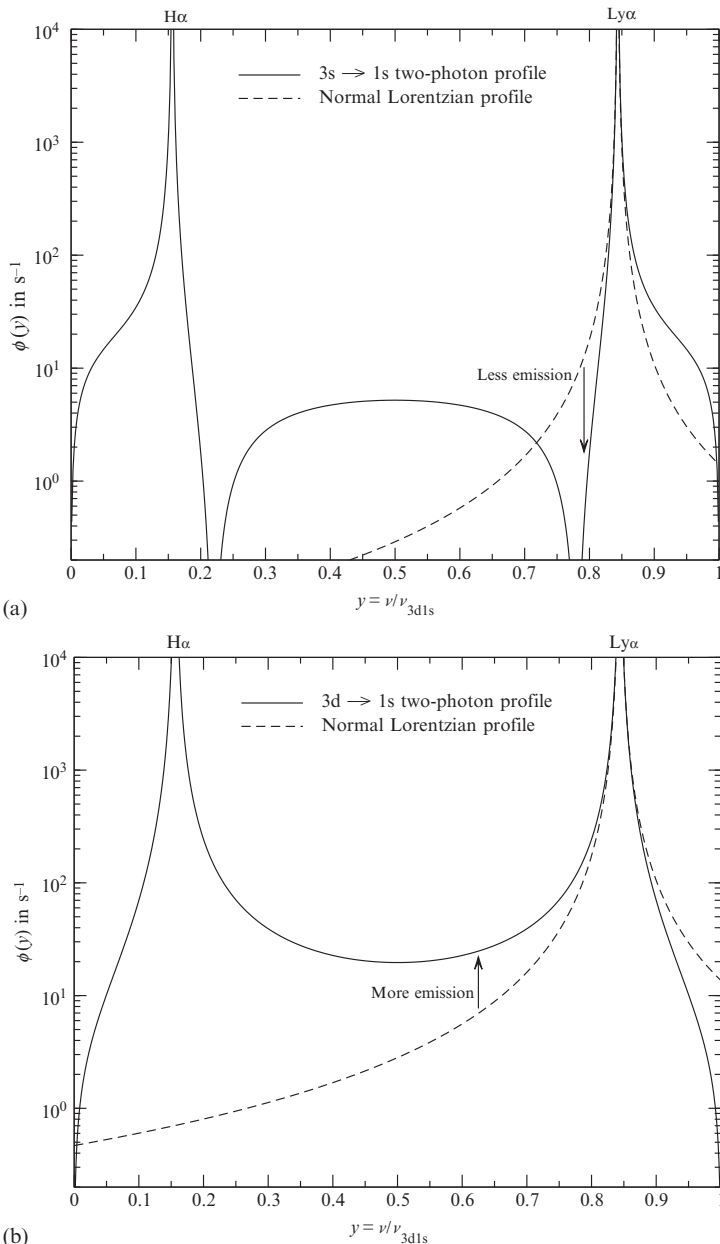
Fig. 8. Two-photon emission profile for the 3s $\rightarrow$ 1s and 3d $\rightarrow$ 1s transitions. The horizontal axis is in normalized frequency units (in the limit where the frequency for each transition is the same) while the vertical axis gives the line shape ϕ. For comparison, we also show the usual Lorentzian corresponding to the Lyα line (long dashed). Far away from the Lyα resonance, the two-photon profiles clearly differ from the Lorentzian shape.

the total modification caused by purely quantum mechanical aspects of the problem lead to a change in the free electron number of $\Delta N_e/N_e \sim -0.4\%$ at $z \sim 1100$.

However, there are two larger effects which were not captured by the estimates of Dubrovich and Grachev (2005). One is related to a frequency-dependent asymmetry between the two-photon emission and absorption profile, while the other arises because of time-dependent aspects of the recombination problem. These two corrections are explained in detail by Chluba and Sunyaev (2009c, 2010b), but the computations of Hirata (2008) also included them. The cumulative effect of 3s–1s and 3d–1s two-photon transitions during hydrogen recombination, accounting for all three aspects mentioned above, results in accelerated recombination, that is, a decrease by $\Delta N_e/N_e$ of $\sim -1.6\%$ at $z \sim 1190$ (Chluba and Sunyaev, 2010b). Furthermore, it was shown that a detailed treatment of two-photon decays from levels with $n \gtrsim 5$ is unnecessary at $\sim 0.1\%$ precision (Ali-Haïmoud and Hirata, 2011; Chluba and Thomas, 2011).

2.6.2 The Effect of Raman Scattering

Raman scattering events must also be considered as coherent quantum processes. This is because collisional processes causing decoherence are completely negligible during the epoch of hydrogen recombination. The associated Raman interaction profiles can be computed using second-order perturbation theory. Hirata (2008) demonstrated that this results in an important delay of hydrogen recombination by $\Delta N_e/N_e \sim 0.9\%$ close to $z \sim 900$, which is dominated by 2s–1s Raman scattering events (i.e., $2s \rightarrow 3p \rightarrow 1s$ and the inverse process). The main cause of this correction is an enhancement of the photon phase space density on the blue side of the Lyα resonance, which results in an increased Lyman-β (Lyβ) feedback corrections. This effect was also found by Chluba and Thomas (2011) and Ali-Haïmoud and Hirata (2011), where it was in addition argued that Raman events from higher levels can be neglected.

2.6.3 Additional Small Corrections and Collision

Several additional corrections during hydrogen recombination have been considered. It would be too much to mention all of them in detail, but it was demonstrated that the effect of metals (Ali-Haïmoud et al., 2011) and molecular hydrogen (Alizadeh and Hirata, 2011) can be neglected. Furthermore, the feedback of photons released during helium recombination on hydrogen can be omitted in computations of the recombination dynamics

(Chluba and Sunyaev, 2010a). Possible primordial distortions of the CMB spectrum at the level allowed by *COBE*/FIRAS are also unimportant (Chluba and Sunyaev, 2009b).

Among all the small corrections, those arising from collisions with protons could still affect the recombination dynamics in the freeze-out tail of the recombination epoch ($z \lesssim 800$). Current estimates based on collision rates using in stellar atmosphere computations (see, e.g., Mashonkina, 1996) indicate that the effect of collisions is small (Chluba et al., 2010). However, in some cases these rates are uncertain by an order of magnitude. It will therefore be very important to use refined estimates of the collision rates that also include the effect of jumps with $\Delta l > \pm 1$. Furthermore, collisions do have an effect on the recombination radiation at low frequencies (Chluba et al., 2010), which deserves more detailed consideration. Recently, Vrinceanu et al. (2012) provided updated rate coefficients which will allow addressing these problems.

2.7 Detailed Recombination Physics During He I Recombination

For helium recombination, many of the effects important during the re-combination of hydrogen are also present. However, helium recombination occurs much earlier than hydrogen recombination and does not affect the Thomson visibility function as strongly, simply because there is so little helium. This means that for precise computations of the CMB anisotropies, the helium recombination model need not be as elaborate as for hydrogen recombination.

The most important corrections during the neutral helium recombi-nation are caused by the spin-forbidden He I 2 ^{3}P$_1$ − 1 ^{1}S$_0$ transition (Dubrovich and Grachev, 2005; Rubiño-Martín et al., 2008; Switzer and Hirata, 2008a; Wong and Scott, 2007) and the absorption of He I photons by neutral hydrogen (Kholupenko et al., 2007; Rubiño-Martín et al., 2008; Switzer and Hirata, 2008a). A smaller, but still noteworthy, correction is related to the feedback of helium photons (Chluba and Sunyaev, 2010a; Switzer and Hirata, 2008a), while several interesting, but in terms of the CMB power spectra negligible, corrections are reported in Switzer and Hirata (2008a,b), Hirata and Switzer (2008), and more recently in Chluba et al. (2012). For additional details, we again refer to Fendt et al. (2009), Rubiño-Martín et al. (2010), and Sunyaev and Chluba (2009). Overall neutral helium recombination is accelerated by the processes mentioned above, with helium recombination ending at $z \sim 1700$ (see Fig. 7).

2.8 HYREC and COSMOREC
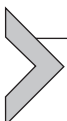
We have provided an overview of all the different recombination corrections considered in the literature thus far. These effects have been worked out as a combined effort of several independent groups, all with their own detailed recombination treatment. For analysis of CMB data, it is important to compute the CMB power spectra many times ($\sim 10^3$–10^4). However, previous methods used in detailed recombination calculations took from several hours to days of computer time per cosmology (Chluba et al., 2010; Grin and Hirata, 2010). Alternative approaches need to be found.

The RECFAST approach reformulates the main physical aspects of the cosmological recombination problem with only a few additional equations. One of the key ingredients is that the evolution of the populations in the highly excited levels need not be explicitly followed when one is interested only in the recombination dynamics. The effect of electrons in the excited states can be integrated out of the problem and extra attention need be given only to the effective recombination rates to a few levels with $n \lesssim 3$–5. These rates can be precomputed once and only depend on the electron and photon temperature.

This simplification was developed by Ali–Haïmoud and Hirata (2010) and has been the basis for the new cosmological recombination codes COSMOREC (Chluba and Thomas, 2011) and HYREC (Ali–Haïmoud and Hirata, 2011). These codes supersede the physical model of RECFAST and allow both very fast but also precise computation of the ionization history on a model-by-model basis including all the aforementioned physical processes that are important at the $\sim 0.1\%$ level. Figure 7 presents the total correction to the cosmic ionization history computed including all the important effects mentioned above. COSMOREC and HYREC are publicly available. The calculated recombination histories from each agree with one another at a level below the sensitivity of present CMB data from *Planck*, SPT, and ACT. Although for the standard cosmology the refudged version of RECFAST agrees to high precision with HYREC and COSMOREC, these recombination codes can be optionally used in CAMB for explicit parameter estimation.

To conclude our discussion of the cosmological recombination problem, we mention that in addition to all the standard physical processes described above one can also imagine that nonstandard physics beyond the standard model may become important. For example, fundamental constants, like the fine structure constant or the electron-to-proton mass ratio, could vary with time, potentially affecting the recombination dynamics. Furthermore,

energy release during recombination, for example, by decaying or annihilating particles, can delay recombination. All this could lead to changes in the CMB power spectra and hence can be constrained with future CMB data.

3. PREGALACTIC GAS CHEMISTRY

3.1 Fundamentals

At the end of the recombination epoch, at $z \sim 800$, the chemical makeup of the gas in the Universe was very simple. At this time, there were not yet any stars or galaxies, and so it is convenient to refer to the gas as "pre-galactic" gas. As we have seen above, the main constituent of this pregalactic gas was atomic hydrogen, accounting for roughly 75% of the total mass. Almost all of the hydrogen was neutral, but a small fraction remained ionized. Neutral atomic helium accounted for most of the remaining mass. Most of this helium was ^{4}He, but there was also a small fraction of ^{3}He. The abundance of singly or doubly ionized helium was very close to zero. Deuterium was also present, with a fractional abundance relative to hydrogen of D/H $\simeq$ 2.5×10^{-5} (Cyburt et al., 2008), and a D^+-to-D ratio that was essentially the same as that of ionized to neutral hydrogen. Finally, there was a trace amount of lithium (Li/H $\simeq 5 \times 10^{-10}$; Cyburt et al., 2008), the majority of which was in the form of Li^+. The fractional abundances of all other ionized or molecular species were smaller than 10^{-12} at this point (Alizadeh and Hirata, 2011).

Starting from this simple beginning, many other chemical species were produced as the Universe evolved. However, before discussing the formation and destruction of a few of the most influential of these species, it is useful to start by considering a few general principles that can help us to understand the chemical evolution of pregalactic gas.

We begin by drawing a distinction between three different classes of chemical species that are present in the pregalactic gas. "Primary" species are those present at the end of recombination, as discussed above. "Secondary" species are those that are formed directly from chemical reactions among the primary species. Finally, "tertiary" species are those formed primarily or exclusively from reactions involving one or more of the secondary species. The evolution with time of the fractional abundance of a secondary species X is largely governed by the relative sizes of four important timescales. The first of these is the formation time, that is, the timescale on which

the abundance of species X changes significantly owing to its formation in chemical reactions. This is given by

$$t_{\text{form,X}} = \frac{n_X}{R_{\text{form,X}}}, \tag{9}$$

where n_X is the number density of species X and $R_{\text{form,X}}$ is the formation rate per unit volume of X. The second important timescale is the photodestruction time, that is, the timescale on which the abundance of species X changes significantly owing to photodissociation or photodetachment. This is given by

$$t_{\text{pd,X}} = \frac{1}{R_{\text{pd,X}}}, \tag{10}$$

where $R_{\text{pd,X}}$ is the photodestruction rate of species X. Next is the collisional destruction time, which describes the timescale on which the abundance of species X changes significantly owing to destructive collisions, and which is given by

$$t_{\text{cd,X}} = \frac{n_X}{R_{\text{dest,X}}}, \tag{11}$$

where $R_{\text{dest,X}}$ is the rate per unit volume at which species X is destroyed by collisional processes (typically reactions with atomic hydrogen). Finally, there is the Hubble time, which is the timescale on which the cosmological scale factor (and hence also the gas density) changes significantly owing to the expansion of the Universe. It is given by the expression

$$t_H = \frac{1}{H(z)}, \tag{12}$$

where $H(z)$ is the Hubble parameter.

At high redshift, photodissociation of most molecules and molecular ions by the CMB occurs rapidly, and the photodissociation time is small. Similarly, the high gas density means that the formation timescale of most species is also small. In this regime, both timescales are typically much shorter than the Hubble time, and hence the abundance of species X evolves until it reaches an equilibrium value set by the balance between formation and photodissociation (in which case $t_{\text{form,X}} = t_{\text{pd,X}}$). Since photodissociation is very effective at high redshift, this equilibrium value is generally very small.
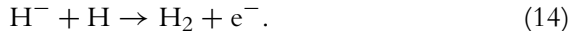
Moving to lower z, the cosmological background gas mass density decreases, since $\rho_g(z) \propto (1 + z)^3$. Hence, the formation time of any given secondary species tends to increase. However, the photon energy density

of the CMB decreases even more rapidly, $\rho_{CMB} \propto (1 + z)^4$, while the CMB temperature decreases as $T_{CMB} \propto (1 + z)$. This means that we eventually reach a redshift at which the number density of photons capable of photodissociating species X starts to fall off exponentially, as the threshold energy for photodissociation starts to fall within the exponential portion of the CMB blackbody spectrum. At this point, $t_{pd,X}$ rapidly increases, and the formation time $t_{form,X}$ becomes the shortest of the three timescales. The abundance of species X then grows rapidly until one of two things happens: either the formation time increases until $t_{form,X} \simeq t_H$, or the abundance reaches an equilibrium value at which formation is balanced by destruction via other collisional reactions, that is, $t_{form,X} = t_{cd,X}$. In the former case, the abundance of X does not significantly further increase, as the time required would be longer than the age of the Universe. In this case, we speak of the abundance of the species "freezing out" at some asymptotic value, which in general is not a true equilibrium value. In the latter case, the abundance of species X does indeed reach the value implied by chemical equilibrium, and its later evolution depends in part on how this equilibrium value evolves with redshift.

As an example, consider the case of the H^- anion discussed in more detail below. At high redshift, photodetachment of the electron by the CMB is very effective, and the H^- abundance is very small (e.g., Galli and Palla 1998, find it to be of the order of 10^{-20} at $z = 500$). At a redshift $z \sim 100$–200, however, the photodetachment time becomes considerably longer than the formation time, and the H^- abundance increases rapidly, until it reaches an equilibrium value set by the balance between formation of H^- by radiative association

$$H + e^- \rightarrow H^- + \gamma, \tag{13}$$

(where γ indicates the photon emitted during this process), and its destruction by associative detachment with atomic hydrogen

$$H^- + H \rightarrow H_2 + e^-. \tag{14}$$

At this point, the equilibrium fractional abundance of H^- relative to the total number density of hydrogen nuclei n_{Hn} is $x_{H^-} \equiv n_{H^-}/n_{Hn} \sim 10^{-11}$. However, this equilibrium fractional abundance declines at lower redshift owing to the rate coefficient for reaction (13) decreasing with decreasing temperature. In comparison, the freeze-out abundance of H^- at this time (i.e., the value for which $t_{form,H^-} = t_H$) is $\sim 10^{-6}$. H^- therefore reaches chemical equilibrium well before freeze-out can become important.

Most of the other secondary species behave similarly to H^-, in that their low redshift abundances reach equilibrium values for which $t_{\mathrm{form,X}} = t_{\mathrm{cd,X}}$, with the destruction of these species typically being dominated by reactions with atomic hydrogen, the most abundant constituent of the pregalactic gas. One exception is neutral lithium. This is formed by radiative recombination of Li^+. The Li-to-Li^+ ratio increases steadily as one moves to lower redshift, due to the steady decrease in the lithium photoionization rate caused by the redshifting of the CMB. However, complete conversion of Li^+ to Li never occurs, even once the photoionization rate has decreased to a negligible value, as the Li^+ recombination timescale quickly becomes greater than the Hubble time (Switzer and Hirata, 2005).

Turning our attention to the tertiary species, we note that the four timescales discussed above are still important, but that an added complication is posed by the fact that the evolution with redshift of the tertiary species is determined in part by the evolution with redshift of the secondary species from which they form. For example, consider molecular hydrogen, H_2, illustrated in Fig. 9. As we discuss in more detail below, this is formed in the pregalactic gas via reaction pathways involving H^- and H_2^+ (with some fraction of the latter forming from reactions involving HeH^+). Because the photodestruction thresholds of H^- and H_2^+ are significantly different, they become abundant in the gas at different redshifts, and the H_2 fraction in the pregalactic gas therefore goes through two main periods of growth, one coinciding with a rapid increase in the H_2^+ abundance and a later one coinciding with a similar rapid increase in the H^- abundance.

3.2 Key Reactions

Comprehensive discussions of the wide variety of chemical reactions that occur in pregalactic gas have been given by a number of authors (see, e.g., Abel et al., 1997; Galli and Palla, 1998, 2013; Glover and Savin, 2009; Lepp et al., 2002; Stancil et al., 1996, 1998). In this review, we do not attempt to follow suit, but instead will focus on a much smaller subset of reactions that are important for understanding the later evolution of the gas.

3.2.1 Molecular Hydrogen (H₂)

We begin our survey with the chemistry involved in the formation and destruction of H_2. Direct formation of the H_2 molecule by radiative association of two hydrogen atoms is strongly forbidden, and hence the formation of H_2 in pregalactic gas takes place via several indirect routes.
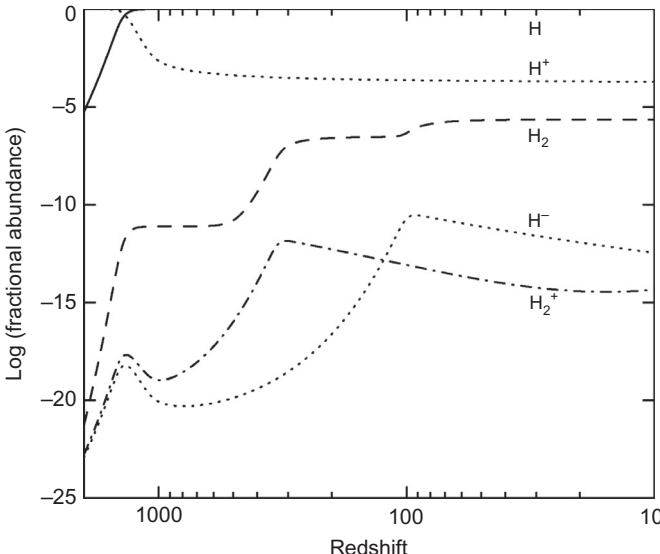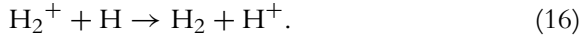
Fig. 9. Evolution with redshift of the fractional abundances of several important species in pregalactic gas. H and H^+ are examples of primary species with simple chemical histories. The log(fractional abundance) of H is indistinguishable from 0 for $z \lesssim 1000$. The H^+ abundance initially declines rapidly during the epoch of cosmological recombination, but eventually freezes out at a value of $\sim 10^{-4}$. H^- and H_2^+ are examples of secondary species with more complex histories. At high redshift, they are destroyed very rapidly by the CMB and have very small abundances. At lower redshift, however, photodestruction becomes unimportant, owing to the redshifting of the CMB, and the H^- and H_2^+ abundances increase rapidly, until they reach a new equilibrium set by collisional destruction processes. The redshift at which this transition occurs depends on the H^- detachment energy E_{det} and the H_2^+ dissociation energy E_{diss}. This occurs at a higher redshift for H_2^+ ($E_{diss} = 2.65$ eV) than for H^- ($E_{det} = 0.755$ eV). Finally, H_2 is an example of a tertiary species that is formed by reactions involving H^- or H_2^+. The H_2 abundance goes through several pronounced periods of growth, coinciding with peaks in the H^- and H_2^+ abundances.

The most important of these involves the H^- ion as an intermediate state. As we have already seen, H^- forms via the radiative association process described in Eq. (13). The H^- ion then undergoes an associative detachment reaction with another hydrogen atom (reaction 14), yielding H_2. An important point to note here is that although free electrons must be present in the pregalactic gas in order for this pair of reactions to operate, they are not consumed in the process—there is no net reduction in the number density of free electrons, implying that as long as the gas remains partially ionized, this process will continue to operate.

The second major pathway to H_2 involves the H_2^+ ion as an intermediate state. This again is formed by a radiative association, this time involving H and H^+

$$H + H^+ \rightarrow H_2^+ + \gamma, \qquad (15)$$
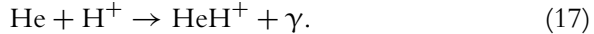
and is then converted into H_2 by a charge transfer reaction

$$H_2^+ + H \rightarrow H_2 + H^+. \qquad (16)$$

Here the proton plays a role similar to that of the electron in the H^- pathway: it is needed to initiate the chemistry, but is not permanently removed from the gas.

Lastly, some H_2 also forms via a third chain of reactions involving both HeH^+ and H_2^+ as intermediate ions. First, the HeH^+ ion is formed via the radiative association of He and H^+

$$He + H^+ \rightarrow HeH^+ + \gamma. \qquad (17)$$

A similar reaction involving He^+ and H is also possible, but can be ignored owing to the negligible amount He^+ present in the gas at these epochs. Next, the HeH^+ ion reacts with atomic hydrogen, yielding H_2^+

$$HeH^+ + H \rightarrow H_2^+ + He. \qquad (18)$$
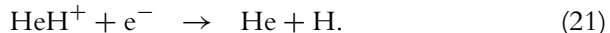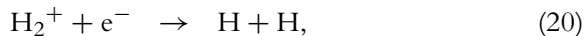
Finally, the H_2^+ reacts with H as in reaction (16) above, yielding H_2.

A common feature of all three pathways to H_2 is that the rate limiting step is the formation of the initial ion by radiative association. The H^-, H_2^+, and HeH^+ ions are all highly reactive and hence have comparatively short lifetimes (and correspondingly low equilibrium abundances) even in the low-density pregalactic gas. Aside from the reactions listed above, the main collisional processes responsible for destroying the ions are mutual neutralization with H^+

$$H^- + H^+ \rightarrow H + H, \qquad (19)$$
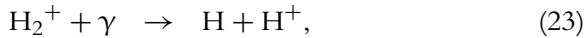
and dissociative recombination with electrons

$$H_2^+ + e^- \quad \rightarrow \quad H + H, \qquad (20)$$
$$HeH^+ + e^- \quad \rightarrow \quad He + H. \qquad (21)$$

However, the fractional ionization of the pregalactic gas is typically small enough that these reactions are responsible for destroying only a small fraction of the H^-, H_2^+, and HeH^+ ions. Far more important are several processes involving the CMB: photodetachment of H^-

$$H^- + \gamma \rightarrow H + e^-, \qquad (22)$$

and photodissociation of H_2^+ and HeH^+

$$H_2^+ + \gamma \rightarrow H + H^+, \tag{23}$$

$$HeH^+ + \gamma \rightarrow He + H^+. \tag{24}$$

As we have already discussed in Section 3.1, processes such as these dominate in the immediate aftermath of recombination, but become less effective at lower redshifts, owing to the decrease in the effective temperature of the CMB radiation field. If we assume that the CMB has a perfect blackbody spectrum, then it is straightforward to derive photodestruction rates for H^-, H_2^+, or HeH^+, provided that the populations of their internal energy levels have their local thermodynamic equilibrium (LTE) values.[8] We can then construct an estimate of the critical redshift $z_{crit,X}$ below which photodestruction becomes unimportant for a particular ion X by finding the redshift at which the photodestruction rate for that ion is equal to the rate at which the ion is destroyed by collisional processes.

For example, Galli and Palla (1998) write the photodissociation rate for the H_2^+ ion with LTE level populations as

$$R_{pd,H_2^+} = 1.63 \times 10^7 \exp\left(\frac{-32,400}{T_r}\right) s^{-1}, \tag{25}$$

where T_r is the blackbody radiation temperature. Comparing this to the rate coefficient measured by Karpas et al. (1979) for reaction (16) of

$$R_{16} = 6.4 \times 10^{-10} n_H s^{-1}, \tag{26}$$

where n_H is the number density of atomic hydrogen, one finds that $R_{pd,H_2^+} \sim R_{16}$ at a redshift $z_{crit,H_2^+} \sim 300$. A similar analysis applied to HeH^+ that uses the recent calculation of the rate coefficient for reaction (18) by Bovino et al. (2011b) yields $z_{crit,HeH^+} \sim 290$, while for H^- we obtain the significantly lower value $z_{crit,H^-} \sim 100$, owing to the fact that the photodetachment threshold energy for H^- is significantly smaller than the photodissociation threshold of HeH^+ or H_2^+.

3.2.2 Deuterated Molecular Hydrogen (HD)
Another important primordial molecule is the singly deuterated form of molecular hydrogen, HD. As we discuss in more detail in Section 4, this molecule is a far more effective coolant than H_2, owing to the combination of several different factors: the smaller energy separation between its

[8] Non-LTE effects are considered in Section 3.3.3 below.
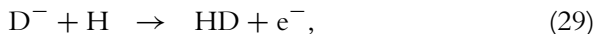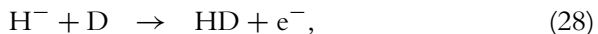
rotational levels, the fact that it is not homonuclear and hence is not divided into separate *ortho* and *para* states that do not radiatively mix, and the fact that it has a nonzero dipole moment.

In pregalactic gas, HD can form via a number of different pathways. In contrast to H_2, formation of HD by direct radiative association is not strongly forbidden, and hence a small amount of HD can form via the reaction

$$H + D \rightarrow HD + \gamma. \qquad (27)$$
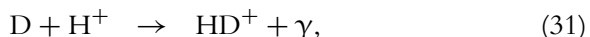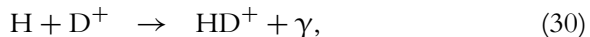
However, the rate of this reaction is very small (Dickinson, 2005), and if this were the only possible formation mechanism for HD, then the final fractional abundance of HD would not exceed a few times 10^{-10}.

Indirect formation of HD via the H^- and D^- ions is also possible,

$$H^- + D \quad \rightarrow \quad HD + e^-, \qquad (28)$$

$$D^- + H \quad \rightarrow \quad HD + e^-, \qquad (29)$$
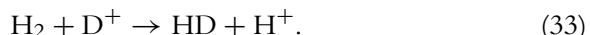
as are analogues of reactions (15) and (16) involving HD^+

$$H + D^+ \quad \rightarrow \quad HD^+ + \gamma, \qquad (30)$$

$$D + H^+ \quad \rightarrow \quad HD^+ + \gamma, \qquad (31)$$

$$HD^+ + H \quad \rightarrow \quad HD + H^+. \qquad (32)$$
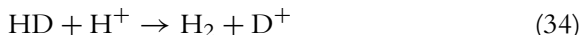
The fractional abundance of HD that is produced by these reactions typically does not exceed $x_{HD} \sim x_{H_2} \times [D/H]$, where $[D/H]$ is the cosmological ratio of deuterium to hydrogen. Since $x_{H_2} \sim 10^{-6}$ and $[D/H] \simeq 2.5 \times 10^{-5}$ (Cyburt et al., 2008), this implies that the maximum HD abundance that can be produced by these reactions is a few times 10^{-11}, that is, smaller than the amount produced by direct radiative association.

HD can also form via an ion–neutral reaction between D^+ and H_2, namely

$$H_2 + D^+ \rightarrow HD + H^+. \qquad (33)$$

This reaction proceeds rapidly and dominates the production of HD once the H_2 abundance exceeds $x_{H_2} \sim 10^{-6}$. The inverse reaction

$$HD + H^+ \rightarrow H_2 + D^+ \qquad (34)$$

also occurs. However, the binding energy of HD is larger than that of H_2, and so reaction (33) is exothermic while reaction (34) is endothermic. Reaction (34) therefore becomes very slow at low temperatures, leading to an enhancement of the HD to H_2 ratio over the cosmological deuterium to

hydrogen ratio, an effect known as chemical fractionation. In equilibrium, the HD to H_2 ratio is given by

$$\frac{x_{HD}}{x_{H_2}} = \frac{k_{33}}{k_{34}} \frac{x_{D^+}}{x_{H^+}}, \tag{35}$$

where k_{33} is the rate coefficient for reaction (33) and k_{34} is the rate coefficient for reaction (34). Using the values for these rate coefficients given by Galli and Palla (2002), we obtain

$$\frac{x_{HD}}{x_{H_2}} \simeq 1.5 \exp\left(\frac{488}{T}\right) \frac{x_{D^+}}{x_{H^+}}, \tag{36}$$

where the ratio of the fractional abundances of D^+ and H^+, x_{D^+}/x_{H^+}, is typically very close to the cosmological deuterium-to-hydrogen ratio. The temperature of the pregalactic gas evolves roughly as

$$T = \begin{cases} 2.73(1+z) & 1+z > 200 \\ 546[(1+z)/200]^2 & 1+z < 200 \end{cases} \tag{37}$$

(see, e.g., Puy et al., 1993) and so this expression predicts that the equilibrium HD to H_2 ratio should be 100 times larger than the cosmological deuterium-to-hydrogen ratio at $z \sim 90$, and even larger at lower redshift. In practice, however, the time required to reach equilibrium becomes longer than the Hubble time at a redshift of $z \sim 110$, and so the HD to H_2 ratio freezes out at a value that is around 30–40 times the cosmological deuterium-to-hydrogen ratio.

3.2.3 Lithium Hydride
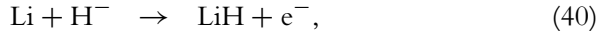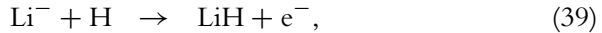
Another interesting neutral molecule that can form in the pregalactic gas is lithium hydride (LiH). This molecule has a very large dipole moment ($\mu = 5.888$ debye; Zemke and Stwalley, 1980) and hence interacts strongly with the CMB. For this reason, the possibility of detecting LiH absorption features in the CMB has attracted considerable interest (see, e.g., Bougleux and Galli, 1997 and references therein).

Lithium hydride can form by radiative association of ground-state lithium and atomic hydrogen

$$Li + H \rightarrow LiH + \gamma, \tag{38}$$

but only at a relatively slow rate. Lithium atoms in the 2p excited state can form LiH via radiative association with atomic hydrogen at a rate which is several orders of magnitude faster (Gianturco and Gori Giorgi, 1996), but the low population of the excited state typically renders this process

unimportant. Finally, LiH can also form from associative detachment of Li$^-$ with H or H$^-$ with Li

$$Li^- + H \quad \rightarrow \quad LiH + e^-, \tag{39}$$

$$Li + H^- \quad \rightarrow \quad LiH + e^-, \tag{40}$$

although both of these reactions are strongly suppressed at $z > 100$ because the H$^-$ and Li$^-$ ions are effectively photodetached by the CMB.

Pregalactic lithium hydride is destroyed by two main mechanisms. At high redshift, photodissociation by the CMB,

$$LiH + \gamma \rightarrow Li + H \tag{41}$$

is highly effective and keeps the LiH abundance very small. At lower redshifts, this process becomes ineffective due to the redshifting of the CMB, and most of the LiH is instead destroyed by the reaction

$$LiH + H \rightarrow Li + H_2, \tag{42}$$

which work by Defazio et al. (2005) has confirmed remains effective even at low gas temperatures.

Since LiH forms slowly, but is destroyed rapidly, it is clear that the equilibrium abundance of LiH will be small. It is further suppressed by the fact that, as we shall see in the next section, most of the lithium in the pregalactic gas is in the form of Li$^+$ and not Li. The most recent calculations of the pregalactic LiH abundance yield values smaller than 10^{-17} (Bovino et al., 2011c), some seven orders of magnitude smaller than the cosmological lithium abundance, and far too small to affect the spectrum of the CMB.

3.3 Complications

3.3.1 Spectral Distortion of the CMB

In this section, we have so far implicitly assumed that we can treat the CMB as a perfect blackbody. However, as we have already seen in Section 2, this is not entirely accurate—the spectrum of the CMB is distorted by the photons emitted during cosmological recombination, which increase the strength of the background at emission-frame photon energies $E \leq 10.2\,eV$. An important consequence of this is that photodissociation rates estimated assuming that the CMB is a perfect blackbody typically underestimate the true photodissociation rates at low redshift, often by a large factor.

The effect of these distortion photons on the chemical evolution of pregalactic gas was first investigated by Switzer and Hirata (2005), who

studied their effect on the balance between Li and Li^+. In the absence of the distortion photons, lithium photoionization would become ineffective at a redshift $z \sim 500$, leading to a dramatic increase in the abundance of neutral lithium. Previous studies by Loeb (2001), Zaldarriaga and Loeb (2002), and Stancil et al. (2002) had shown that in this case, scattering of CMB photons by the $6708 \text{\AA}$ resonance line of neutral lithium would produce a detectable frequency-dependent anisotropy of the CMB at an observed wavelength of around 300 μm. However, Switzer and Hirata (2005) showed that if one accounted for the distortion photons, then the resulting lithium photoionization rate would remain large for significantly longer, and the abundance of neutral lithium would be suppressed by several orders of magnitude, meaning that the lithium signal would no longer be detectable.
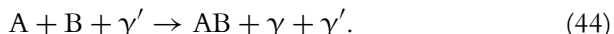
A more comprehensive study of the effects of the distortion photons was carried out by Hirata and Padmanabhan (2006). They showed that although the additional photons have energies that are too low to dissociate H_2 directly, they would nevertheless act to reduce the H_2 abundance in the pregalactic gas by causing significant additional photodestruction of the H^- and H_2^+ ions. The effect on the H^- is particularly important and results in a reduction of the final H_2 abundance by a factor of four in comparison with the value predicted by a model that treats the CMB as a perfect blackbody.

3.3.2 Stimulated Radiative Association

Another way in which the CMB can influence pregalactic chemistry is by enhancing the rate of radiative processes such as radiative association. The basic idea is simple. A radiative association reaction of the form

$$A + B \rightarrow AB + \gamma \qquad (43)$$

typically involves spontaneous emission of a photon during the collision process, which stabilizes the product AB by removing energy from the system. However, the same reaction can also occur by stimulated emission of a photon, that is,

$$A + B + \gamma' \rightarrow AB + \gamma + \gamma'. \qquad (44)$$

For this to be competitive with spontaneous radiative association, there must be a sufficiently high number density of photons of the correct frequency. So in most circumstances, this process is ineffective and is ignored. In the early Universe, however, the CMB provides an abundant source of energetic photons, and in some circumstances, stimulated radiative association is no longer negligible.

The influence of stimulated radiative association on the formation rates for a number of different species has been examined in the literature. Studies exist for H^- (Miyake et al., 2010; Stancil and Dalgarno, 1998), Li^- (Stancil and Dalgarno, 1998), HD (Dickinson, 2005; Stancil and Dalgarno, 1997b), LiH (Stancil and Dalgarno, 1997a), HeH^+ (Zygelman et al., 1998), and $LiHe^+$ (Bovino et al., 2011a), and we refer the reader to these references for full details of the calculations. However, one general result of these studies is that a significant enhancement in the formation rate of these molecules and ions is typically found only when the radiation temperature is large (i.e., $T_r \gg 1000$ K). When this is the case, photodestruction of these species by the CMB will also be highly effective, and so we would expect them to have very small fractional abundances. Therefore, although stimulated radiative association is an important process to understand if one is interested in the evolution of molecular species in the very high redshift, photodissociation dominated regime, it has almost no influence on the chemical evolution of the pregalactic gas at lower redshifts.
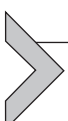
3.3.3 Influence of Rotational and Vibrational Excitation

A final complication that arises in our study of the chemical evolution of the pregalactic gas is the fact that it is often not a good approximation to treat the molecules and molecular ions that form in the gas as being in LTE. Because the density of the pregalactic gas is relatively low, collisional excitation of rotational and vibrational energy levels of these species is often unable to compete with radiative de-excitation of these same levels, leading to level population distributions that differ significantly from those that would be present in LTE. Of particular importance is the internal state of the H_2^+ ions that form in the gas. Galli and Palla (1998) examined the evolution of the H_2^+ abundance with redshift in three simplified cases: one in which all of the H_2^+ ions were assumed to be in the $v = 0$ vibrational ground state, a second in which they were all assumed to be in the $v = 9$ excited vibrational state, and a third in which LTE level populations were assumed. They showed that the evolution of the H_2^+ abundance at $z > 200$ was very sensitive to this choice, with far more H_2^+ forming at early times in the $v = 0$ case than in the other two cases. This also had a pronounced effect on the final, low z H_2 abundance in the pregalactic gas, which is of order 10^{-4} in the $v = 0$ case compared to a value of order 10^{-6} in the other two cases. Galli and Palla (1998) considered that the $v = 0$ case was unlikely to be a good representation of reality, owing to the influence of the CMB on the H_2^+ level populations, but were unable to perform a more detailed

calculation due to the absence of sufficient vibrational-state-resolved data on the reactions primarily responsible for forming and destroying H_2^+, a situation that was also noted by Lepp et al. (2002) to be a major obstacle to modeling the pregalactic H_2^+ abundance accurately.

The issue of the vibrational excitation of H_2^+ was revisited by Hirata and Padmanabhan (2006), who noted that H_2^+ ions formed via radiative association (reaction 15) would be created preferentially in highly excited vibrational levels. They derived values for the radiation association rate and photodissociation rate for each rotational–vibrational level of H_2^+ and used these values to model the evolution with redshift of the H_2^+ abundance. The effect of this improved treatment was to significantly decrease the equilibrium abundance of H_2^+ compared to the value calculated if one assumes LTE level populations for the H_2^+. This in turn decreased the amount of H_2 produced in the gas at redshifts $z \gg 300$. At $z \lesssim 300$, however, production of H_2^+ in the gas began to be dominated by reaction (18), which is not expected to produce highly vibrationally excited ions, and so at $z < 300$, the influence of the vibrational excitation on the amount of H_2 produced in the gas becomes very small.

More recently, Coppola et al. (2011) have presented the results of a new calculation of the chemical evolution of the pregalactic gas that accounts for the populations of every vibrational level of H_2^+ and H_2. They confirm the finding by Hirata and Padmanabhan (2006) that formation of H_2^+ by radiative association leads to a highly non-LTE distribution of level populations for that ion, and show that this result is not significantly affected if one includes a number of collisional excitation and de-excitation processes that were omitted from the Hirata and Padmanabhan (2006) calculation.

4. POPULATION III STAR FORMATION

4.1 The Assembly of the First Protogalaxies

At the redshift of recombination, the distribution of matter in the Universe is very close to homogeneous. Small perturbations exist in the CDM distribution, with typical amplitudes of order 10^{-3}–10^{-4}, resulting in even smaller perturbations in the radiation component, with amplitudes on the order of 10^{-5}. At this epoch, linear perturbation theory gives one an accurate guide to the behavior of the CDM density perturbations, and it is relatively straightforward to show that the amplitude of a simple plane-wave

perturbation will grow as $\delta \propto D_+(z)$, where D_+ is the linear growth factor, given by (Hamilton, 2001)

$$D_+(z) = \frac{1}{1+z} \frac{5\Omega_\mathrm{m}}{2} \int_0^1 \frac{\mathrm{d}a}{a^3 H'^3}. \tag{45}$$

Here $H' \equiv H/H_0$ is a normalized version of the Hubble parameter.

Eventually, however, the amplitude of the perturbations grows to a point at which they are too large to be treated with a simple linear approximation. The CDM density distribution begins to evolve nonlinearly, with localized regions undergoing gravitational collapse, forming condensed, quasi-spherical structures in virial equilibrium that are commonly referred to in the astrophysical literature as dark matter halos. The minimum mass of these structures is set by the requirement that their escape velocity be larger than the typical velocity dispersion of the dark matter particles, but in most CDM models this minimum mass is very small, of the order of a few times the mass of the Earth (Green et al., 2005). On scales larger than this minimum mass, the mass function of dark matter halos is described fairly accurately by the so-called Press–Schechter mass function (Bond et al., 1991; Press and Schechter, 1974)

$$N(M, z)\mathrm{d}M = \sqrt{\frac{2}{\pi}} \frac{\rho_0(z)}{M} \left| \frac{\mathrm{d}\nu(z)}{\mathrm{d}M} \right| \exp\left[-\frac{\nu^2(z)}{2} \right] \mathrm{d}M, \tag{46}$$

where $N(M, z)\mathrm{d}M$ is the number density of halos with masses in the range M to $M + \mathrm{d}M$ at a redshift z and $\rho_0(z)$ is the corresponding mean matter density in units of mass density. The term $\nu(z) = \delta_\mathrm{c}/[D_+(z)\sigma(M)]$, where $\sigma(M)$ is the standard deviation of the fluctuations in the linear density field, calculated for a field smoothed on a mass scale M, and δ_c is a critical overdensity, typically taken to be $\delta_\mathrm{c} = 1.69$ (Press and Schechter, 1974). Equation (46) shows us that the halo mass function has little dependence on ν when $\nu \ll 1$, but that it falls off exponentially with ν^2 when $\nu \gtrsim 1$. In the CDM model, $\sigma(M)$ increases as we consider smaller and smaller masses M, because this corresponds to smoothing the density field on successively smaller length scales, allowing an increasing number of short wavelength fluctuations to contribute to the standard deviation. Large values of ν correspond to small values of $\sigma(M)$ and therefore to large halo masses. At any given redshift, we can identify a characteristic halo mass corresponding to the mass above which the number density of halos begins to decline exponentially, that is, the mass for which $\nu = 1$. As we move to lower redshifts, $D_+(z)$ increases, meaning

that a smaller $\sigma(M)$ is required to produce $\nu \approx 1$. One therefore finds that in this model, the characteristic halo mass increases with decreasing redshift.

So far, we have only considered the behavior of the nonbaryonic dark matter. If we now turn our attention to the behavior of the baryonic matter (henceforth simply "gas"), we find that although there is far more nonbaryonic dark matter than there is gas, the gas does not simply trace the dark matter on small scales. There are two reasons for this. First, the gas pressure provides support against gravitational collapse on short length scales. The critical length scale on which the force due to the gas pressure exactly balances the force due to gravity is known as the Jeans length. In the unperturbed pregalactic gas, it is given in physical (i.e., noncomoving) units by

$$\lambda_J = c_s \sqrt{\frac{\pi}{G\rho_0}}, \tag{47}$$

where c_s is the sound speed of the gas. We can associate a mass with this critical length scale by taking the mass within a sphere of radius $\lambda_J/2$ (Barkana and Loeb, 2001), yielding a quantity known as the Jeans mass

$$M_J = \frac{4\pi}{3} \rho_0 \left(\frac{\lambda_J}{2}\right)^3. \tag{48}$$

If we assume that the sound speed to be used in Eq. (47) is the current value,[9] then it is simple to show that at redshifts $z \gg 100$, where Compton scattering keeps the gas temperature coupled to the CMB temperature, the Jeans mass is given by (Barkana and Loeb, 2001)

$$M_J = 1.35 \times 10^5 \left(\frac{\Omega_m h^2}{0.15}\right)^{-1/2} M_\odot, \tag{49}$$

where $M_\odot$ is the mass of the Sun. In this regime, M_J is independent of redshift, while at $z \ll 100$, where Compton scattering is no longer able to couple the gas temperature to the radiation temperature, the Jeans mass is given instead by

$$M_J = 5.18 \times 10^3 \left(\frac{\Omega_m h^2}{0.15}\right)^{-1/2} \left(\frac{\Omega_b h^2}{0.026}\right)^{-3/5} \left(\frac{1+z}{10}\right)^{3/2} M_\odot. \tag{50}$$

---

[9] A more detailed analysis that properly accounts for the effects of spatial and temporal variations in c_s is given in Barkana and Loeb (2005c) and Naoz and Barkana (2005).

Note that for Eqs. (49) and (50), the terms in parentheses are typically of order unity. We use this convention intermittently throughout the rest of this chapter and leave it as an exercise for the reader to determine when.

The second important effect that acts to prevent collapse on small scales is the coherent streaming of the gas with respect to the dark matter. The strong coupling between gas and radiation prior to recombination, together with the small anisotropies that exist in the matter and radiation distributions, leads to the gas developing a nonzero velocity relative to the dark matter. A small fraction of this relative velocity persists even after recombination (Tseliakhovich and Hirata, 2010). The resulting streaming motions are supersonic, with a root-mean-squared (RMS) velocity of roughly $30 \, \mathrm{km \, s^{-1}}$ at the end of the recombination epoch, and a coherence length of several comoving Mpc. At lower redshifts, the RMS velocity of the streaming motions declines as $v_{\mathrm{RMS}} \propto (1 + z)$; but because the sound speed of the gas also decreases as we move to lower redshifts, these motions remain supersonic for a considerable period. Tseliakhovich et al. (2011) showed that one important consequence of the streaming would be to prevent gas from being accumulated within low mass dark matter halos, as the velocity of the gas with respect to the dark matter would be larger than the escape velocity of the lowest mass halos. They found that in a representative portion of the pregalactic gas, the critical mass at which the accumulation of gas would become possible was roughly $10^5 \, M_\odot$, somewhat larger than the Jeans mass at low redshift, as can be seen from Eq. (50) above.

Thus, the first structures that we might reasonably think of as protogalaxies—condensed, virialized structures containing both gas *and* dark matter—are simply the first dark matter halos to assemble that have masses greater than this critical mass of $10^5 \, M_\odot$. What is more, the Press–Schechter formalism allows us to determine the redshift at which such protogalaxies become reasonably common; that is, the redshift at which the comoving number density of such protogalaxies first exceeds $1 \, h^3 \, \mathrm{Mpc^{-3}}$. This occurs at a redshift $z \sim 30$ (Reed et al., 2007).

As the gas accumulates in these first protogalaxies, it is heated up by adiabatic compression and shocks up to the virial temperature of the halo (i.e., the temperature at which the gas would be in virial equilibrium with total thermal plus kinetic energy $K = |W|/2$, where W is the potential energy of the halo). At these redshifts, this is given approximately by (Barkana and Loeb, 2001)

$$T_{\text{vir}} = 4 \times 10^4 \left(\frac{M}{10^8 \, h^{-1} \, M_\odot} \right)^{2/3} \Omega_{\text{m}}^{1/3} \left(\frac{1+z}{10} \right) \text{K}, \qquad (51)$$

where M is the halo mass and z is the formation redshift, which for a $10^5 \, M_\odot$ halo assembling at $z = 30$ yields $T_{\text{vir}} \simeq 600 \, \text{K}$.

At this temperature, cooling by electronic excitation of atomic hydrogen or helium is ineffective. One must instead rely on molecular cooling, particularly that coming from molecular hydrogen. The cooling time of the gas (i.e., the time required for it to significantly reduce its temperature) is therefore given by

$$t_{\text{cool}} = \frac{n k_B T}{\Lambda_{\text{H}_2} n_{\text{H}_2}}, \qquad (52)$$

where Λ_{H_2} is the cooling rate per H_2 molecule and n_{H_2} is the number density of H_2 molecules. At $T \sim 600 \, \text{K}$ and $n \sim 1 \, \text{cm}^{-3}$ (the mean gas number density within a dark matter halo forming at $z = 30$), the cooling rate per H_2 molecule in a primarily atomic gas is given by $\Lambda_{\text{H}_2} \sim 9 \times 10^{-26} \, \text{erg} \, \text{s}^{-1} \, \text{molecule}^{-1}$ (see, e.g., Glover and Abel, 2008). Substituting this value into Eq. (52), we obtain

$$t_{\text{cool}} \sim \frac{3 \times 10^4}{x_{\text{H}_2}} \text{ year}. \qquad (53)$$

Comparing this cooling time to the expansion timescale of the Universe, t_{H}, defined in Eq. (12), we find that $t_{\text{cool}} < t_{\text{H}}$ only if $x_{\text{H}_2} > 2 \times 10^{-4}$. This is much larger than the value of order 10^{-6} produced in the diffuse pregalactic gas prior to the formation of the first protogalaxies (e.g., Fig. 9), demonstrating that in order for the gas to cool effectively (an essential requirement if star formation is to take place), it must be able to form a substantially larger quantity of H_2 during the assembly of the protogalaxy.

We can gain considerable insight into the process of H_2 formation in the protogalactic gas by considering a very simple model for the H_2 chemistry first introduced by Tegmark et al. (1997). We begin by assuming that radiative recombination of H^+ is the only process that significantly alters the electron abundance in the gas, and write the rate of change of the electron number density as

$$\frac{\text{d}n_e}{\text{d}t} = -k_{\text{rec}} n_e n_{\text{H}^+}, \qquad (54)$$

where k_{rec} is the radiative recombination rate coefficient. If we assume that ionized hydrogen is the only source of free electrons, implying that

$n_e = n_{H^+}$, and that the temperature and density remain roughly constant during the period that we are considering, then we can easily solve for the time evolution of the electron abundance:

$$x_e = \frac{x_{e,0}}{1 + k_{rec} n t x_{e,0}}, \tag{55}$$

where t is time and $x_{e,0}$ is the initial value of x_e.

Assuming that all the H_2 forms via the H^- pathway described in the previous section, that the H^- ion formation is the rate-limiting step, and that other reactions destroy only a small proportion of the H^- ions (e.g., mutual neutralization with H^+), then we can write the rate of change of the H_2 fractional abundance as

$$\frac{dx_{H_2}}{dt} = k_{ra} x_e n_H \tag{56}$$

where k_{ra} is the rate coefficient for the radiative association reaction that forms H^- (reaction 13). Provided that $x_{e,0} \ll 1$, as is the case during the assembly of the first protogalaxies, and that the density and temperature again remain roughly constant, then we can solve for the time evolution of the H_2 fraction:

$$x_{H_2} = \frac{k_{ra}}{k_{rec}} \ln(1 + t/t_{rec}), \tag{57}$$

where $t_{rec} = 1/(k_{rec} n x_{e,0})$ is the recombination time. The growth of the H_2 fraction is therefore logarithmic in time, with most of the H_2 forming within the first few recombination times, and with H_2 formation at later times being strongly suppressed due to the scarcity of free electrons.

This simple analysis shows that the most important factor for determining the final H_2 abundance is the ratio of the radiative association rate coefficient, k_{ra}, to the recombination rate coefficient, k_{rec}, since for times on the order of a few recombination times, the logarithmic term is of order one. Both of these rate coefficients are known to a high degree of accuracy, and detailed functional fits for their values as a function of temperature can be found in Glover and Savin (2009). For the purposes of discussion, however, it is more convenient to use the simpler (albeit somewhat less accurate) power-law fits given in Hutchins (1976):

$$k_{ra} = 1.83 \times 10^{-18} T^{0.8779} \text{ cm}^3 \text{ s}^{-1}, \tag{58}$$

$$k_{rec} = 1.88 \times 10^{-10} T^{-0.644} \text{ cm}^3 \text{ s}^{-1}. \tag{59}$$

Combining these, we find that

$$\frac{k_{\mathrm{ra}}}{k_{\mathrm{rec}}} \simeq 10^{-8}\,T^{1.5219}. \tag{60}$$

From this, we see that the amount of H_2 formed in the gas is a strong function of the gas temperature, and also that the final fractional abundance of H_2 is typically small: for $T \sim 600\,\mathrm{K}$, the virial temperature of the earliest protogalaxies, we have $x_{H_2} \sim 10^{-4}$ at $t \sim t_{\mathrm{rec}}$. Nevertheless, if we compare this value with the value derived above for the amount of H_2 required to cool the gas within a Hubble time, we see that they are roughly comparable.

   We can therefore conclude that the quantity of H_2 that forms within the first protogalaxies is enough to cool the gas, thereby allowing it to undergo further gravitational collapse. The physical and chemical evolution of the gas during this further collapse phase, and its final outcome are discussed below. Space constraints limit our discussion of this complicated topic to the most important details. More comprehensive reviews can be found in Bromm and Yoshida (2011), Glover (2013), and Bromm (2013).

4.2 Gravitational Collapse and Star Formation

4.2.1 The Initial Collapse Phase

In Section 4.1, we saw that gas in protogalaxies with virial temperatures $T_{\mathrm{vir}} \gtrsim 600\,\mathrm{K}$, corresponding to masses $M \gtrsim 10^5\,\mathrm{M}_\odot$, is able to form enough H_2 *in situ* to cool within a Hubble time. As the gas cools and its thermal pressure decreases, it flows toward the center of the protogalaxy and is compressed further as it does. In order for the cooling gas to become unstable to gravitational fragmentation, its mass must exceed the local value of the Jeans mass. Combining Eqs. (47) and (48), we can show that this scales as $M_{\mathrm{J}} \propto c_{\mathrm{s}}^3 \rho^{-1/2}$. Since the sound speed of the gas scales with the temperature as $c_{\mathrm{s}} \propto T^{1/2}$, this means that the Jeans mass scales with density and temperature of the gas as $M_{\mathrm{J}} \propto T^{3/2} \rho_0^{-1/2}$. The Jeans mass therefore decreases rapidly while the gas is cooling.

   Two effects, both related to the microphysics of H_2, eventually combine to dramatically slow the decrease in M_{J}. First, as the gas temperature approaches $T \sim 200\,\mathrm{K}$, H_2 cooling becomes increasingly ineffective, owing to the large energy separation $E_{JJ'}$ between the H_2 rotational ground level J' and the first accessible excited rotational level J giving $E_{20}/k_{\mathrm{B}} = 510\,\mathrm{K}$ for *para*-hydrogen and $E_{31}/k_{\mathrm{B}} = 845\,\mathrm{K}$ for *ortho*-hydrogen. When $T \sim 200\,\mathrm{K}$ or less, the only collision partners with enough energy to excite these transitions are found in the high energy tail of the Maxwellian

velocity distribution, and their abundance therefore falls off exponentially with decreasing temperature. Second, as the number density of the gas approaches a critical density $n_{\text{crit}} \sim 10^4 \, \text{cm}^{-3}$, the level populations of the excited rotational and vibrational states of H_2 approach their LTE values. We can write the cooling rate per unit volume as

$$\Lambda_{H_2} = \sum_{i,j>i} A_{ji} E_{ji} f_j n_{H_2}, \qquad (61)$$

where A_{ji} is the spontaneous radiative transition rate from level j to level i, E_{ji} is the energy separation of the two levels, f_j is the fraction of all of the H_2 molecules that are in level j, and where the sum includes all possible radiative transitions between bound states of the H_2 molecule. At densities $n \ll n_{\text{crit}}$, the level populations depend on both the temperature of the gas and the number density of collision partners. Consequently, $f_j \propto n_{Hn}$, and $\Lambda_{H_2} \propto x_{H_2} n_{Hn}^2$. As x_{H_2} is largely independent of density during this phase, Λ_{H_2} scales as the square of the density. Above n_{crit}, however, the H_2 populations have their LTE values, which are functions only of temperature and not of density. In this limit, therefore, the cooling rate per unit volume scales only linearly with density: $\Lambda_{H_2} \propto n_{H_2}$. Compressional heating of gravitationally collapsing gas occurs at a rate that is roughly $n_{Hn}^{3/2}$, and so the cooling rate increases with increasing density more slowly than the heating rate at densities $n_{Hn} > n_{\text{crit}}$. As a result, the gas temperature begins to increase once the density exceeds n_{crit}.

Together, these effects yield a characteristic density and temperature for the collapsing gas. As the gas approaches this point, it enters what has been described as a "loitering" phase (Bromm et al., 2002), during which cold gas accumulates in the center of the halo but only slowly increases its density. This loitering phase ends once the mass of cold gas that has accumulated exceeds the local value of the Jeans mass, given in this case by (Abel et al., 2002)
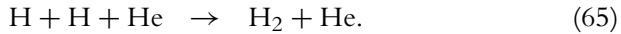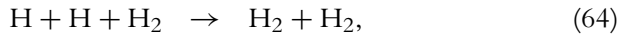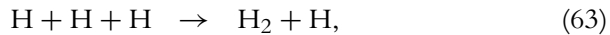
$$M_J \simeq 40 \, T^{3/2} n_{Hn}^{-1/2} \, M_\odot, \qquad (62)$$

which for $n_{Hn} \sim 10^4 \, \text{cm}^{-3}$ and $T \sim 200$ K yields $M_J \sim 1000 \, M_\odot$. Once the mass of cold gas exceeds this value, it begins to collapse more rapidly.

4.2.2 Three-Body H_2 Formation

The next notable event occurs once the number density of the gas reaches a value of around 10^8–$10^9 \, \text{cm}^{-3}$. At this density, a new formation pathway

for H_2 becomes viable—formation via three-body association. The main reactions involved are (Palla et al., 1983)

$$H + H + H \quad \rightarrow \quad H_2 + H, \tag{63}$$

$$H + H + H_2 \quad \rightarrow \quad H_2 + H_2, \tag{64}$$

$$H + H + He \quad \rightarrow \quad H_2 + He. \tag{65}$$

The first of these typically dominates. At low densities, the small size of the rate coefficients for these reactions means that the time required to convert even a small fraction of the hydrogen from H to H_2 is very long. However, as the density increases, this timescale decreases as $t \sim n_{Hn}^{-2}$, and at sufficiently high densities, these reactions become very efficient and quickly convert most of the atomic hydrogen to H_2.

During this three-body H_2 formation phase, a large amount of chemical energy is released, most of which goes into heating the gas. Each time an H_2 molecule forms via one of the three-body reactions, its binding energy of 4.48 eV is a carried away by the reaction products in the form of rotational and vibrational excitation and/or translational kinetic energy. At these high densities, the individual atoms and molecules undergo many collisions and quickly thermalize, resulting in essentially all of the chemical energy being converted into heat. Therefore, even though the abundance of the dominant coolant (namely, H_2) increases by two to three orders of magnitude, the gas typically does not cool significantly during this process, owing to the chemical heat input. In fact, the gas temperature often rises slightly at this time.

Unfortunately, the behavior of the gas during this portion of its evolution remains somewhat uncertain, owing to the large uncertainty that exists regarding the correct value for the rate coefficient for reaction (63). At the temperatures of interest ($T \sim 1000$ K), published values for the rate coefficient for this reaction disagree by almost two orders of magnitude (Forrey, 2013; Glover, 2008). The impact of this uncertainty on the dynamical evolution of the gas was examined by Turk et al. (2011), who showed that it has pronounced effects on the morphology of the gas and on its velocity structure. Simulations in which a low value was used for the three-body rate coefficient find that the gas proceeds relatively slowly and develops a spherical structure, whereas using a high value results in gravitational collapse that occurs more rapidly and molecular gas which develops a much more flattened, filamentary structure. Significant differences are also apparent in the infall velocities and the degree of rotational support. A more recent study by Bovino et al. (2013) finds that the link between

the morphology of the collapse and the size of the rate coefficient is less straightforward than in the Turk et al. study, but confirms the fact that the behavior is highly sensitive to the choice of rate coefficient. Our ability to understand the fragmentation of the gas and the resulting mass distribution of the first stars is considerably hindered by this chemical uncertainty.

4.2.3 Transition to the Optically Thick Regime

Once the collapsing gas reaches a density of around $10^{10}\,\mathrm{cm^{-3}}$, the H_2 emission lines that provide most of the cooling start to become optically thick (Ripamonti and Abel, 2004). This reduces the effectiveness of H_2 cooling, leading to a further rise in the gas temperature. However, detailed one-dimensional (1D) models of the thermal and chemical evolution of the gas during this phase of the collapse show that although the optical depth of the H_2 emission lines becomes large at the line centers, the low continuum opacity of the gas allows photons to continue to escape through the wings of the lines (see, e.g., Omukai and Nishi, 1998; Omukai et al., 1998; Ripamonti et al., 2002). The result is that although the H_2 cooling rate is reduced, it is suppressed far less than one might naively expect.

In full three-dimensional (3D) hydrodynamical simulations, a full treatment of the radiative transfer of the photons emitted by the H_2 molecules is impractical, owing to the very high computational expense. Consequently, we must rely on more approximate treatments. There are two approximations in general use. One of these was introduced by Ripamonti and Abel (2004) and models the suppression in the H_2 cooling rate with a simple density-dependent suppression factor f_τ via

$$\Lambda_{H_2,thick} = f_\tau \Lambda_{H_2,thin}, \tag{66}$$

here $\Lambda_{H_2,thick}$ is the optically thick H_2 cooling rate, $\Lambda_{H_2,thin}$ is the optically thin cooling rate, and

$$f_\tau = \min\left[1, \left(\frac{n_{Hn}}{n_0}\right)^{-0.45}\right], \tag{67}$$

where $n_0 = 8 \times 10^9\,\mathrm{cm^{-3}}$ is the density at which the H_2 ro–vibrational lines start to become optically thick. Ripamonti and Abel (2004) found that this expression was a good approximation to the results of the full radiative transfer model used in the 1D models of Ripamonti et al. (2002). However, it is unclear whether this approximation will remain appropriate if the geometry of the gas deviates strongly from spherical symmetry, as will happen if, for example, an accretion disk forms.

The other common approach, first used by Yoshida et al. (2006), is an escape probability technique based on the large velocity gradient approximation (Sobolev, 1960). Strictly speaking, this approximation is valid only when the Sobolev length—the ratio of the thermal velocity to the velocity gradient—is much smaller than the characteristic length scales associated with changes in the density, temperature, or chemical makeup of the gas. This is easy to satisfy if the collapse is highly supersonic, but is harder to justify in the present context, as the high gas temperature implies a high sound speed and a collapse speed that is comparable to or less than the sound speed. However, Yoshida et al. (2006) show that in practice, the cooling rate predicted by the Sobolev approximation is in reasonable agreement with that found in 1D studies that solve the full radiative transfer problem with approximations (Omukai and Nishi, 1998).

In a recent study, Turk et al. (2011) compared these two approaches and showed that they yield similar values for the H_2 cooling rate during the initial collapse of the gas, with differences of at most a factor of two. Whether this level of agreement persists at later times remains unclear.

4.2.4 Cooling at Very High Densities

Once the gas density reaches $n_{Hn} \sim 10^{14}$ cm^{-3}, a process known as collision-induced emission (CIE) begins to provide the bulk of the cooling. One of the main factors that limits the effectiveness of H_2 as a coolant is the fact that it has no dipole moment and hence can only emit or absorb radiation through quadrupole transitions. However, during collisions between two H_2 molecules (or between an H_2 molecule and a hydrogen or helium atom), the collision complex does have a dipole moment and can therefore emit or absorb radiation via dipole transitions. If radiation is absorbed, then this process is termed collision-induced absorption, while if it is emitted, we refer to it as CIE (see Frommhold, 1993 for a more detailed discussion).

Since the collision lifetime is very short, the probability of photon emission during any given collision is small, and at low gas densities, CIE cooling is unimportant. However, it becomes increasingly important as the gas evolves to higher densities since the associated cooling rate scales as the square of the H_2 number density over a very wide range of densities. For comparison, the H_2 ro–vibrational cooling rate scales only linearly with molecular density once the H_2 level populations reach LTE, at $n_{Hn} \sim 10^4$ cm^{-3}. Moreover, the high optical depths that develop in the H_2 rotational and vibrational lines do not suppress CIE cooling, which occurs through a set of lines that are so broad that they essentially merge

into a continuum. Together, these factors allow CIE cooling to eventually dominate over H_2 line cooling (Omukai and Nishi, 1998; Ripamonti and Abel, 2004; Ripamonti et al., 2002).

However, the phase of the collapse dominated by CIE cooling is short. Primordial gas becomes optically thick in the continuum once its density exceeds $n_{Hn} \sim 10^{16}$ cm^{-3} (Omukai and Nishi, 1998; Ripamonti and Abel, 2004), due primarily to collision–induced absorption, and this strongly suppresses any further radiative cooling. Once this occurs, chemical changes are the only process that can limit the inevitable increase in the temperature of the gas.

When the gas temperature exceeds a few thousand Kelvin, H_2 begins to dissociate. Every time an H_2 molecule is collisionally dissociated, the 4.48 eV binding energy of the molecule is removed from the gas. So, once the gas reaches a temperature at which H_2 dissociates, any further increase in temperature is greatly hampered by the fact that most of the available energy goes into dissociating the H_2 rather than raising the temperature. Of course, H_2 dissociation is effective at limiting the temperature increase only for as long as H_2 remains in the gas. Once the H_2 has all been destroyed, there is nothing to stop the gas from heating up further. The evolution becomes adiabatic, and the thermal pressure within the collapsing core eventually becomes large enough to halt the collapse. At the point at which this occurs, the size of the dense core is around 0.1 AU, its mass around 0.01 $M_\odot$, and its mean density of order 10^{20} cm^{-3} (Yoshida et al., 2008). The dense core is bounded by a strong accretion shock. This pressure-supported, shock–bounded core is the first structure that we can identify as a true protostar, and we discuss its later evolution below.

4.2.5 Influence of Other Coolants

Given the limited effectiveness of H_2 as a coolant of primordial gas, it is reasonable to ask whether cooling from any other molecules or molecular ions may become competitive with H_2. One important such alternative coolant is deuterated molecular hydrogen, HD. This molecule has a small but nonzero dipole moment, giving it radiative transition rates that are somewhat larger than those of H_2, resulting in a critical density $n_{crit} \sim 10^6$ cm^{-3}. Unlike H_2, however, HD is not separated into *ortho* and *para* states, and so the lowest energy transition accessible from the ground state is the $J = 1$ to $J' = 0$ rotational transition, with an energy $E_{10}/k_B = 128$ K. Although the cosmological ratio of deuterium to hydrogen is small, the ratio of HD to H_2 can be significantly boosted in low temperature gas by chemical fractionation, driven by reactions (33) and (34). In equilibrium,
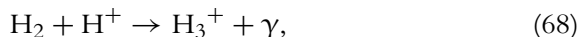
the HD/H$_2$ ratio is given by Eq. (36) and can be tens or hundreds of times larger than the cosmological deuterium-to-hydrogen ratio, provided that the temperature is low enough. In cold, low-density pregalactic gas, the time taken to reach this equilibrium state can be very long, and typically the HD/H$_2$ ratio freezes out at a value that is a factor of 30–40 times larger than the cosmological deuterium-to-hydrogen ratio. In the much denser environment within a protogalaxy, however, equilibrium is reached far more rapidly, and hence even larger enhancements of the HD/H$_2$ ratio are possible.

As the gas gets colder, chemical fractionation causes the fractional abundance of HD to increase. The ratio of the HD and H$_2$ cooling rates per molecule also increases owing to the ineffectiveness of H$_2$ cooling at low temperatures. Together, these effects mean that HD eventually becomes the dominant coolant in the cold gas. In practice, this occurs only once the gas temperature has decreased to $T \sim 150$ K (see, e.g., Glover, 2008), which means that considerable cooling is required *before* HD can take over. Temperatures this low are typically not reached during the gravitational collapse of gas within the very first star-forming minihalos (Bromm et al., 2002), but can be reached in regions that start with an enhanced fractional ionization (for a number of examples, see Greif et al., 2008; Johnson and Bromm, 2006; Kreckel et al., 2010; McGreer and Bryan, 2008; Nagakura and Omukai, 2005; Nakamura and Umemura, 2002; Yoshida et al., 2007). In situations where HD cooling does become important, it is capable of reducing the gas temperature significantly below that reachable by H$_2$ cooling alone, and often brings the temperature down to the CMB temperature. Moreover, the gas remains at this low temperature up to densities of the order of the HD critical density, $n_{\mathrm{Hn}} \sim 10^6$ cm^{-3}. As a result, the characteristic mass of the cold clump of gas that accumulates at the center of the halo is greatly reduced. The characteristic mass is given by the Jeans mass of the gas during the so-called loitering phase, and when HD cooling dominates, this is roughly $M_{\mathrm{J}} \sim 40\,M_{\odot}$, compared to $M_{\mathrm{J}} \sim 1000\,M_{\odot}$ in the H$_2$ dominated case. It is therefore quite possible that the final mass of the protostars formed in this case will be smaller, since the total available mass of cold gas is smaller, although this outcome remains uncertain.

Another alternative primordial coolant that periodically attracts attention is LiH. This molecule at first appears to be a very good candidate for an important high-density coolant, as it has a very large dipole moment, $\mu = 5.888$ debye (Zemke and Stwalley, 1980), and consequently its excited

levels have very short radiative lifetimes. For this reason, it was thought for a long time that LiH would dominate the cooling of primordial gas at very high densities (see, e.g., Lepp and Shull, 1984), despite the low elemental lithium abundance. However, more accurate calculations for the radiative association formation of LiH (reaction 38) have shown that the rate coefficient is much smaller than was assumed in earlier work (Bennett et al., 2003b; Dalgarno et al., 1996; Gianturco and Gori Giorgi, 1997). We also now understand that reaction (42) is an effective destruction mechanism for LiH even in the coldest gas. Together, these factors mean that more recent models of primordial chemistry predict the LiH abundance to be very small. For this reason, LiH is no longer expected to be an important primordial coolant (Glover and Savin, 2009; Mizusawa et al., 2005).

Finally, the role played by cooling from the H_3^+ ion has also attracted attention. This ion has a very large number of excited rotational and vibrational levels that are energetically accessible at the temperatures of interest in primordial gas, and its vibrational levels have much shorter radiative lifetimes than those of H_2 or HD. In LTE, its cooling rate per molecule is roughly 10^9 times larger than that of H_2. It is known to be an important coolant in planetary atmospheres (Miller et al., 2000), and because it does not react with H_2 and is not easily destroyed by atomic hydrogen, its abundance in dense primordial gas could plausibly become quite large (Glover and Savin, 2006). For this reason, Glover and Savin (2009) made a careful study of its effects and showed that the amount of H_3^+ that forms during the gravitational collapse of the gas is very sensitive to the value adopted for the rate coefficient for the radiative association reaction

$$H_2 + H^+ \rightarrow H_3^+ + \gamma, \tag{68}$$

which is uncertain by four orders of magnitude (Gerlich and Horning, 1992; Stancil et al., 1998). However, Glover and Savin (2009) also showed that even if one adopts the largest possible value for the rate of this reaction, the fractional abundance of H_3^+ never quite becomes large enough to become important, and the ion contributes at most a few percent of the total cooling rate.

4.3 Evolution After the Formation of the First Protostar

As we have already discussed, the point at which the first protostar forms, it has a mass of only $0.01\ M_\odot$ (Yoshida et al., 2008). However, it is surrounded by a much larger envelope of dense gas, containing hundreds of solar masses.

The final mass of the protostar therefore has little to do with its initial mass, but is determined instead by what happens to the gas within this surrounding envelope.

Unfortunately, modeling the further evolution of this gas is numerically challenging. The numerical methods commonly used to model astrophysical gas flows work by splitting up the period of time over which the flow is to be simulated into a series of discrete timesteps, and then solving for the change in the system during each timestep. The computational cost of modeling the flow scales linearly with the number of timesteps used, and so ideally one wants to make these steps as large as one can without sacrificing accuracy. However, there is a limit on how large one can make these timesteps without introducing numerical instabilities into the solution that lead to a catastrophic loss of accuracy. This limit is known as the Courant condition and is given by

$$\Delta t \leq \frac{\Delta x}{c_s}, \tag{69}$$

where Δt is the size of the timestep and Δx is the size of a single spatial resolution element (i.e., the minimum size of an object that can be represented in the simulation). In order to model the flow of gas within and immediately around a protostar, Δx must be very small, of the order of the solar radius or smaller. Consequently, the maximum permitted timestep is also very small, of the order of a few thousand seconds. Since the characteristic timescale on which the protostar evolves is measured in the thousands of years, the number of timesteps required in order to model this evolution directly within the simulations is impractically large.

For this reason, most numerical simulations of the formation of Population III stars stop at or before the point at which the first protostar forms, leaving the ultimate fate of this protostar somewhat speculative. The most popular hypothesis, stemming from the work of Abel et al. (2002) and Bromm et al. (2002), notes that there is little or no evidence for fragmentation of the gas during the initial collapse, and hence it is plausible that the gas in the infalling envelope will also remain stable against gravitational collapse. In this picture, only a single star forms in each minihalo (or occasionally a binary system; see, e.g., Turk et al. 2009), and the final mass of this star is determined by the amount of mass it is able to accrete during its lifetime.

Simple models of the accretion of gas onto the protostar show that it occurs very rapidly, and predict that a Population III protostar that accretes

with 100% efficiency can grow to a mass of anywhere between 20 and 500 $M_\odot$ before it reaches the main sequence, depending on the details of the assembly history of the halo (O'Shea and Norman, 2007). Prior to reaching the mean sequence, the protostar has a large radius (Omukai and Palla, 2003; Stahler et al., 1986). The radiation produced by the protostar therefore is primarily in the form of low-energy optical and infrared photons that heat up the infalling gas, but that do not have sufficient energy to ionize the gas. However, as the protostar contracts onto the main sequence, it starts to generate higher-energy photons. If its mass is greater than about 20 $M_\odot$, then the outer layers of the protostar become sufficiently hot to radiate strongly in the ultraviolet, producing a large number of ionizing photons. Ionization of the gas surrounding the star prevents it from being accreted, and strongly limits its further growth (Hosokawa et al., 2011; McKee and Tan, 2008). This conventional picture of Population III star formation therefore leads one to conclude that all Population III stars should have masses of around 20 $M_\odot$.

In the past few years, however, evidence has been accumulating that this model is an oversimplified picture of what actually happens following the formation of the first protostar. The key development responsible for this revision to our thinking is the advent of a new generation of simulations of Population III star formation that use a technique drawn from the study of present-day star formation to allow the evolution of the gas during the accretion phase to be directly modeled. This technique involves the use of so-called sink particles to represent gravitationally bound and collapsing regions of gas that become smaller than some preselected size scale (Bate et al., 1995). These sink particles can accrete gas from their surroundings and continue to interact gravitationally with the surrounding gas, but allow one to neglect the very small-scale hydrodynamical flows that would otherwise force one to take very small numerical timesteps. This allows the gas flow on larger scales to be modeled for much longer than would otherwise be possible.

High-resolution simulations carried out using sink particles show that after the protostar forms, the surrounding gas settles into a thick, rotationally supported accretion disk (see, e.g., Clark et al., 2011; Greif et al., 2011; Smith et al., 2011; Stacy et al., 2010). Crucially, these studies show that the gas making up the disk retains its H_2, which continues to be the most important coolant. Previous semi-analytical studies of the structure of Population III accretion disks did not account for H_2 cooling and hence found that the disks would be hot, with temperatures $T \sim 6000$ K or higher

(Mayer and Duschl, 2005; Tan and Blackman, 2004; Tan and McKee, 2004). At these temperatures, thermal pressure is highly effective in preventing the onset of gravitational instability, and so these early studies predicted that the accretion disk would remain stable.

When H_2 cooling is included, however, one finds that the disk is much colder ($T \sim 1500$–2000 K) and hence much less stable. Recent simulations show that in this case, the disk grows in mass until it becomes gravitationally unstable. Once unstable, it breaks into multiple fragments, each corresponding to a separate Population III protostar. This process occurs quickly, only 100–200 years after the formation of the initial protostar (Clark et al., 2011). The effects of accretion luminosity (i.e., the energy released as gas accretes into the protostars) have been included in some models and have been shown to be of limited importance— the accretion disk becomes larger and puffier when the effects of the accretion luminosity are accounted for, but nevertheless, the disk still fragments.

The ultimate fate of the protostars that form in these simulations is unclear. The current models suggest that they will form a very dense cluster of protostars with a wide range of masses (Greif et al., 2011, 2012; Smith et al., 2011). Once one or more of the protostars reaches a mass of around $20\,M_\odot$ and settles onto the main sequence, they will ionize the infalling gas in a similar fashion to that predicted in the single-star models, thereby shutting off accretion onto the protostellar cluster (see Stacy et al., 2012 for a first attempt at modeling this numerically). During the evolution of the protostellar cluster, some protostars may be ejected from it due to gravitational three-body interactions. The accretion of gas onto these ejected protostars is very inefficient, and so it is plausible that the final masses of some of these protostars may have been less than the Sun (see, e.g., Greif et al., 2011). This is important, because the lifetime of stars with subsolar masses is very long, and it is therefore conceivable that some of them may have survived until the present day. However, this conclusion is currently highly speculative. The number of ejections and the masses of the ejected objects are both highly sensitive to the details of the numerical treatment of protostellar encounters and mergers, which are treated in a highly approximate fashion in the current simulations. The uncertainties introduced by our poor knowledge of the three-body H_2 formation rate coefficient and by the approximations used to treat optically thick H_2 cooling also need to be reduced or eliminated in order for us to truly trust the predicted outcome of the simulations.

5. THE 21-CM LINE OF ATOMIC HYDROGEN

5.1 Physics of the 21-cm Line

The hydrogen 21-cm line arises from the hyperfine splitting of the H ground state due to the interaction of the magnetic moments of the proton and electron. This splitting leads to two distinct levels separated by an energy $\Delta E = 5.9 \times 10^{-6}$ eV, corresponding to a wavelength of 21.1 cm and a frequency of 1420 MHz. This frequency is one of the most precisely known quantities in astrophysics, having been measured to great accuracy from studies of hydrogen masers (Goldenberg et al., 1960).

The 21-cm line was theoretically predicted by van de Hulst (1945) and has been used as a probe of astrophysics since it was first detected by Ewen and Purcell (1951). Radio telescopes look for emission by warm hydrogen gas within galaxies. Since the line is narrow with a well measured rest frame frequency, it can be used in the local Universe as a probe of the velocity distribution of gas within our galaxy and other nearby galaxies. Observed 21-cm rotation curves are often used to trace galactic dynamics, but traditional observations have been limited to relatively local galaxies.

A new generation of radio telescopes, enabled by progress in technology and computational power, raises exciting prospects for using the 21-cm line as a probe of cosmology. Figure 10 illustrates schematically the evolution of the 21-cm signal with cosmological time, showing both the sky-averaged mean signal and spatial fluctuations. Single dipole experiments, such as EDGES (Bowman and Rogers, 2010), target the mean signal while radio interferometers such as LOFAR,[10] MWA,[11] and PAPER[12] target the fluctuations. In this section, we describe the physics that underlies this signal and explore what 21-cm observations might tell us about the first galaxies. Additional details can be found in Furlanetto et al. (2006b), Morales and Wyithe (2010), and Pritchard and Loeb (2012).

5.1.1 Basic 21-cm Physics

In cosmological contexts, the 21-cm line can be used as a probe of gas along the line of sight to a background radio source. Two types of background radio sources are important for the 21-cm line. First, we may use the CMB as the radio background source. In this case, the 21-cm signal is seen as a spectral distortion to the CMB blackbody at the appropriate redshifted

[10] http://www.lofar.org.
[11] http://www.mwatelescope.org.
[12] http://eor.berkeley.edu.
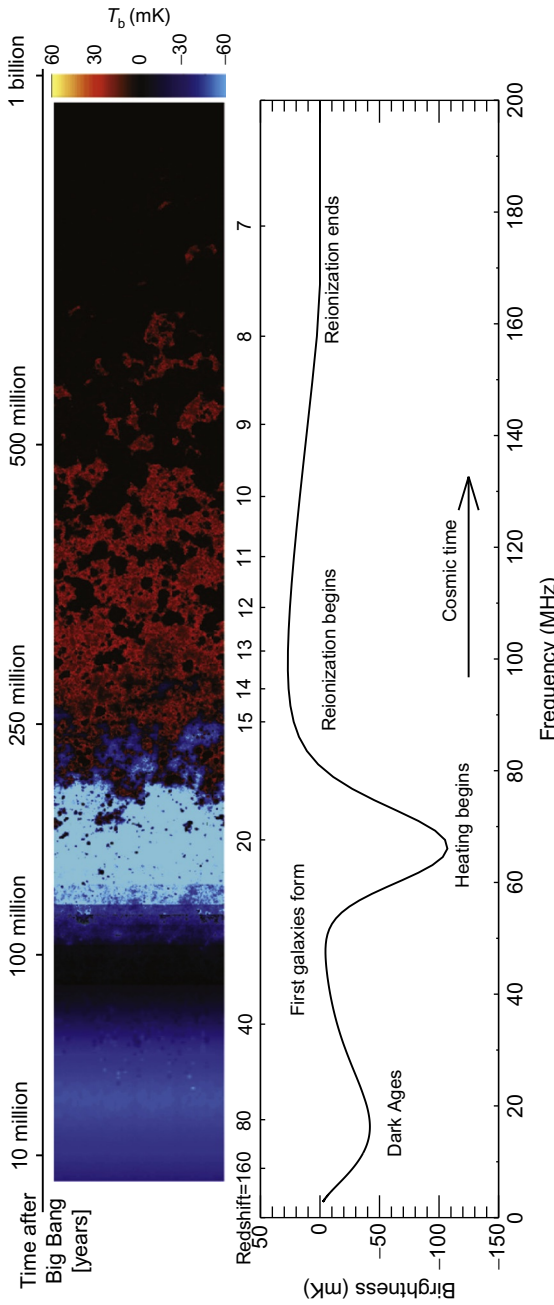
Fig. 10. The theoretical 21-cm cosmic hydrogen signal (Pritchard and Loeb, 2010). *Top panel:* Time evolution of fluctuations in the 21-cm brightness temperature T_b from just before the first stars formed through to the end of the reionization epoch. The coloring indicates the strength of the 21-cm brightness as it evolves through two absorption phases (purple and blue (dark gray and light gray in the print version)), separated by a period (black) where the excitation temperature of the hydrogen 21-cm transition decouples from the temperature of the hydrogen gas, after which it transitions to emission (red (gray in the print version)) and finally disappears (black) owing to the ionization of the hydrogen gas. *Bottom panel:* Corresponding evolution of the sky-averaged 21-cm brightness.

radio frequencies. The distortion forms a diffuse background that can be studied across the whole sky with observations at different frequencies (corresponding to different redshifts) probing different spherical shells of the observable Universe, so that a 3D map of the intervening gas can be constructed.

Alternatively, a radio point source, such as a radio loud quasar, may act as a backlighter. In this case, the source will always be brighter than the weak emission from diffuse hydrogen gas and the gas is seen in absorption against the source. The appearance of lines from clumps of neutral gas at different distances to the source is predicted to lead to a "forest" of lines known as the "21-cm forest" in analogy to the Lyα forest (Carilli et al., 2002; Furlanetto and Loeb, 2002).

The details of the signal depend upon how much neutral hydrogen is present and its excitation state. Here we label the energy levels by $n\,_F L_J$, where n, L, and J are the standard radial, orbital angular momentum, and total angular momentum quantum numbers, and $F = I + J$ is the quantum number obtained from J and the nuclear spin I. As a result of the nuclear spin, the H ground state is split into a lower $1\,_0 S_{1/2}$ hyperfine level and an excited $1\,_1 S_{1/2}$ hyperfine level. We will sometimes refer to these as the $1S$ singlet and triplet levels, respectively.

The excitation state of the neutral H is characterized by an excitation temperature known as the 21-cm spin temperature T_S. It is defined through the ratio between the number densities n_i of hydrogen atoms in the two hyperfine levels (labeled with the subscript 0 for the $1S$ singlet level and 1 for the $1S$ triplet level)

$$n_1/n_0 = (g_1/g_0) \exp(-T_\star/T_S). \qquad (70)$$

Here $(g_1/g_0) = 3$ is the ratio of the statistical degeneracy factors of the two levels. The quantity $T_\star \equiv 2\pi\hbar c/k_B \lambda_{21\,cm} = 0.068\,\mathrm{K}$ where $\hbar$ is Planck's constant divided by 2π, c is the speed of light, and $\lambda_{21\,cm}$ is the wavelength of the H 21-cm transition.

The relevant photon frequencies ν are much smaller than the peak frequency of the CMB blackbody and lie in the Raleigh–Jeans limit. Radio astronomers commonly describe an observed flux by a brightness temperature, equivalent to the temperature a blackbody would have to produce the observed flux. For the flux in the 21-cm line, it is common to consider a differential brightness temperature relative to the radio background. This differential brightness temperature is determined by the optical depth τ of the line and is fixed by the spin temperature of the gas and

the column of gas along the line of sight corresponding to the width of the 21-cm line. The differential brightness temperature is given by (Furlanetto et al., 2006b)

$$\delta T_{\rm b} \quad = \quad \left(\frac{T_{\rm S} - T_{\rm R}}{1 + z} \right) \tau \qquad\qquad (71)$$

$$\approx \quad 27 x_{\rm H\,I} (1 + \delta_{\rm b}) \left(\frac{\Omega_{\rm b} h^2}{0.023} \right) \left(\frac{0.15}{\Omega_{\rm m} h^2} \frac{1 + z}{10} \right)^{1/2}$$

$$\times \left(\frac{T_{\rm S} - T_{\rm R}}{T_{\rm S}} \right) \left[\frac{\partial_{\rm r} v_{\rm r}}{(1 + z) H(z)} \right]^{-1} \quad {\rm mK}. \qquad (72)$$

Here $x_{\rm H\,I}$ is the neutral fraction of hydrogen relative to the total hydrogen nuclei number density, $\delta_{\rm b}$ is the fractional overdensity in baryons, and $T_{\rm R}$ is the brightness temperature of the background source. The final term arises from the gradient of $v_{\rm r}$, the velocity along the line of sight, which connects the line width in frequency to a physical distance.

The key to the detectability of the 21-cm signal hinges on the spin temperature. Only if this temperature deviates from the background temperature will a signal be observable. Three processes determine the spin temperature: (i) absorption (emission) of 21-cm photons from (on top of) the radio background, primarily the CMB; (ii) spin flip inducing collisions with other hydrogen atoms and with protons or electrons; and (iii) resonant scattering of Lyα photons that induce a spin flip via an intermediate excited state. These processes set the spin temperature (Field, 1958)

$$T_{\rm S}^{-1} = \frac{T_{\rm CMB}^{-1} + x_\alpha T_\alpha^{-1} + x_{\rm c} T_{\rm K}^{-1}}{1 + x_\alpha + x_{\rm c}}. \qquad (73)$$

Here $T_{\rm CMB}$ is the temperature of the surrounding bath of radio photons from the CMB and T_α is the color temperature of the Lyα radiation field at the Lyα frequency, where the color temperature is a measure of the shape of the photon distribution at a single frequency such that a blackbody of that temperature would give the same gradient in photon occupation number with frequency (see below for a more formal definition). Repeated scattering of Lyα photons from the gas brings T_α to equilibrium with the gas kinetic temperature $T_{\rm K}$. Finally, $x_{\rm c}$ and x_α are the coupling coefficients due to atomic collisions and scattering of Lyα photons, respectively.

The coupling coefficients compare the rate of spin flips induced by collisions or scattering Lyα photons to that induced by scattering of CMB photons. A large coupling coefficient indicates that process will dominate over the absorption of CMB photons and thereby determine

the equilibrium occupation of the hyperfine levels. This means that the spin temperature becomes strongly coupled to the gas temperature when $x_{\text{tot}} \equiv x_{\text{c}} + x_\alpha \gtrsim 1$ and relaxes to T_{CMB} when $x_{\text{tot}} \ll 1$.

In passing, we note that other atomic species show hyperfine transitions that may be useful in probing cosmology. Of particular interest are the 8.7 GHz hyperfine transition of $^3\text{He}^+$ (Bagla and Loeb, 2009; McQuinn and Switzer, 2009), which could provide a probe of helium reionization, and the 92 cm deuterium analogue of the 21-cm line (Sigurdson and Furlanetto, 2006). The details of the signal from these lines are much less developed and the reader is referred to the above cited works for additional information.

5.1.2 Collisional Coupling

Before stars form, the only mechanism for coupling the spin and gas temperatures is via spin flip inducing collisions between hydrogen atoms and other particles. The collisional coupling x_{c}^i for a particle species i is (Field, 1958; Furlanetto et al., 2006b)

$$x_{\text{c}}^i \equiv \frac{C_{10}^i}{A_{10}} \frac{T_\star}{T_{\text{CMB}}} = \frac{n_i \kappa_{10}^{i\text{H}}}{A_{10}} \frac{T_\star}{T_{\text{CMB}}}, \qquad (74)$$

where C_{10}^i is the collisional de-excitation rate from the singlet to the triplet level due to collisions with species i, A_{10} is the Einstein A coefficient for spontaneous de-excitation from the triplet to the singlet level, and $\kappa_{10}^{i\text{H}}$ is the species-specific rate coefficient for spin de-excitation from collisions. The total collisional coupling coefficient is a sum of the different processes: (i) scattering between two hydrogen atoms, (ii) between an electron and a hydrogen atom, and (iii) between a proton and a hydrogen atom. The collisional rates for each of these individual processes require quantum mechanical calculation. Values for scattering between H atoms κ_{10}^{HH} have been tabulated as a function of T_{K} (Allison and Dalgarno, 1969; Zygelman, 2005), the scattering rate coefficient between electrons and hydrogen atoms κ_{10}^{eH} was considered in Furlanetto and Furlanetto (2007a), and the scattering rate coefficient between protons and hydrogen atoms κ_{10}^{pH} was considered in Furlanetto and Furlanetto (2007b). Useful fitting functions exist for both the HH scattering rate coefficient (Kuhlen et al., 2006) and the eH scattering rate coefficient (Liszt, 2001). One could also consider scattering from helium and trace species, for example, lithium, but these are unlikely to be significant during reionization. Neutral helium has a closed electron shell and so cannot drive spin flips during collisions, except in the rare situation

that it has first been placed in an excited state (Hirata and Sigurdson, 2007). Partially ionized He$^+$ could cause spin flips, but is unlikely to be abundant until well into reionization when Lyα scattering is likely to dominate spin coupling.

The above calculations make use of the assumption that the collisional cross sections are independent of velocity; the actual velocity dependence leads to a nonthermal distribution for the hyperfine occupation (Hirata and Sigurdson, 2007). During the cosmic Dark Ages, when collisions are the dominant coupling channel, this effect can lead to a suppression of the 21-cm signal at the level of 5%. This is an important correction if the 21-cm signal from the Dark Ages is to be used to measure cosmological parameters precisely.

5.1.3 Wouthuysen–Field Effect (Photon Coupling)

As the Universe expands, the intergalactic medium (IGM) become less dense and collisional coupling becomes less effective. For $z \lesssim 30$, which is likely to be observationally probed in the near future, we expect collisions to play little role in setting the spin temperature. However, once star formation begins, resonant scattering of Lyα photons provides a second channel for coupling the spin temperature to the gas temperature. This process is known as the Wouthuysen–Field effect (Field, 1958; Wouthuysen, 1952) and is illustrated in Fig. 11, which shows the hyperfine structure of the hydrogen 1S and 2P levels.
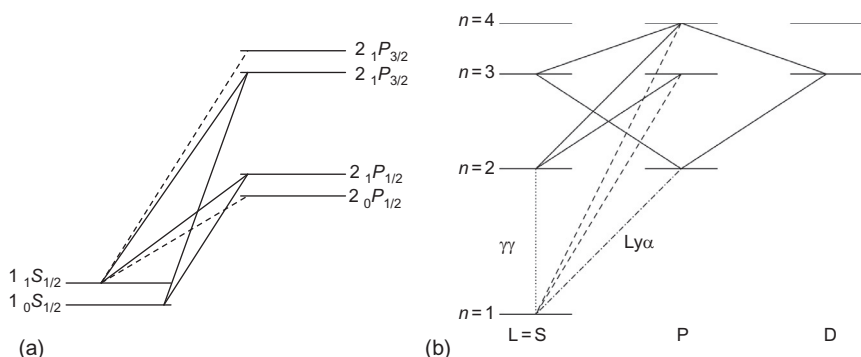
Fig. 11. (a) Hyperfine structure of the hydrogen atom and the transitions relevant for the Wouthuysen–Field effect (Pritchard and Furlanetto, 2006). The solid line transitions allow spin flips, while the dashed transitions are allowed but do not contribute to spin flips. (b) Illustration of how atomic cascades convert higher-energy Lyman photons into either Lyα photons or the two photon ($\gamma\gamma$) decay from the 2S level.

Suppose that hydrogen is initially in the hyperfine singlet level. Absorption of a Lyα photon will excite the atom into either of the $2\,^1P_{1/2}$ or $2\,^1P_{3/2}$ hyperfine levels. The electric dipole selection rules are $\Delta F = 0, 1$ with no $F = 0 \to 0$ transitions, making the other two hyperfine levels inaccessible. When the atom re-emits a Lyα photon, it can relax to the hyperfine triplet of the ground level. A similar mechanism is at work for photoexcitation out of the triplet level relaxing to the singlet level. As a result, resonant scattering of Lyα photons can produce a spin flip and change the relative occupation number of the two levels.

The strength of the Lyα coupling is determined by the scattering rate of Lyα photons and their ability to drive spin flips. This can be expressed as (Pritchard and Furlanetto, 2006)

$$x_\alpha = \frac{16\pi^2 T_\star e^2 f_\alpha^{\text{osc}}}{27 A_{10} T_{\text{CMB}} m_e c} S_\alpha J_\alpha, \qquad (75)$$

where e is the elementary charge, f_α^{osc} the Lyα oscillator strength, m_e the electron mass, and J_α the specific (number) flux of Lyα photons. Here we have introduced S_α as a correction factor of order unity that describes the detailed photon distribution in the neighborhood of the Lyα resonance relative to the flux J_α.

We can use Eq. (75) and the evolution of T_{CMB} with z to define a critical flux required for Lyα coupling to affect the spin temperature through the requirement $x_\alpha = S_\alpha$ giving $J_\alpha^C \equiv 1.165 \times 10^{10}[(1+z)/20]$ $\text{cm}^{-2}\,\text{s}^{-1}\,\text{Hz}^{-1}\,\text{sr}^{-1}$. This critical flux can also be expressed in terms of the number of Lyα photons per hydrogen nucleus $J_\alpha^C/n_{\text{Hn}} = 0.0767[(1+z)/20]^{-2}$, where $n_{\text{Hn}} \propto (1+z)^3$ is the number density of hydrogen nuclei. In practice, this condition is easy to satisfy once star formation begins.

Scattering of Lyα photons changes the spin temperature to a new temperature scale that depends upon the radiation field, that is, the color temperature. The color temperature in the neighborhood of the Lyα line is best defined via the shape of the radiation field as a function of frequency by (Rybicki, 2006)

$$\frac{2\pi\hbar}{k_B T_\alpha} = -\left[\frac{\text{d}\log n_\nu}{\text{d}\nu}\right]_{\nu=\nu_\alpha}, \qquad (76)$$

where $n_\nu = c^2 J_\nu/2\nu^2$ is the photon occupation number and ν_α the Lyα frequency. Note that here the color temperature is defined assuming an isotropic radiation field and as a results J_ν is the mean number flux versus ν, independent of solid angle.

Typically, $T_\alpha \approx T_{\mathrm{K}}$, because in most cases of interest the optical depth to Lyα scattering is very large leading to a large number of scatterings of Lyα photons that bring the radiation field and the gas into local equilibrium for frequencies near the line center (Field, 1959). At the level of the microphysics, this relation occurs through the process of scattering Lyα photons in the neighborhood of the Lyα resonance, which leads to a distinct feature in the frequency distribution of photons. Without going into the details, one can understand the formation of this feature in terms of the "flow" of photons in frequency. Redshifting with the cosmic expansion leads to a flow of photons from high to low frequency at a fixed rate. As photons flow into the Lyα resonance, they may scatter to larger or smaller frequencies. Since the cross section is symmetric, one would expect the net flow rate to be preserved. However, each time a Lyα photon scatters from a hydrogen atom, due to atomic recoil the photon will lose a fraction of its energy $2\pi\hbar\nu/m_{\mathrm{p}}c^2$, where m_{p} is the proton mass. This loss of energy increases the flow to lower energy and leads to a deficit of photons at and around the line center. Scattering redistributes photons leading to an asymmetry about the line, so that the deficit is more pronounced blue-ward of line center (Chen and Miralda-Escudé, 2004). This asymmetry is exactly that required to bring the distribution into local thermal equilibrium and so set $T_\alpha \approx T_{\mathrm{K}}$. To facilitate connection of the 21-cm signal to astrophysics, we would like to refer to the mean background Lyα flux J_α and therefore sweep this detailed physics of scattering and recoil into the correction factor S_α. Since there is actually a deficit of Lyα photons at line center, the scattering rate that drives the Wouthuysen–Field effect will be decreased, as the probability of scattering leading to a spin flip falls off away from line center. The net effect of this atomic physics is that the coupling will be slightly suppressed giving $S_\alpha \lesssim 1$.

At low values of T_{K}, recoils have more of an effect as the energy imparted to the atom by a single scattering-and-recoil event represents a larger fraction of the overall particle energy than for high temperatures. This means that the deficit in the Lyα flux at line center is more pronounced at low temperatures and so the Wouthuysen–Field effect is less effective. In contrast, if some mechanism has heated the IGM to temperatures $T_{\mathrm{K}} \gtrsim 10\,\mathrm{K}$, then the effect of recoils on the Lyα distribution is negligible and $S_\alpha \approx 1$ (Chen and Miralda-Escudé, 2004; Chuzhoy and Shapiro, 2007; Furlanetto and Pritchard, 2006; Hirata, 2006).

The above discussion has neglected processes whereby the distribution of photons is changed by spin exchanges. Including this complicates the

determination of T_S and T_α considerably since they must then be iterated to find a self-consistent solution for the level and photon populations (Hirata, 2006). The effect of spin flips on the photon distribution is $\lesssim 10\%$, which is important but typically less than the uncertainty in our knowledge of the sources themselves.

In the astrophysical context, Lyα photons can be produced by two mechanisms. Photons emitted at frequencies below Lyβ will redshift directly into the Lyα resonance. Photons emitted at frequencies higher than Lyβ will redshift until they reach a Lyman series resonance and excite a hydrogen atom. The excited atom will then relax via an atomic cascade, which can produce Lyα photons. These atomic cascades are illustrated in Fig. 11, where the probability of converting a higher-energy Lyman photon into a Lyα photon is set by consideration of the Einstein A coefficients for electric dipole transitions and can be found in tabular form in Hirata (2006) and Pritchard and Furlanetto (2006). For large n, approximately 30% conversion is typical. Since these photon arise from atomic cascades, they are injected into the Lyα line where they immediately begin scattering. The combination of scattering and redshifting makes the frequency distribution of these injected photons highly asymmetric. In the absence of scatterings, there would be a step function distribution with no photons at frequencies higher than the Lyα frequency and redshifted photons populating lower frequencies. This one-sided distribution modifies the details of their contribution to the Wouthuysen–Field coupling (Chen and Miralda-Escudé, 2004).

Though the details are subtle, the two effects of Lyα scattering is to (1) couple the hydrogen spin temperature to the Lyα color temperature and (2) drive the Lyα color temperature to the gas temperature. The net effect is that Lyα scattering couples spin and gas temperatures together.

5.2 Global 21-cm Signature

The 21-cm signal can be probed by two different sorts of experiment. Single radio dipoles can measure the total power of the 21-cm signal and thereby track the evolution of the sky-averaged brightness (bottom panel in Fig. 10) while radio interferometers can map the fluctuations in 21-cm brightness (top panel in Fig. 10). We first examine the cosmological evolution of the mean 21-cm signal and only later turn to the fluctuations. The 21-cm brightness temperature can be expressed as

a function of four variables $T_b = T_b(T_K, x_{H\,II}, J_\alpha, n_{Hn})$. The number density of neutral hydrogen atoms is then given by $n_{H\,I} = (1 - x_{H\,II})n_{Hn}$, since the abundance of molecular hydrogen in the gas is insignificant. As these quantities evolve, they lead to several qualitatively different phases, which can be seen in Fig. 10. We can outline the sequence in terms of the redshifts of star formation $z_\star$, saturated Lyα coupling z_α, strong X-ray heating z_h, and reionization z_r. These serve to define the following phases:

1. $z \gtrsim 200$ ($T_S = T_K = T_{CMB}$; $x_c \gg 1$, $x_\alpha = 0$; $x_{H\,I} = 1$): After recombination, Compton scattering maintains thermal coupling of the gas to the CMB, so that there is no 21-cm signal.

2. $40 \lesssim z \lesssim 200$ ($T_S = T_K < T_{CMB}$; $x_c \gg 1$, $x_\alpha = 0$; $x_{H\,I} = 1$): The gas thermally decouples from the CMB and cools adiabatically with the expansion of the Universe. During this phase, the gas temperature cools adiabatically as $T_K \propto (1 + z)^2$, faster than the CMB, $T_{CMB} \propto (1 + z)$. Collisions couple the spin and gas temperatures leading to an early absorption signal. Density inhomogeneities produce brightness fluctuations, potentially allowing the initial conditions to be probed (Hirata and Sigurdson, 2007; Loeb and Zaldarriaga, 2004).

3. $z_\star \lesssim z \lesssim 40$ ($T_S = T_{CMB}$, $T_K \ll T_{CMB}$; $x_c \sim 0$, $x_\alpha = 0$; $x_{H\,I} = 1$): The decreasing gas density makes collisional coupling ineffective and the spin temperature relaxes to the CMB, so there is no detectable 21-cm signal.

4. $z_\alpha \lesssim z \lesssim z_\star$ ($T_S = T_K \ll T_{CMB}$; $x_c \sim 0$, $x_\alpha \sim 1$; $x_{H\,I} = 1$): Once the first galaxies form, they produce Lyα photons, which again couple the spin and gas temperatures. This leads to a strong absorption signal since the gas has continued to cool adiabatically. Brightness fluctuations are dominated by spatial variation in the Lyα flux (Barkana and Loeb, 2005b; Chen and Miralda-Escudé, 2008; Pritchard and Furlanetto, 2006).

5. $z_h \lesssim z \lesssim z_\alpha$ ($T_S = T_K \sim T_{CMB}$; $x_c \sim 0$, $x_\alpha \gg 1$; $x_{H\,I} = 1$): Ultimately, Lyα coupling saturates so that fluctuations in the Lyα flux no longer affect the 21-cm signal. The first stars die leaving compact remnants, whose X-ray emission begins to heat the gas. The resulting gas temperature fluctuations cause brightness fluctuations. A patchwork of different temperatures means some regions will be seen in absorption and others in emission.

6. $z_r \lesssim z \lesssim z_h$ ($T_S = T_K \gg T_{CMB}$; $x_c \sim 0$, $x_\alpha \gg 1$; $x_{H\,I} \sim 0.5$): After the gas has everywhere been heated above the CMB, the 21-cm signal

is seen solely in emission. Ionized bubbles begin to grow around groups of galaxies and are visible as patches of no 21-cm signal.

7. $z \lesssim z_r$ ($T_S = T_K \gg T_{CMB}$; $x_c \sim 0$, $x_\alpha \gg 1$; $x_{H\,I} \sim 0.03$): After reionization, any remaining 21-cm signal originates primarily from collapsed islands of neutral hydrogen (damped Lyα systems).

This basic story is built upon our understanding of galaxy formation, but is subject to considerable uncertainty. These epochs are unlikely to be sharply defined, but are representative of the physics involved as we discuss below.

5.2.1 Cosmic Dark Ages and Exotic Heating ($z \gtrsim 40$)

During the early stages of the 21-cm signal, the key elements of physics are well understood. Recombination sets the initial conditions for the gas and CMB temperature, which then evolve according to the well-understood adiabatic expansion of the Universe and Compton scattering of CMB photons from the small residual electron fraction. Hence, the 21-cm signal before star formation is well understood in the absence of exotic physics. This simplicity makes it an interesting regime to look for nonstandard physics. So long as collisional coupling is saturated, the global 21-cm signal plays the role of a thermometer for the IGM gas temperature. Many models of physics beyond the standard model make concrete predictions for exotic energy injection and so heating of the IGM. Some examples include dark matter annihilation (Belikov and Hooper, 2009; Chen and Kamionkowski, 2004; Furlanetto et al., 2006c; Slatyer et al., 2009; Valdés et al., 2007), decaying dark matter (Furlanetto et al., 2006c; Valdés et al., 2007), excited dark matter (Finkbeiner et al., 2008), evaporating primordial black holes (Mack and Wesley, 2008; Ricotti et al., 2008), and cosmic strings wakes (Brandenberger et al., 2010). Incorporating the heating effect of exotic physics will require a knowledge of the energy spectrum of photons produced by any of these various sources, which must then be carefully modeled to determine how much of the radiative energy is ultimately deposited into the IGM.

5.2.2 Lyman-α Coupling ($z_\alpha \lesssim z \lesssim z_\star$)

Once the first galaxies begin to form (probably around $z \sim 30$), their radiation becomes important for the 21-cm signal. Photons emitted by stars, between Lyα and the Lyman limit, will redshift until they enter a Lyman series resonance. Subsequently, they may generate Lyα photons via atomic cascades (Hirata, 2006; Pritchard and Furlanetto, 2006). It is

currently unclear what the first stars looked like, and there is a possibility that either Population II or Population III stars dominated the light of the first galaxies.

To a first approximation, the 21-cm signal should depend primarily on the total number of Lyα photons emitted, which is key for the overall strength of the Wouthuysen–Field effect. Only with precision measurements of the 21-cm power spectrum might we say something about the details of the source spectrum, which will modify slightly the spatial distribution of Lyα photons (Chuzhoy et al., 2006; Pritchard and Furlanetto, 2007). For example, model spectra of Population II stars indicate that about 6590 Lyα photons are produced for every baryon processed in a star (Barkana and Loeb, 2005b; Leitherer et al., 1999), while very massive Population III stars are predicted to produce around 3030 Lyα photons (Bromm et al., 2001). This difference is small compared to the order of magnitude uncertainty in the star formation rate at early times. As a result, we expect the Lyα emissivity from stars to be relatively insensitive to the stellar type and to initially provide information about the overall star formation rate.

A second source of Lyα photons comes from photoionization of H I or He I by X-rays. Energy from the primary photoelectron will be partitioned between secondary ionization, heating, and excitation of hydrogen atoms. As these collisionally excited electrons relax via radiative emission, some Lyα photons will be produced (Chen and Miralda-Escudé, 2008; Chuzhoy et al., 2006). The fraction of energy that goes into producing Lyα photons can be calculated by Monte-Carlo simulation of an X-ray scattering in the IGM (Furlanetto and Stoever, 2010; Shull and van Steenberg, 1985; Valdés and Ferrara, 2008). The final Lyα flux produced by X-ray excitation may be found by balancing the rate at which Lyα photons are produced by cascades with the rate at which photons redshift out of the Lyα resonance (Chen and Miralda-Escudé, 2008).

The relative importance of Lyα photons from X-rays or directly produced by stars is highly dependent upon the nature of the sources that existed at high redshifts. Furthermore, it can vary significantly from place to place. In general, X-rays with their long mean free path seem likely to dominate the Lyα flux far from sources while the contribution from stellar sources dominates closer in (Chen and Miralda-Escudé, 2008).

5.2.3 Gas Heating ($z_h \lesssim z \lesssim z_\alpha$)

Both collisions and Lyα ultimately couple the spin and gas temperatures. At high redshifts, the dominant source of heating is Compton heating

of the gas arising from the scattering of CMB photons from the small residual free electron fraction. Since these free electrons scatter readily from the surrounding baryons, this transfers energy from the CMB to the gas. Ultimately, at redshift $z \sim 200$, the expansion of the Universe reduces the number density of CMB photons and the energy per photon to the point that Compton heating is no longer efficient. Thereafter, the gas cools adiabatically, becoming colder than the CMB.

Once galaxy formation begins, new heating mechanisms appear. Shocks can occur around collapsed objects leading to heating of the gas in localized regions (Furlanetto and Loeb, 2004). More importantly, galaxies can heat the gas by emission of photons between Lyα and the Lyman limit or by X-rays. The scattering of Lyα photons by hydrogen atoms leads to a slight recoil of the nuclei that saps energy from the photons, thereby heating the gas (Madau et al., 1997). Detailed consideration of the atomic physics of this process shows it to be relatively inefficient (Chen and Miralda-Escudé, 2004; Chuzhoy and Shapiro, 2007; Furlanetto and Pritchard, 2006). It is natural to compare the heating rate of the gas due to scattering by Lyα photons with the Lyα flux required to couple the spin and gas temperatures. For the critical Lyα flux required to set $x_\alpha \approx 1$, scattering of Lyα photons will not heat the gas significantly (Chen and Miralda-Escudé, 2004; Chuzhoy and Shapiro, 2007; Furlanetto and Pritchard, 2006). This is vital for the 21-cm signal, since it allows for a period of strong 21-cm absorption when Lyα photons couple the spin and gas temperatures before the gas is heated above the CMB temperature. In the absence of other heating mechanisms, Lyα heating could be important at late times when the Lyα flux becomes large so that $x_\alpha \gg 1$.

The most important source of energy injection into the IGM is likely via X-ray heating of the gas (Chen and Miralda-Escudé, 2004; Pritchard and Furlanetto, 2007; Venkatesan et al., 2001; Zaroubi et al., 2007). For sensible source populations, Lyα heating is mostly negligible compared to X-ray heating (Ciardi et al., 2010; Furlanetto and Pritchard, 2006). Energetic X-rays have a long mean free path and are able to heat gas far from the source. X-rays heat the gas primarily through photoionization of H I and He I, which produces energetic photoelectrons that deposit their energy in the gas through heating, secondary ionizations, and atomic excitation. As mentioned earlier, the relevant division of the X-ray energy depends on both the X-ray energy E and the free electron fraction x_e and can be calculated by Monte-Carlo methods. Once x_e of a few percent has been reached, most of the X-ray energy is deposited as heat.

X-rays can be produced by a variety of sources, with three main candidates at high redshifts being identified as starburst galaxies where the high densities and star formation rates leads to a large population of X-ray binaries, supernova remnants, and miniquasars (Furlanetto, 2006; Glover and Brand, 2003; Oh, 2001). The total X-ray luminosity at high redshift is constrained by observations of the present-day soft X-ray background, which rules out complete reionization by X-rays but allows considerable latitude for heating (Dijkstra et al., 2004a).

5.2.4 Growth of H II Regions ($z_r \lesssim z \lesssim z_h$)

The Universe is believed to have been ionized by UV photons with energies $E \gtrsim 13.6$ eV. Such photons have short mean free paths in a neutral IGM, and we expect galaxies producing UV photons to be surrounded by an ionized bubble with sharp boundaries. Ionization by X-rays is believed to be a smaller contribution; but X-rays have a longer mean free path in the IGM and could soften these bubble boundaries (Geil and Wyithe, 2009) and ionize gas beyond these bubbles. To a good approximation, the IGM can be treated as a two-phase medium with hot, ionized bubbles surrounded by cooler, mostly neutral IGM. These ionized bubbles show up as "holes" in the surrounding 21-cm emission. We describe the filling fraction of ionized bubbles by x_i and the free electron fraction of the partially ionized IGM outside these bubbles by x_e. In this two-phase IGM model, the average number density of neutral hydrogen in the Universe is $n_{H I} = (1 - x_e)(1 - x_i)n_{Hn}$. The factor of $1 - x_e$ accounts for the partial ionization by X-rays of the IGM outside of the fully ionized bubbles, but in most models x_e remains small.

During the early stages of reionization, ionized bubbles surround individual galaxies. These rapidly grow to surround groups of nearby galaxies. These larger bubbles grow as more galaxies form until eventually they percolate and the entire Universe is ionized (except for very dense self-shielding regions). As a result, the overall pattern of ionized regions is driven by the clustering statistics of galaxies.

The growth of ionized H II regions is governed by the interplay between ionization and recombination, both of which contain considerable astrophysical uncertainties. The sources of ionizing photons in the early Universe are believed to have been primarily galaxies. However, the properties of these galaxies are currently poorly constrained, with recent observations with the Hubble Space Telescope providing some of the best available constraints on early galaxy formation. Faint galaxies are identified as being

at high redshift using a "Lyman break technique." The emitted light from these galaxies displays a strong drop in amplitude for wavelengths below the rest frame Lyα wavelength of 1216 Å, as a result of the absorption of star light by neutral hydrogen gas internal to the galaxy. Detection of a galaxy in different wavelength filters measures the observed frequency of the break and allows the redshift of the galaxy to be estimated. So far, galaxies at redshifts up to $z \sim 9$ have been found providing information on the sources of reionization. Unfortunately, there are considerable limitations on the existing surveys owing to their small sky coverage, which makes it unclear whether those galaxies seen are properly representative. Even more problematic for our purposes is that the optical frequencies at which the galaxies are seen do not correspond to the UV photons that ionize the IGM. Our limited understanding of the mass distribution of the emitting stars introduces an uncertainty in the number of ionizing photons emitted per baryon inside stars, N_{ion}. There is also considerable uncertainty in the fraction of ionizing photons f_{esc} that escape the host galaxy to ionize the IGM.

The recombination rate is primarily important at late times once a significant fraction of the volume has been ionized. At this stage, dense clumps within an ionized bubble can act as sinks of ionizing photons slowing or even stalling further expansion of the bubble. The degree to which gas resides in these dense clumps is an important uncertainty in modeling reionization. Hydrodynamic effects, such as the evaporation of gas from a halo as a result of photoionization heating (Pawlik et al., 2009), can significantly modify the clumping and impact of recombinations.

5.2.5 Astrophysical Sources and Histories

Calculating the 21-cm signal has two key parts—understanding the population of sources and understanding how their radiation affects the surrounding IGM. Although we have a reasonable understanding of the physical processes involved, our knowledge of the properties of the early sources of radiation is highly uncertain. We have three radiation backgrounds to account for: ionizing UV, X-ray, and Lyman series photons. For each of these radiation fields, we must specify parameters to describe: the ionization efficiency ζ, the X-ray emissivity f_X, and the Lyα emissivity f_α. Each of these parameters determines the effect of a given star formation history, which must itself be specified.

Figure 12 shows one example of the global 21-cm signal and the associated evolution in the neutral fraction and the gas kinetic and spin
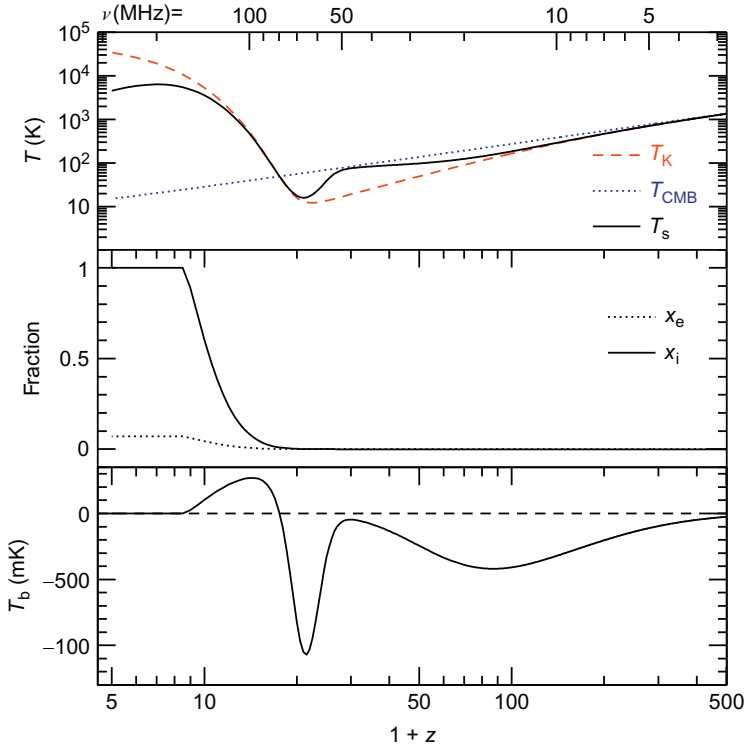
Fig. 12. *Top panel:* Evolution of the CMB temperature T_{CMB} (dotted curve), gas kinetic temperature T_K (dashed curve), and spin temperature T_S (solid curve). *Middle panel:* Evolution of the filling fraction of ionized regions, x_i (solid curve), and the ionized fraction outside these regions due to diffuse X-rays, x_e (dotted curve). *Bottom panel:* Evolution of mean 21-cm brightness temperature T_b (Pritchard and Loeb, 2008).

temperatures. As seen in the top panel, at high redshift, $10 \lesssim z \lesssim 200$, the gas temperature cools faster than the CMB (since the residual fraction of free electrons is insufficient to couple the two temperatures). At the same time, collisional coupling is effective at coupling spin and gas temperatures leading to the absorption trough seen on the right of the bottom panel. The details of this trough are fixed by cosmology and therefore may be predicted relatively robustly. The minima of this trough at $z \sim 90$ correspond to the point at which collisional coupling starts to become relatively ineffective.

Once star formation begins, the spin and gas temperatures again become tightly coupled by Lyα scattering leading to a second, potentially deeper, absorption trough (seen in the bottom panel at $z \sim 20$). The minimum of this trough corresponds to the point when X-ray heating switches on, heating the gas above the CMB temperature, and leading to an emission

signal. There then begins a phase where $T_S \gg T_{CMB}$, so that $(T_S - T_{CMB})/T_S \approx 1$ and the evolution of the spin temperature no longer determines the brightness temperature (cf., Eq. 72). Finally, the signal dies away as ionization of neutral hydrogen is ionized (compare middle and bottom panels).

The ordering of these events is determined primarily by the energetics of the processes involved and by the basic properties of the spectra expected for Population II and Population III stars. For example, ionization requires at least one ionizing photon with energy $E \geq 13.6$ eV per baryon while depositing only ~10% of that energy per baryon would heat the gas to $T_K \gtrsim 10^4$ K. However, the details of the shape of the curve after star formation begins are highly uncertain, but the basic structure of one emission feature and two absorption troughs is likely to be robust. By determining the positions of the various turning points in the signal, one could hope to constrain the underlying astrophysics and learn about the first stars and galaxies.

5.3 21-cm Tomography

Integrating the 21-cm signal over the full sky gives the global signal, which can be viewed as a zeroth order approximation to the full 21-cm signal, as it is averaged over large angular scales. The full 3D signal will be highly inhomogeneous as a result of the spatial variation in the different radiation fields and properties of the IGM. In this section, we consider the physics underlying 21-cm brightness fluctuations in 3D. Figure 13 shows four redshift slices from a numerical simulation of the 21-cm signal, which may be viewed like still frames taken from a movie. These slices indicate the different regimes that occur as the dominant source of fluctuations change with time.

5.3.1 Fluctuations in the Spin Temperature

In the early phases of the 21-cm signal when the IGM is fully neutral, brightness fluctuations arise from variations in the spin temperature of the gas. Fluctuations in the Lyα coupling (Barkana and Loeb, 2005b; Pritchard and Furlanetto, 2006) are driven by spatial variation in the Lyα flux as a result of the clustering of star-forming galaxies. Light emitted from galaxies at frequencies between Lyα and the Lyman limit has the possibility of contributing to the Lyα flux. These UV photons will redshift as they travel until ultimately they become resonant with one of the Lyman series lines of hydrogen and begin to scatter. Photons scattering in high Lyman series
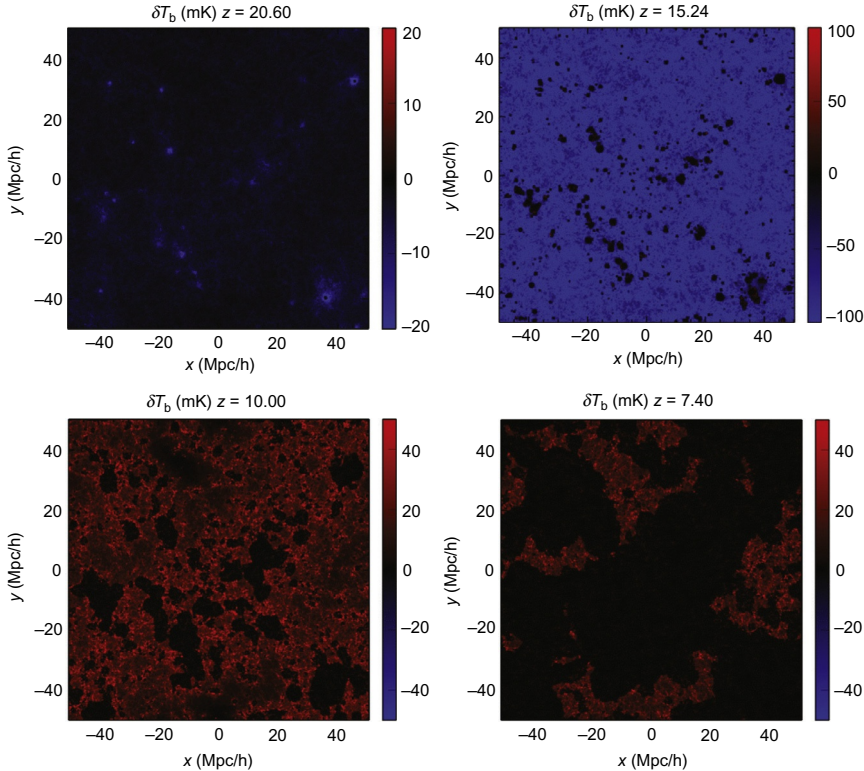
Fig. 13. Redshift slices illustrating 21-cm fluctuations at different redshifts (Santos et al., 2008). *Top left:* First star forming galaxies produce Lyα halos seen as regions as strong 21-cm absorption (blue (light gray in the print version)). *Top right:* Continuing Lyα emission leads to a strong 21-cm absorption signal from the majority of the IGM. *Bottom left:* X-ray heating raises the gas temperature so that the IGM is seen in 21-cm emission (red (dark gray in the print version)). *Bottom right:* Growing ionized regions (black) lead to holes in the 21-cm absorption.

lines may rapidly be converted into Lyα photons via atomic cascades as described earlier. The first galaxies were rare and, as a result, we expect small groupings of galaxies to form isolated "Lyman–alpha halos"—islands of gas where Lyα coupling is strong surrounded by uncoupled gas. This can be seen in the top left panel of Fig. 13, where these islands are seen in absorption against the CMB.

At redshifts before reionization, the Universe is filled with neutral H leading to an optical depth for scattering of Lyα photons that is very large, with $\tau \gtrsim 10^5$. While this is reduced for higher series transitions, the Universe is optically thick for all but the highest Lyman series transitions. This modifies the naive expectation that a UV photon emitted above the

Lyα frequency will redshift until it reaches the Lyα frequency and then begin scattering from hydrogen atoms. This naive picture essentially assumes a delta function line profile, but the high optical depth makes scattering in the wings of the line important. A photon redshifting as it travels through space is likely to scatter in the wings of the Lyα line long before it reaches the line center. The high optical depth also implies a short mean free path for these photons, so that they will not move far from the point where they first scatter and subsequent frequency evolution will be driven by scattering not redshifting (Chuzhoy and Zheng, 2007; Naoz and Barkana, 2008; Semelin et al., 2007).

A key consequence is that a UV photon emitted above the Lyα frequency will travel a shorter distance through the IGM before scattering from a hydrogen atom than predicted by a naive calculation that expected them to scatter only at line center. This effect makes the Lyα halos smaller and more pronounced and so increases the variance in the Lyα flux on small scales.

5.3.2 Gas Temperature

Ultimately, Lyα halos will percolate so that all of the IGM is illuminated with a sufficient Lyα flux to allow the Wouthuysen–Field effect to operate. As a result, we expect T_S to be well coupled to T_K throughout the IGM at late times ($z \lesssim 20$ in Fig. 12). It follows from this that inhomogeneities in the gas temperature will translate into spin temperature fluctuations. If X-ray heating is the dominant driver of the gas temperature, then the clustering of X-ray sources will lead to inhomogeneous heating (Pritchard and Furlanetto, 2007). In the case of heating by extremely rare quasars, Poisson fluctuations may also become important (Alvarez et al., 2010). The top right panel of Fig. 13 shows the beginning of this phase of temperature fluctuations. In this slice, Lyα photons have everywhere coupled the spin and gas temperatures leading to a strong absorption signal throughout the box. However, scattered regions are beginning to be heated to around the CMB temperature making them look dark against the background absorption. Ultimately, the gas is heated throughout the volume and passes into emission, which is shown in the bottom left panel of Fig. 13.

Insight into X-ray heating can be gained by looking at the results of 1D numerical simulations of X-ray radiative transfer (Venkatesan et al., 2001; Zaroubi et al., 2007). The optical depths for X-ray absorption (which leads to photoionization of electrons and the deposition of energy as further ionization and heating) are strongly energy dependent with a cross section $\sigma \propto E^{-3}$. Soft X-rays have a short mean free path and are absorbed close

to the source; harder X-rays will travel further, while X-rays with energies $E \gtrsim 2\,\mathrm{keV}$ can have mean free paths comparable with the size of the Universe and so may reach us today without being absorbed. Observations of the present-day unresolved soft X-ray background place constraints on early populations of X-ray sources via their contribution from redshifted hard X-rays (Dijkstra et al., 2004a).

In the local Universe, shocks around large collapsed structures are known to be an important mechanism for IGM heating. Shocks heat the gas directly by converting bulk motion into thermal energy. They can also be responsible for accelerating charged particles (if magnetic fields are present in the shock), which can lead to radiative emission of X-rays and so further heating. Shocks have been discussed both analytically (Furlanetto and Loeb, 2004) and observed in simulations (Kuhlen et al., 2006; Shapiro et al., 2006). These models show that, in the absence of X-ray heating, the IGM can be significantly heated by large scale shocks at redshifts $z \lesssim 20$.

5.3.3 Ionization Fluctuations

Once the gas has been heated far above the CMB temperature, the spin temperature is no longer important in determining the 21-cm signal. The key determining factor in the signal strength is the amount of neutral hydrogen. One of the major motivations for 21-cm observations is to map out fluctuations in the ionized fraction of the neutral hydrogen during reionization. These ionized bubbles can be seen in the bottom two panels of Fig. 13 as dark regions against the background emission from still neutral gas.

Reionization is a complicated process involving the balancing of ionizing photons originating in highly clustered collections of galaxies and recombinations in dense clumps of matter. It is perhaps surprising that remarkably robust models of the topology of reionization can be developed by simply counting the number of ionizing photons. This basic insight lies at the center of the analytic calculation of ionization fluctuations (Barkana and Loeb, 2004; Furlanetto et al., 2004). The distribution of bubbles sizes found from this analytic calculation has been shown to be a good match to numerical reionization simulations at the same neutral fraction (Zahn et al., 2007, 2011).

5.3.4 Density and Minihalos

In addition to the signal from the diffuse IGM seen in Fig. 13, significant 21-cm emission can arise from the densest regions of neutral hydrogen. These occur in those dense clumps that have achieved the critical density

for collapse, but that lack the mass for efficient cooling of the gas that would lead to star formation and so ionize the gas within the halo. This requirement is satisfied for halos of with $T_{\text{vir}} < 10^4$ K, provided that only atomic hydrogen is available for cooling or for halos with $T_{\text{vir}} \lesssim 300\,\text{K}$ if molecular hydrogen is present. These minihalos should be abundant in the early Universe, although at later times external ionizing radiation may cause them to evaporate. Furthermore, their formation may be prevented with moderate gas heating that raises the Jeans mass suppressing the collapse of these low mass objects. The high density in these regions implies that collisions can provide the main coupling mechanism, and due to the high temperature of the virialized gas these minihalos are bright in 21-cm emission (Furlanetto and Oh, 2006; Iliev et al., 2002, 2003; Shapiro et al., 2006).

5.3.5 Redshift Space Distortions

There is one final contribution to the details of the signal that is not readily visible by eye. Bulk flows in the gas—peculiar velocities—can have a significant effect on the 21-cm signal, since observations are made in frequency space while theory makes predictions most directly in real space. The conversion between these two coordinate systems is affected by the local velocity of the gas and leads to "redshift space distortions." In the limit that density perturbations are small, the effects of peculiar velocities are well understood and introduce an angular distortion of the observed 21-cm power spectrum, known as the "Kaiser effect" (Barkana and Loeb, 2005a; Bharadwaj and Ali, 2004; Wang and Hu, 2006). As the density field evolves, nonlinear corrections to the velocity field become important; the picture can change in ways that are not well understood. For example, large velocities in virialized structures leads to an apparent stretching of these overdensities along the line of sight (these features are often called "Fingers of God") and greatly complicates efforts to separate components via the angular structure of the 21-cm power spectrum (Mao et al., 2012; Mellema et al., 2006; Shaw and Lewis, 2008).

6. THE REIONIZATION OF INTERGALACTIC HYDROGEN

The hallmark event of the "cosmic dawn" is the reionization of the IGM: the transformation of the neutral hydrogen that forms during cosmological recombination into an ionized medium, most likely thanks to ultraviolet photons from stars, black holes, or a combination of the two. For

astrophysicists, this is a milestone event for several reasons. First, and most important, it is the most dramatic effect of the first generations of galaxies, triggering a global phase transformation in all the baryons in the Universe.[13] This shift in the global state from neutral to ionized only happens once: we know now that, during at least the past 12 billion years of the Universe, the gas has remained very highly ionized, and even if all of the luminous galaxies in the Universe switched off today, the gas is now so tenuous that it would not fully recombine. Reionization is, therefore, also the final phase transition in the history of the Universe.

Second, reionization has a number of concrete implications for galaxy formation. For example, it renders the IGM transparent to hydrogen-ionizing photons. Before reionization occurred, these photons were quickly absorbed by neutral hydrogen, except for the highest energy photons. Reionization also heats the IGM up to $T > 10^4$ K, dramatically increasing the thermal pressure of the gas—and hence the Jeans mass (see Section 4). This affects the gas by smoothing out density fluctuations in the IGM (Pawlik et al., 2009), evaporating small clumps of baryons (Shapiro et al., 2004), and suppressing accretion onto larger galaxies (Dijkstra et al., 2004b; Efstathiou, 1992).

Finally, because it is such a dramatic and widespread event, reionization is relatively easy to observe (at least by the standards of observations of the very high redshift Universe). We have already considered one important probe of reionization in Section 5, the 21-cm spin-flip background, but there are many others as well, including secondary effects on the CMB, absorption of light from luminous galaxies and quasars (primarily through the Lyα line of neutral hydrogen), and, indirectly, through the thermodynamic properties of the IGM at later times and even local structures within the Milky Way.

As such, over the past 15 years, a great deal of theoretical and observational effort has focused on the epoch of reionization. In this section, we will briefly summarize the physics and astrophysics of reionization, with an emphasis on the necessary atomic physics inputs. We refer the reader to Loeb and Furlanetto (2013) for a more extensive discussion.

---

[13] Helium most likely reaches its first ionization state along with hydrogen, though reaching the second requires much higher energy photons and must wait for the quasar era at $z \sim 3$. We will focus on the hydrogen era here, as it is of more fundamental importance to structure formation, but many of the same issues apply during the later era as well (e.g., Furlanetto and Oh, 2008; McQuinn et al., 2009).

6.1 Sources of Reionization: Stars

We begin by discussing some of the possible sources of reionization. In order to describe the reionization process from its most basic level, we need to know three things about these sources: (1) their locations, (2) their efficiency at converting their rest mass energy into ionizing photons, and (3) their spectra.

At the moment, little is known about the populations of luminous objects at $z > 7$ (Bouwens et al., 2010a,b; McLure et al., 2011; Willott et al., 2010). This epoch is when we believe reionization to be underway, but (barring exotic processes like dark matter decay or primordial black hole evaporation) the most likely agents are "conventional" astrophysical sources such as stars or quasars. In this subsection, we focus on the best-studied case, reionization by stellar sources.

The first characteristic is easy to address: following the arguments of the previous sections, densities only reach sufficiently large values to form luminous objects inside dark matter halos. We therefore associate each ionizing source with a dark matter halo. The halo must also be able to accrete gas that can then shed its thermal energy (large following virialization) and collapse to the much higher densities characteristic of star formation. The latter requires the gas undergo efficient radiative cooling. In primordial gas, this requires either efficient H_2 formation (in low mass halos) or that the virialization shock heat the gas to $T > 10^4$ K, where line transitions of atomic hydrogen can be excited (Barkana and Loeb, 2001). The latter then allows the gas to radiatively shed its thermal energy and to cool to low temperatures where star formation could occur.

Atomic and molecular physics are crucial for this process, because it is radiative transitions of the primordial elements (primarily hydrogen) that are responsible for this cooling. Atomic cooling processes are well understood. But, important uncertainties remain in molecular cooling, which likely strongly affects the earliest stars. These are discussed above in Section 4.

Here we focus on scenarios in which halos with virial temperatures larger than 10^4 K host the sources that reionize the Universe. Due to the fragility of the low mass halos in which Population III stars form, the conventional wisdom is that they cannot form enough stars to complete the reionization process. Fortunately, most of our conclusions from large halos are general enough to apply to other source populations.

The first factor affecting the number of stars able to form in the Universe is thus the mass available within this population of star-forming halos.

We define this as the collapse fraction f_{coll}, which is the fraction of all baryons inside halos. With a model for the number density of dark matter halos as a function of mass—which we have already seen in the Press–Schechter model of Eq. (46)—this collapse fraction can readily be computed:

$$f_{\text{coll}} = \text{erfc}\left[-\frac{\nu(z)}{\sqrt{2}}\right].\tag{77}$$

This result is adequate for our purposes here. It matches numerical simulations to within an order of magnitude or so for early times or for unusually large halo masses; it can easily be improved to provide a significantly better match (see Sheth and Tormen, 2002). The collapse fraction typically increases from a few tenths of a percent to a few percent over the course of reionization. In other words, only a small fraction of the mass of the Universe is actually bound into galaxies at these early times.

The second question—the efficiency with which these sources can ionize the Universe—is much harder to answer. We begin by discussing the case of ionizing photons from stars. The overall efficiency can be broken into several pieces.

1. *What is the efficiency with which galaxies can form stars?* Knowing that gas is inside a dark matter halo is not enough to determine whether it can actually form stars. Nearby galaxies have $< 10\%$ of their expected baryonic content inside of stars (Fukugita and Peebles, 2004). The remainder is still locked in the gas phase or in other (invisible) objects, or has been expelled through large-scale galaxy outflows (which are ubiquitous in rapidly star-forming galaxies). The processes through which stars form are still understood only crudely, and we do not yet have a robust model to predict the star formation efficiency, denoted $f_{\star}$, that is, the fraction of baryonic material a galaxy can transform into stars. This is especially true at high redshifts, as local observations do little to constrain how stars formed at these early times. For example, consider the case of very massive Population III stars where a halo is expected to form only a single very massive star ($M_{\star} \sim 10^2\,M_{\odot}$) that then disrupts its entire halo ($M_{\text{h}} > 10^6 M_{\odot}$) through ionizing radiation or a supernova. This then gives $f_{\star} \sim (\Omega_{\text{m}}/\Omega_{\text{b}})M_{\star}/M_{\text{h}} < 10^{-3}$.

2. *What is the efficiency with which stars generate ionizing photons?* The number of ionizing photons produced per baryon inside stars, N_{ion}, depends on the stellar masses and their metallicity (the fraction in the gas of elements heavier than helium, given below in terms of the solar metallicity $Z_{\odot}$). Convenient approximations are $N_{\text{ion}} \approx 4000$ for metallicity

$Z = 0.05\ Z_\odot$ Population II stars with a present-day mass distribution (Leitherer et al., 1999), and $N_{\rm ion} < 10^5$ for very massive Population III stars (Bromm et al., 2001; Schaerer, 2002). However, a number of other factors affect these estimates, such as mass transfer between binary stars, stellar rotation, and winds.

3. *What is the efficiency with which ionizing photons escape their galaxies?* Only a fraction of the UV photons manage to escape the interstellar medium (ISM) of their host galaxies into the IGM and thereby contribute to intergalactic reionization. This fraction, denoted $f_{\rm esc}$, is small in both nearby galaxies and those at moderate distances, with $f_{\rm esc} < 5\%$ (Boutsia et al., 2011; Gnedin et al., 2008; Iwata et al., 2009; Nestor et al., 2011; Shapley et al., 2006). Interestingly, $f_{\rm esc}$ shows a large variance between galaxies; most likely, ionizing photons are only able to escape along clear channels into the galactic ISM, perhaps blown by supernovae or powerful winds, which appear to be quite rare in the objects we can study. In principle, it could be considerably larger inside small, high redshift galaxies, whose ISM can easily be shredded by radiation pressure, winds, and supernovae, clearing out large escape paths (Whalen et al., 2004); but there is so far no good evidence either way at $z > 7$.

We can now naively estimate the requirements for hydrogen reionization. The minimal condition is that these stars have produced one ionizing photon (with $E > 13.6$ eV) per hydrogen atom in the Universe. Because $f_{\rm coll}$ is the fraction of all baryons inside galaxies (under the assumption that every dark matter halo above our cooling threshold contains a galaxy), this requirement may be written $f_{\rm coll}\, f_\star\, N_{\rm ion}\, f_{\rm esc}\, A_{\rm He}\, n_{\rm b} > n_{\rm H}$, where $n_{\rm b}$ is the baryon number density, $A_{\rm He} = 4/(4 - 3Y_{\rm p}) = 1.22$, and $Y_{\rm p}$ is the mass fraction of helium (this is a correction factor to convert the number of ionizing photons to the number of ionized hydrogen atoms assuming that helium is singly ionized as well). Taking the fiducial values above, we therefore need

$$f_{\rm coll} > \frac{0.025}{A_{\rm He}} \left(\frac{0.1}{f_\star} \frac{0.1}{f_{\rm esc}} \frac{4000}{N_{\rm ion}} \right). \tag{78}$$

The currently favored cosmological model reaches this threshold at $z \sim 10$, which suggests that reionization is likely to occur near that epoch.

Although the separate efficiency factors describe distinct physical effects, so far as IGM reionization is concerned they are essentially degenerate. For simplicity, we will therefore write the overall ionizing efficiency as $\zeta = A_{\rm He}\, f_\star\, f_{\rm esc}\, N_{\rm ion}$ below, so that the above condition may be written

$\zeta\,f_{\mathrm{coll}}\;>\;$ 1. This overall efficiency is clearly highly uncertain, but note that it only depends indirectly on atomic physics inputs (primarily through the cooling efficiency); most of the unknown factors require a better understanding of the astrophysical processes at play in forming high redshift galaxies and their internal structures.

We must also emphasize just how crude a view Eq. (78) provides of the sources themselves, which undoubtedly vary in these efficiency parameters not only across the population of all dark matter halos (and hence galaxies) but also evolve over time, causing substantial variations in the parameters of even a single galaxy. Predictions of the ionizing process require a sophisticated understanding of galaxy evolution throughout the cosmic dawn, which lies well beyond our powers at present.

Moreover, this is a minimal estimate, as it ignores the possibility of recombinations in the IGM, which increase the required number of ionizing photons (since some atoms must be ionized multiple times). It is easy to see that this is likely to be of at least moderate importance during the reionization era by taking the recombination time for a single hydrogen ion, $t_{\mathrm{rec}} = (\alpha n_{\mathrm{e}})^{-1}$, where α is the recombination rate coefficient. Comparing it to the expansion timescale $t_{\mathrm{H}} = H^{-1}(z)$, which is the time over which the cosmological scale factor increases by a factor of two, this yields (Furlanetto et al., 2006b)

$$\frac{t_{\mathrm{rec}}}{t_{\mathrm{H}}} \approx 0.8 \left(\frac{8}{1+z}\right)^{3/2}. \tag{79}$$

In fact, recombinations are more important than this, as inhomogeneities in the IGM increase the overall recombination rate (which is $\propto n_{\mathrm{H}} n_{\mathrm{e}}$), though this also implies most of those recombinations occur in locally overdense environments.

We could simply assume that such recombinations occur uniformly across space; in that case, if N_{rec} is the mean number of recombinations per hydrogen atom, the condition would become $\zeta f_{\mathrm{coll}} > (1 + N_{\mathrm{rec}})$. However, such a naive view does not provide a good match to more realistic calculations, because recombinations are actually quite inhomogeneous. Instead of globally slowing down reionization, they are relatively unimportant in the early stages but take over the process by the end (Choudhury et al., 2009; Furlanetto and Oh, 2005).

The final crucial ingredient we need to model reionization is the spectrum of the emitted photons. Stars are roughly blackbodies in the relevant regime (above the hydrogen ionization threshold of 13.6 eV), with

the peak of the intensity sitting at energies well below this ionization threshold for low mass stars. Thus, only high mass stars are important for reionization. Even then, their peak energy is much smaller than the ionization threshold of He^+ at 54.4 eV. With such soft photons, their precise spectra are usually unimportant, because the photons all have very short mean free paths through the neutral IGM: it generally suffices to assume that the photons are absorbed almost immediately upon impacting neutral gas. In detail, the photoionization cross sections for neutral hydrogen and helium affect the width of the ionization front that propagates into the IGM. The atomic physics of these processes are extremely well known and the problem can be solved exactly. The results show that the fronts are so narrow that their internal structures are all but unobservable. Stellar reionization therefore leads to a nearly two-phase medium: one very highly ionized that surrounds the sources, and another almost completely neutral far from those sources.

6.2 Sources of Reionization: Quasars

Although the most popular models for reionization appeal to stellar sources, it is possible that other agents may contribute to the reionization process. The most likely candidate is a population of massive black holes. When these black holes accrete matter, they can transform a substantial fraction of the rest energy of the accreting material into radiation (up to $\sim$40%, depending on the rotation of the black hole); such sources are known as quasars. The census of very luminous $z \sim 6$ quasars is now fairly well determined, and their abundance seems to decline rapidly at $z > 4$ (Willott et al., 2010). Although constraints on the shape of the luminosity function are quite weak, the total ionizing photon emissivity generated by this population of quasars appears to fall a factor of 10–50 short of that required to be responsible for reionization at $z \sim 6$.

Nevertheless, it is relatively easy to imagine that much smaller black holes could play an important role in at least partially ionizing the IGM, in particular black holes characteristic of the small galaxies common at high redshifts. At lower z, it is now clear that black holes are both ubiquitous and closely related to their host galaxies. The data show a tight relationship between the mass of a central galactic black hole and the velocity dispersion of the stars in the spherical component of the galaxy (as opposed to the disk, if it is present), at least at the present day (Gültekin et al., 2009). Unfortunately, it is not clear why such a correlation exists. It is consistent with any number of models, but most appeal to some sort of feedback

between the accreting black hole and the gas supply of the galaxy. It is also not clear how this correlation behaves at high z.

We can crudely gauge the potential importance of black holes to the reionization of the Universe. For the purposes of a simple estimate, we will simply scale the black hole mass M_{BH} to the total halo mass M_{h}, so that the mass density in black holes is $\rho_{\mathrm{BH}} = f_{\mathrm{BH}} f_{\mathrm{coll}} \bar{\rho}_{\mathrm{b}}$, where f_{BH} defines the fraction of collapsed baryonic mass inside of black holes and $\bar{\rho}_{\mathrm{b}}$ is the mean universal baryon density. We will scale f_{BH} to its local value in massive galaxies, $\sim 10^{-4}$.

Now let us consider how large this factor must be in order for high energy photons from accreting black holes to significantly ionize the IGM. To do so, we require several additional parameters.

1. First, these ionizations come from two sources: primary photoionization from the quasar photons and secondary ionizations from the energetic photoelectrons (as well as their secondaries). In a mostly neutral medium and in the high energy limit, the fraction $f_{\mathrm{ion}} \sim 1/3$ of the photoelectron energy ends up ionizing hydrogen atoms through these processes. Calculating this fraction requires some sophisticated machinery—including important inputs from atomic physics—that we will return to later.

2. Second, we need the efficiency with which black holes convert the accreted rest energy of particles into radiation; we write this factor as η and take a value near expectations for a nonrotating black hole, $\eta \approx 0.1$. This fraction is relatively easy to compute from GR, provided that the quasar does radiate all of this rest energy.

3. Finally, we suppose that the black holes emit a fraction f_{UV} of their energy above the H ionization threshold. This fraction is difficult to estimate from first principles, as it requires a sophisticated understanding of the accretion disks around black holes. However, it can be calibrated observationally.

Then, the expected ionizing energy output of the black hole population per unit volume is $f_{\mathrm{UV}} \eta \rho_{\mathrm{BH}} c^2$, implying the number of ionizations per H atom is

$$N_{\mathrm{ion}} \sim 0.5 \left(\frac{\eta}{0.1} \right) \left(\frac{f_{\mathrm{UV}}}{0.2} \right) \left(\frac{f_{\mathrm{coll}}}{0.01} \right) \left(\frac{f_{\mathrm{BH}}}{10^{-4}} \right) \left(\frac{f_{\mathrm{ion}}}{1/3} \right). \tag{80}$$

Here we have used the fact that for the hard spectra of interest secondary ionizations dominate over the initial photoionization, so we have neglected the latter. As emphasized above, we have scaled the most uncertain of these parameters, f_{BH}, to its local value. It is therefore quite plausible that quasars

make a substantial contribution to reionization. On the other hand, they are unlikely to be dominant. First, observations of the present day, soft X-ray background limit the high redshift background to be not much larger than that implied by Eq. (80) (Dijkstra et al., 2004a). Otherwise, very high-energy photons from that era (for which the IGM is nearly transparent) would have redshifted all the way to today's telescopes, overproducing the soft X-ray background. Second, as we shall see in the next section, less and less of the energy from each photon goes into ionization and more and more into heating as the ionized fraction increases (because the primary photoelectron encounters many more free electrons, rather than neutral atoms). Sources of high-energy photons generally have a difficult time completing reionization, even if they contribute to the early phases.

For these reasons, most astrophysicists assume that quasar radiation plays a subdominant role in the reionization process. But that is by no means a requirement of either models or data.

Since they can produce very high-energy photons, the spectra of quasars can be very important to understanding reionization, as the highest energy photons can propagate large distances through the ISM; photons with energies larger than ~ 1 keV can travel an entire Hubble length before interacting with the IGM. (The Hubble length is $c/H(z)$, the distance a photon can travel over one expansion time in the Universe. It thus characterizes the distance over which a photon will lose roughly half its energy to the cosmological redshift.)

If we imagine a source that produces a wide range of photon energies, we would therefore expect many photons to be absorbed near the source, but many others would reach some distance into the neutral IGM before interacting. Thus, in the case of a quasar source, many of the soft X-rays escape the ionized bubble but deposit their energy (as ionization and heat) in the surrounding gas, "preionizing" and "preheating" it before the ionization front itself reaches the gas. This would produce a qualitatively different sort of reionization from the two-phase medium characteristic of stellar sources.

6.2.1 Secondary Ionizations

From an atomic physics perspective, the fate of fast electrons (in our case, photoelectrons resulting from ionizations by very high-energy photons) scattering through the IGM is the most complex and interesting theoretical input to the reionization process. These electrons can deposit their energy in a variety of ways (Shull and van Steenberg, 1985): (1) through further

ionization of hydrogen or helium; (2) through scattering off of CMB photons; (3) through scattering off of free electrons; or (4) through collisional excitation of neutral hydrogen, neutral helium, or He$^+$.

Collisional ionization cross sections for high-energy collisions have been computed several times, but there is no exact solution. Johnson (1972) estimated the values for hydrogen analytically, finding that the high-energy limit obeys the Bethe approximation reasonably well. At lower energies, more accurate calculations show deviations. The most recent estimates (Furlanetto and Johnson Stoever, 2010) use values taken from the convergent close coupling (CCC) approximation (Bray et al., 2002).[14] The CCC approach is accurate whenever the target particle can be well modeled by one or two valence electrons above a Hartree–Fock core. Obviously, this is an excellent approximation for hydrogen and helium. These cross sections have only been computed for collision energies $E < 1\,\mathrm{keV}$, but the Bethe approximation appears to provide a good fit at the upper end of this range (and presumably at higher energies).

A second aspect of collisional ionization is less well quantified: the energy distribution of the secondary electrons produced. The only measurements are from Opal et al. (1971), from which Dalgarno et al. (1999) have constructed a phenomenological model. The analytic estimates of Johnson (1972) provide another approach for hydrogen, which produce qualitatively similar results. In either case, many of these secondary electrons also have rather high energies, whose fates must then also be followed as they scatter through the IGM.

Collisional excitation can be treated similarly, although some care is required because one would also like to trace the radiative cascades that follow (as some of the resulting photons, especially hydrogen Lyα as well as high-energy photons from helium which can ionize hydrogen, impact other aspects of the IGM, such as the 21-cm spin temperature). The CCC calculations include all levels through the Rydberg level $n = 4$; analytic estimates show that excitation to higher levels is subdominant in the cases of interest (Johnson, 1972; Xu and McCray, 1991). The calculations also stop at $E = 1\,\mathrm{keV}$, but the Bethe approximation again provides a reasonable fit at higher energies.

Most estimates of the energy deposition fraction for photoelectrons use a Monte-Carlo approach, following the energy loss through the series of interactions in the IGM (Furlanetto and Johnson Stoever, 2010; Shull

---

[14] See http://atom.curtin.edu.au/CCC-WWW/.

and van Steenberg, 1985; Valdés and Ferrara, 2008), tracing the fates of the secondary electrons as well. Figure 14 shows these energy deposition fractions from one such suite of simulations (Furlanetto and Johnson Stoever, 2010). This ignores Compton scattering, which depends strongly on redshift as the CMB energy density u_{CMB} is $\propto (1 + z)^4$. The various curves show different IGM ionized fractions (assuming that $x_{He\,II} = x_{H\,II}$); the abscissa shows the initial energy of the electron. Here x_X is the fractional abundance of ionization stage X relative to all nuclei of that element. Note how the fractions depend strongly on ionized fraction: when free electrons are common, fast electrons thermalize rapidly, depositing nearly all of their energy as heat. On the other hand, at low ionized fractions collisional excitation and ionization become much more important. At low energies, the line structure of hydrogen and helium imprint features on the curves, but at high electron energies the fractions converge to asymptotic values. Very roughly, these are $\sim x_{H\,I}/3$ for collisional excitation and ionization and $\sim (1 - 2x_{H\,I}/3)$ for heating.

These and other calculations show that, despite the relatively poorly quantified atomic physics for many of the input processes, the final results are fairly insensitive to the remaining uncertainties in these inputs. Residual uncertainties appear to be a few percent at most. Moreover, in the conventional picture in which most ionizing photons come from stars— in which case the photons are just above the ionization threshold and so must deposit all of their extra energy in heat—these calculations are largely irrelevant. Only if future observations show that quasars (or even more exotic processes) dominate the reionization epoch, will improvements in these calculations or measurements have interesting effects on the reionization process.

6.3 The Growth of Ionized Bubbles

The simplest reionization problem is to consider how a single, isolated galaxy ionizes its surroundings. The formation of H II regions (or ionized bubbles) around galaxies is the fundamental process driving reionization, although in practice these galaxies are only isolated during their very earliest phases.

The complete calculation requires a careful treatment of the radiative transfer of ionizing photons through the IGM. For simplicity, we consider a model Universe of only hydrogen; including helium complicates the equations but adds no essential new physics. As a photon travels away from its source, it encounters absorption that depends on the local ionized
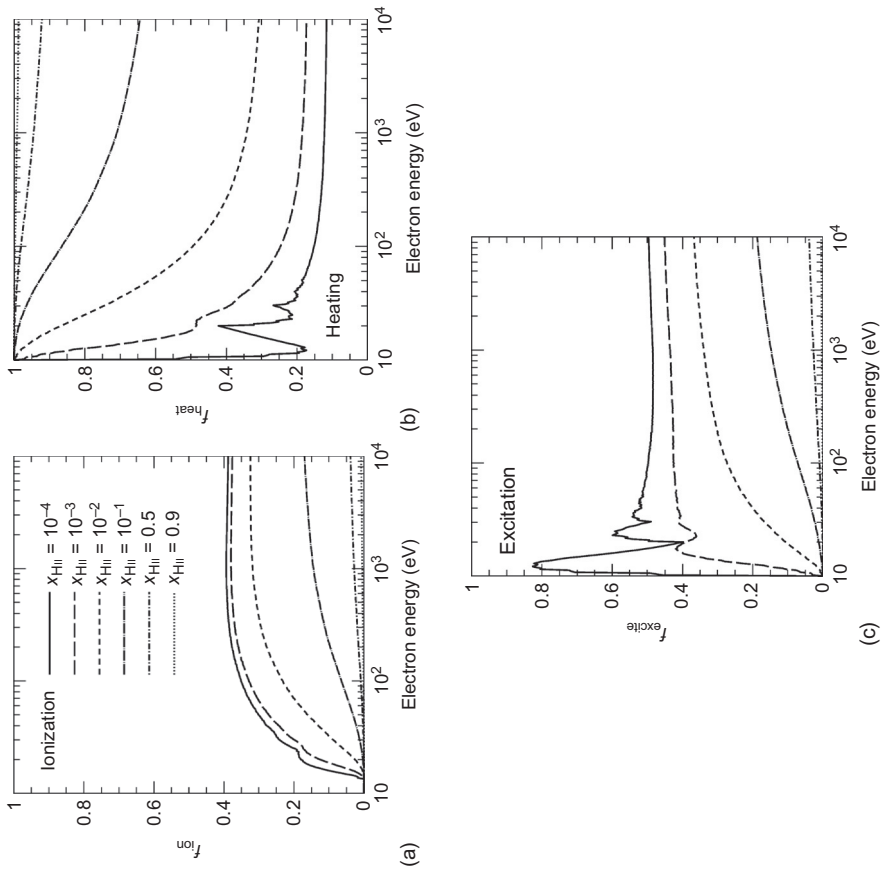
Fig. 14. Energy deposition fractions in ionization (a), heating (b), and collisional excitation (c) as a function of initial electron energy. The curves show results for several different IGM ionized fractions x_{HII}, as labeled in (a). *From Furlanetto and Johnson Stoever (2010).*

fraction as well as its energy. We parameterize the amount of absorption through the optical depth, τ_ν. The differential along a line of length ℓ is given by $d\tau_\nu = \alpha_\nu d\ell$, where α_ν is the absorption coefficient (or the probability of absorption per unit length).

The total optical depth experienced by a photon with frequency ν that has traveled from a source to a radius or distance r at time t is

$$\tau(\nu, r, t) = \int_0^r \sigma_{\mathrm{H\,I}}(\nu) n_{\mathrm{H\,I}}(r', t') dr', \tag{81}$$

where $\sigma_{\mathrm{H\,I}}$ is the photoionization cross section of H, $n_{\mathrm{H\,I}}$ is the local neutral hydrogen number density (which may evolve either with the cosmic expansion or as the neutral fraction changes), and t' is the time at which the photon passed a distance r'. We have explicitly noted the time dependence, as the ionized region will grow as more and more photons are pumped into it. We have also assumed that $r \ll c/H(z)$, so that we can ignore cosmological redshift.

The ionization rate for a neutral H atom at this position (expressed per unit time) is then

$$\Gamma_{\mathrm{H\,I}}(r, t) = \int_{\nu_{\mathrm{H\,I}}}^\infty \frac{d\nu}{2\pi\hbar\nu} \frac{L_\nu e^{-\tau(\nu,r,t)}}{4\pi r^2} \sigma_{\mathrm{H\,I}}(\nu) \left[1 + \left(\frac{E'}{E_{\mathrm{H\,I}}}\right) f_{\mathrm{ion}}(E')\right], \tag{82}$$

where L_ν is the monochromatic luminosity (per unit frequency) of the source, $E' = E - E_{\mathrm{H\,I}}$ the energy of the photoelectron following an ionization with photon energy $E = 2\pi\hbar\nu$, and $E_{\mathrm{H\,I}} = 13.6\,\mathrm{eV}$ the ionization potential of neutral hydrogen (and $\nu_{\mathrm{H\,I}}$ the corresponding frequency). The quantity $f_{\mathrm{ion}}(E - E_{\mathrm{H\,I}})$, introduced in Section 6.2, is the fraction of the energy of the photoelectron that goes into secondary ionizations as it scatters through the ambient medium (see Fig. 14).

The ionized fraction at each position is then governed by the rate equation

$$\frac{dn_{\mathrm{H\,I}}}{dt} = \Gamma n_{\mathrm{H\,I}} - \alpha_{\mathrm{B}}(T) n_e n_{\mathrm{H\,II}}, \tag{83}$$

where $n_e = n_{\mathrm{H\,II}} = n_{\mathrm{H}} - n_{\mathrm{H\,I}}$. The radiative recombination rate coefficient, $\alpha(T)$, determines the speed of the crucial "sink" term in reionization. Here we use the so-called case-B value, which assumes that photons generated by direct recombinations to the ground state are absorbed instantaneously (known as the "on-the-spot" approximation). Otherwise, the radiative transfer equation must include a source term for these reprocessed photons. We discuss recombinations more in Section 6.3.1.

Because the recombination rate depends on temperature T (and often because the temperature is of intrinsic interest), one must also trace its evolution. For gas at the mean cosmological density, the relevant equation is

$$\frac{dT}{dt} = -2HT - T\frac{d\ln(2 - x_{HI})}{dt} + \frac{2}{3k_B n_{tot}}(\mathcal{H} - \Lambda). \qquad (84)$$

Each of the terms has a simple physical interpretation. The first describes adiabatic cooling as the Universe expands: for a nonrelativistic gas, $T \propto V^{-5/3}$, where $V \propto a^3$ is the volume. Together these imply $\dot{T}/T = -(2/3)(\dot{V}/V) = -2HT$. The second term describes the repartition of energy between particles as the gas is ionized (which tends to counteract the heating you expect from photoionization). Finally, $\mathcal{H}$ is the total radiative heating rate, Λ is the total radiative cooling rate, and $n_{tot} = n_{HI} + n_{HII} + n_e + n_{HeI} + n_{HeII} + n_{HeIII}$ is the total particle density.

At high redshifts, radiative heating and cooling are typically dominated by photoheating and inverse Compton cooling, respectively. Neglecting helium for simplicity, the photon heating rate is given by

$$\mathcal{H}_{ph} = \int_{\nu_{HI}}^{\infty} d\nu \, \frac{L_\nu e^{-\tau(\nu,r,t)}}{4\pi r^2} \sigma_{HI}(\nu) E' f_{heat}(E'), \qquad (85)$$

where $f_{heat}(E')$ is the fraction of the photoelectron energy that goes into heating the gas (see Section 6.2.1 and Fig. 14). This term accounts for the energy deposited in the primary photoelectron, over and above that required to ionize the atom. Much of this energy will be thermalized on a short timescale as the electron scatters through the IGM. Inverse Compton cooling describes the scattering of low-energy CMB photons by hot electrons, leading to a net decrease in the energy density of the electron gas. The Compton cooling rate Λ_{Comp} is given by (see Chapter 2 of Loeb and Furlanetto, 2013)

$$\frac{2}{3}\frac{\Lambda_{Comp}}{k_B n_{tot}} = \frac{1 - x_{HI}}{2 - x_{HI}}\frac{(T_{CMB} - T)}{t_C}, \qquad (86)$$

where $t_C \equiv (3m_e c)/(8\sigma_T u_{CMB})$ is the Compton cooling time, σ_T is the Thomson cross section, and $u_{CMB} \propto T_{CMB}^4$. The first factor on the right hand side of Eq. (86) accounts for energy sharing by all free particles.

Compton cooling most often dominates, but in some regimes—particularly those at the leading edge of an ionization front—radiative line cooling by collisions can also be important. Typically, the ionization front heats the gas to $T > 20,000\,K$, just above the threshold for exciting

the upper levels of neutral H (this temperature requires only ~1 eV of extra energy per ionization). These transitions are then excited by collisions between the remaining neutral atoms and fast-moving free electrons, and they cool the gas until either the neutral gas disappears or until the gas cools enough that the transitions can no longer be excited efficiently. We will discuss this line cooling in more detail in Section 6.3.2.

Because the heating process is not an equilibrium one, the final temperature of the gas after the ionization front passes is difficult to estimate without recourse to detailed simulations. But it certainly depends upon both the spectrum of the sources—more high-energy photons allow much more room for heating, as each photoelectron has a much higher energy—and the absorbers—as the incident spectrum is filtered by absorption nearer the source. For example, if a dense, neutral region sits in front of the source, only high-energy photons will strike gas parcels at larger distances, making them hotter than otherwise expected.

Figure 15 shows some example ionization and temperature profiles around a relatively faint quasar at $z = 10$ that produces 10^{55} ionizing photons per second. The source is assumed to emit steadily after it turns on, and the different curves present $t = 10^6$, $10^{6.5}$, 10^7, $10^{7.5}$, and 10^8 year after ignition. (Current constraints on the lifetimes of bright quasar phases are weak, but they are thought to live for ~10^7–10^8 year.) The calculation assumes an initial IGM temperature of $T = 10\,\mathrm{K}$ (which corresponds to very minimal preheating) and a uniform IGM at the mean density. As expected, the ionization front sweeps outward over time. Behind it, the gas lies in ionization equilibrium, with $x_{\mathrm{H\,I}} \propto r^2$ but always very small (so it appears to be nearly completely ionized in the plot). The ionization front itself is narrow, but residual ionization (and heating, which can be substantial) extends several comoving Mpc ahead of the front. The gas preceding the ionization front is not in ionization equilibrium, as the ionization front will continue to sweep outward if the source remains luminous, and the gas outside will steadily increase both temperature and ionized fraction.

This long tail outside of the ionized bubble is characteristic of quasars. Stars have much simpler ionized regions. Their soft photons are all absorbed in a narrow region just past the ionization front. The resulting "two-phase" medium—without the long tails of weak ionization and heating visible in Fig. 15—lends itself to simpler approximations. In the absence of recombinations, each H atom in the IGM would only have to be ionized once. The size of the resulting ionized region depends on the number
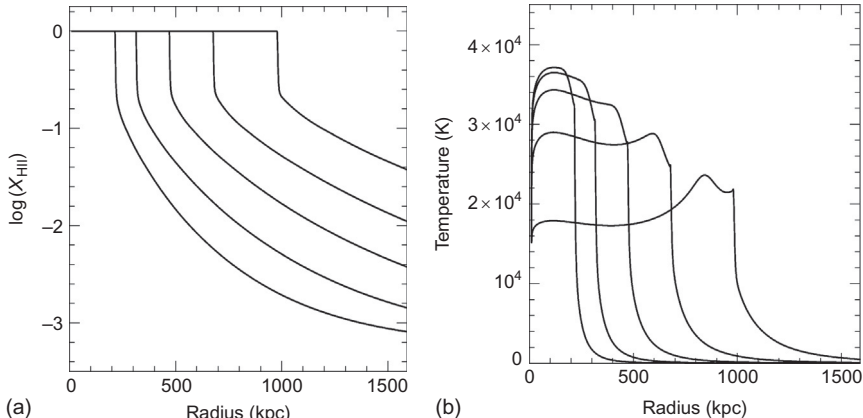
Fig. 15. Example ionization and temperature profiles around a relatively faint quasar at $z=10$ that produces 10^{55} ionizing photons per second. The source is assumed to emit steadily after it turns on. From left to right, the different curves show $t = 10^6$, $10^{6.5}$, 10^7, $10^{7.5}$, and 10^8 year after ignition. The calculation assumes an initial IGM temperature of $T = 10$ K and a uniform IGM at the mean density (including helium); note that distances are measured in proper units.

of ionizing photons produced by the source, or under the simplifying assumptions of the previous section, the mass of the halo which produces it: it is just a local region with $\zeta f_{coll} = 1$. Let us consider a halo of total mass M_h that produces N_{ion} ionizing photons, where $N_{ion} = \zeta(\Omega_b/\Omega_m)(M_h/m_p)$. If the mean comoving hydrogen number density is $\bar{n}_H^0$, we find[15]

$$
r_{max} = \left(\frac{3}{4\pi} \frac{N_{ion}}{\bar{n}_H^0} \right)^{1/3} = \left(\frac{3}{4\pi} \frac{\zeta}{\bar{n}_H^0} \frac{\Omega_b}{\Omega_m} \frac{M_h}{m_p} \right)^{1/3}
$$
$$
= 680 \, \text{kpc} \left(\frac{\zeta}{40} \frac{M_h}{10^8 M_\odot} \right)^{1/3} . \tag{87}
$$

This is many times the size of the galaxy itself, so ionized bubbles are generically expected to be very large.

However, the elevated density of the IGM at high redshift implies that recombinations cannot be ignored, so this simplest method must be improved. In the case of a steady ionizing source (and neglecting the cosmological expansion), an equilibrium volume (termed a "Strömgren Sphere" and named after a Danish astronomer who studied the analogous problem around hot stars) would be reached, throughout which recombinations

---

[15] Again, we neglect the presence of helium here for simplicity.

balance ionizations:

$$\alpha_B \bar{n}_H^2 V_p = \frac{dN_{ion}}{dt} \; , \tag{88}$$

where the recombination rate depends on the square of the mean proper density, $\bar{n}_H = (1 + z)^3 \bar{n}_H^0$, V_p is the proper volume of the sphere, and dN_{ion}/dt is the rate at which the source produces ionizing photons. Again, we assume the case-B value here, which means that any ionizing photons resulting from recombinations to the ground state would contribute to the growth of the Strömgren sphere itself.

To model the evolution of the ionized bubble in this two–phase approximation, including a nonsteady ionizing source, recombinations, and cosmological expansion, we write (Shapiro and Giroux, 1987)[16]

$$\bar{n}_H \left(\frac{dV_p}{dt} - 3HV_p \right) = \frac{dN_{ion}}{dt} - \alpha_B \langle n_H^2 \rangle V_p \; , \tag{89}$$

where the angle brackets denote a volume average. Here the right-hand side includes the source and sink terms, so the left-hand side would equal zero in the Strömgren limit within a static Universe. The region can grow for two reasons. The first is if the number of ionizing photons exceeds the number of recombinations: in that case, the ionized bubble grows, which corresponds to the first term. In addition, the bubble will grow as the Universe expands (i.e., z decreases), simply because the mean density of the Universe declines ($\bar{n}_H \propto [1 + z]^3$) so that the recombination rate falls with time.

6.3.1 Photoionization Rates and Recombinations

The photoionization cross section for hydrogen is well known and can be calculated to high accuracy very efficiently; see, for example, Storey and Hummer (1991) for a detailed discussion. Helium is more complex, but has been studied in great detail. Verner et al. (1996) collected data from the Opacity Project (Seaton et al., 1992), which used R-matrix methods to produce cross sections for many atoms of particular interest. Verner et al. (1996) present convenient analytic fits to these results, smoothed over resonances.

---

[16] We caution the reader that this equation should only be applied to the expanding stage in the life of an ionized bubble, as it does not properly distribute the recombinations through space. Moreover, it does not describe the early phases of expansion accurately, because it does not account for the time delay as the light propagates outward.

On the other hand, the recombination term provides one of the most important uncertainties in reionization calculations—though not because of uncertainties in the atomic physics. The recombination coefficient to a given Rydberg and angular momentum nL level is

$$\alpha_{nL} = \int \sigma_{nL}(v)vf(v)\mathrm{d}v, \qquad (90)$$

where σ_{nL} is the recombination cross section, v the velocity, and $f(v)$ the relative electron–ion velocity distribution. The cross section $\sigma_{nL} \propto v^{-2}$ (roughly), so the recombination coefficient decreases with increasing gas temperature. At the $T \approx 10^4\,\mathrm{K}$ typical of ionized regions, this cross section is many times smaller than both the photoionization cross section and the electron scattering cross section, which means that the electron gas thermalizes long before recombination occurs, so $f(v)$ always follows a Maxwell–Boltzmann distribution. The dependence on gas temperature introduces one uncertainty to the calculation. This temperature, in turn, depends on nonequilibrium processes during reionization, which cannot be followed in many approximate treatments.

Assuming a Maxwell–Boltzmann distribution, the recombination coefficients to a given state can be deduced directly from the photoionization cross sections using the Milne relations. Ferland et al. (1992) describe this procedure in detail for hydrogen, while Verner and Ferland (1996) present results for helium (based on their fits to the photoionization cross sections in Verner et al., 1996).

For singly ionized helium, there is also the possibility of dielectronic recombination, in which the excess energy from the recombining electron excites the bound electron rather than triggering radiation. This must be computed separately. It has received less attention but is highly subdominant in most regimes (Aldrovandi and Pequignot, 1973).

Of course, recombinations can occur to many different levels, over which we must sum in order to extract the total recombination rate. This introduces another substantial uncertainty to reionization calculations, because it is not always clear which terms in the sum should be retained; this is the difference between case-A and case-B recombination (the former includes recombinations to the ground state, while the latter does not). It is not atomic physics but an environmental factor—again very difficult to quantify—that determines which of these is the more appropriate limit (Miralda-Escudé, 2003). On the one hand, suppose that ionizations (and hence recombinations) are distributed uniformly throughout the IGM. Then any ionizing photons produced by recombinations to the ground state

would be produced in a highly ionized medium and could easily travel to the nearest IGM neutral atom. They would therefore contribute to further ionizations of the IGM, and case B would be appropriate, as assumed in Eq. (83).

On the other hand, in the highly ionized, low redshift Universe, most recombinations actually take place inside dense, partially neutral clouds. The high-energy photons that propagate large distances in the IGM can penetrate such high column density systems, where they finally manage to ionize a hydrogen atom. However, in this dense region the atom quickly recombines. Any ionizing photons produced after recombinations to the ground state usually lie near the Lyman limit (where the mean free path is small) so they are consumed inside the systems. Thus, these photons would not help ionize the IGM, and case A would be more appropriate. Which of these regimes is more relevant depends on the details of small-scale clumping and radiative transfer and will evolve as reionization progresses, which we will explore further below.

The level-dependent recombination rates also potentially affect observable signals of the recombining gas, which could in principle be imaged through the recombination lines. However, estimates show that this recombination radiation is far beyond the capabilities of existing instruments (e.g., Fernandez et al., 2010).

A final uncertainty in the recombination term comes from its density dependence. If the IGM is not uniform, but contains high-density clumps separated by modestly underdense voids—as in the real Universe—recombinations will become more important, because of the density-squared weighting of the collisional process. This is often accounted for by introducing a volume-averaged clumping factor C (which is, in general, time dependent), defined by

$$C = \langle n_{\mathrm{H}}^2 \rangle / \bar{n}_{\mathrm{H}}^2 . \tag{91}$$

This factor is difficult to calculate, as one must (1) trace the gas distribution with sufficient precision to resolve density fluctuations on the smallest scales (Mellema et al., 2006); (2) correctly trace the topology of ionized and neutral gas—since the average must be performed only over the ionized gas (Furlanetto and Oh, 2005); and (3) correctly model the evolution of gas clumps during the reionization process itself, during which photoheating will increase the gas temperature and hence pressure, smoothing out some of the clumps (Pawlik et al., 2009). There is no complete model of the effect of clumping on reionization, though simulations suggest that the effects are

modest at the high z of interest (with $C < 5$ according to most models; McQuinn et al., 2007; Pawlik et al., 2009).

In a perfect world, these uncertainties could be settled by detailed radiative transfer calculations of the reionization process. Unfortunately, such calculations are currently beyond the power of even the most powerful computers, as they require multifrequency radiative transfer with exquisite spatial resolution.

We emphasize again that, though this atomic physics process (recombination) introduces substantial uncertainty to the reionization models, the uncertainty is not due to the atomic physics but rather the astrophysical context.

6.3.2 Line Cooling

The other atomic physics input to the calculation is line cooling by collisional excitation. In ionized regions near or inside the Milky Way, this can be quite complex, as a number of atoms and their lines must be considered, from resonance transitions to forbidden lines. However, for cosmological reionization, the calculation is much easier: the primordial gas includes only hydrogen and helium, so it is only their line transitions that are relevant. The best estimates in the astronomical literature are fits to measurements and/or calculations that are several decades old (Black, 1981; Giovanardi and Palla, 1989; Giovanardi et al., 1987). These could probably be improved with new theoretical calculations; however, the astrophysical uncertainties (in the density structure and spectrum of the sources) are almost certainly larger than the uncertainties in these rates. Nevertheless, as theoretical calculations and observations improve, it may be necessary to revisit collisional excitation rates for transitions relevant to primordial gas at $T \sim 10,000$–$30,000\,\mathrm{K}$ in order to predict the resulting temperatures.

Note that the excitation rates to individual angular momentum states are also relevant, because photons from the various line transitions could be detectable (at least in principle) and Lyα photons in particular may affect the IGM spin temperature (see Section 5). For example, Cantalupo et al. (2008) suggest that the line cooling from the ionization front may be visible in deep imaging of the regions around extremely luminous quasars. Although the resulting emission has a very low surface brightness, the large angular extent of the ionization front may render the total emission visible. This possibility is just beginning to be explored, and the extent to which the predicted signals depend on the atomic physics uncertainties remains to be seen.

6.4 Reionization as a Global Process

Having tackled the small–scale details of reionization, the next level of sophistication is to compute the evolution of the average neutral fraction across the entire Universe. We obtain a first estimate for the requirements by demanding one stellar ionizing photon for each hydrogen atom in the Universe. Using the "two–phase" approximation appropriate for stellar sources, then to zeroth order, the accounting is relatively simple: the efficiency parameter ζ that we introduced in Section 6.1 is simply the number of ionizing photons produced per baryon inside galaxies; thus the ionized fraction (ignoring recombinations) is

$$Q_{\mathrm{H\,II}} = \zeta f_{\mathrm{coll}}, \tag{92}$$

where $Q_{\mathrm{H\,II}}$ denotes the filling factor of ionized bubbles (i.e., the fraction of the volume of the Universe inside of H II regions).

As in the case of a single bubble, recombinations are likely to be at least modestly important. However, we can make the simple but reasonable approximation that the volume ionized by each source is an extensive quantity, so that we can simply add the ionized volume from all sources together. Then, in terms of the filling factor $Q_{\mathrm{H\,II}}$ (for which the expansion of the Universe does not matter), we can rewrite Eq. (89) as

$$\frac{\mathrm{d}Q_{\mathrm{H\,II}}}{\mathrm{d}t} = \zeta \frac{\mathrm{d}f_{\mathrm{coll}}}{\mathrm{d}t} - \alpha(T)C\bar{n}_{\mathrm{H}}Q_{\mathrm{H\,II}}, \tag{93}$$

where we have replaced the density factor with the clumping factor C. This is not a perfect approximation, since more of the photons will be absorbed internally as the bubbles overlap and grow, but those effects are much smaller than the uncertainties in parameterizing both the ionizing efficiency of the sources and clumpiness.

The middle panel of Fig. 12 shows an example ionization history computed with Eq. (93). This model takes $\zeta = 40$, which is typical for Population II stars assuming that $f_\star \approx 10\%$ and $f_{\mathrm{esc}} \approx 10\%$. It also does not allow stars to form in halos below the threshold for atomic hydrogen cooling. Under these conditions, reionization completes at $z \approx 8$. The process is also quite fast: this is because while halos massive enough to reach this cooling threshold (which corresponds to $M \sim 10^8 \, M_\odot$) are far above the characteristic mass scale at high redshifts, their abundance increases almost exponentially fast with decreasing redshift, for example, Eq. (46). This kind of rapid increase in the ionized fraction is generic to models in which the parameters of star-forming galaxies do not change.

However, the timing of reionization is almost unconstrained by theory because of the fundamental uncertainties in the properties of the first stars and galaxies. This is the most basic reason that observations of reionization are so useful; they provide an integral constraint on all the ionizing sources in the first generations of structure formation, or a first cut at understanding what kinds of stars formed in the early Universe.

To date, such constraints are quite weak. Observations of the Lyα forest toward distant quasars show that the Universe is highly ionized by $z \sim 6$, so reionization must at least be nearly over by then (Fan et al., 2004; Mesinger, 2010). The polarization of the CMB also constrains the ionization history, as Thomson scattering in the ionized IGM generates polarization. The most recent measurements, by *WMAP*, indicate that the midpoint of reionization occurred at $z \sim 10$ (Komatsu et al., 2011). Other, more model–dependent measurements, may indicate that the bulk of reionization occurs somewhat later than that (Fan et al., 2006).

Although the global evolution described by Eq. (93) contains a great deal of astrophysics, it only describes the average properties of reionization. The spatial properties of the ionization field (cf., Fig. 16) are even more interesting. In particular, the ionization history likely evolves through two basic phases:

1. **The bubble–dominated phase:** As described above, the bubbles generated by galaxies inevitably overlap. If we imagine a clump of star–forming galaxies, each producing their own ionizing photons, those bubbles will quickly overlap with each other. This overlap process is volume conserving; however, the photons that would have ionized the region near their source are now free to travel farther and ionize more distant gas. Thus, the small bubbles generated by single sources can join together into much larger structures. Models predict that these bubbles quickly reach radii of a megaparsec and, during the middle stages of reionization, ten or more megaparsecs (Furlanetto et al., 2004).

   The size distribution of these bubbles is an extremely useful observable, because it depends primarily on (1) the degree of ionization (or $Q_{\mathrm{H\,II}}$) and (2) the clustering of the ionizing sources. Bubbles grow larger throughout the reionization era, and the filling factor of these ionized bubbles is the single most important factor in determining their characteristic size (Furlanetto et al., 2006a). The second most important factor is how clustered the ionizing sources are. According to structure formation models, this clustering depends entirely on the mass of the host halo: more massive dark matter halos are much more highly
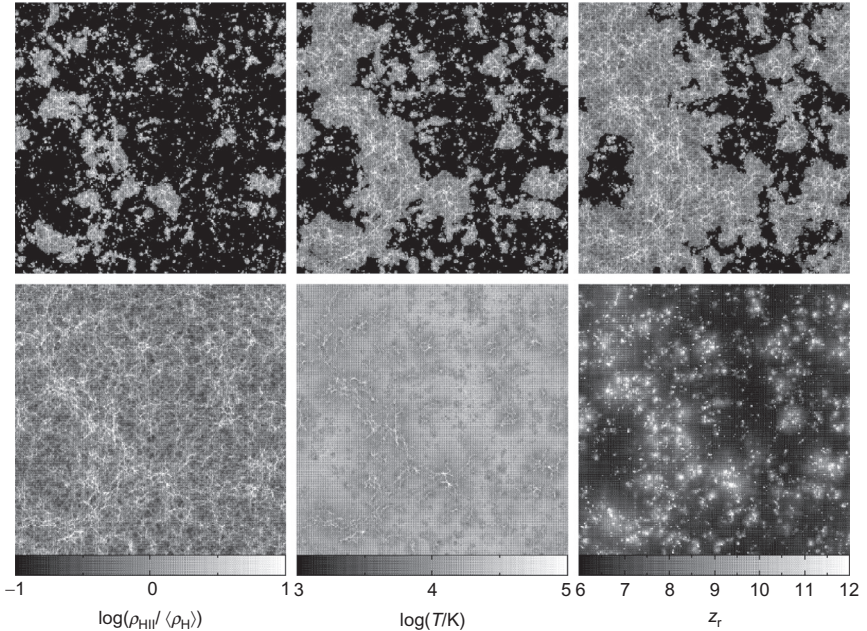
Fig. 16. Snapshots from a numerical simulation illustrating the spatial structure of reionization in a slice of 140 comoving Mpc across. The simulation includes the dynamics of the dark matter and gas as well as the radiative transfer of ionizing radiation from galaxies. The first four panels (reading across from top left to bottom left) show the evolution of the ionized hydrogen mass density $\rho_{H\,II}$ normalized by the mean proton mass density in the IGM $\langle \rho_H \rangle$ when the simulation volume is 25%, 50%, 75%, and 100% ionized, respectively. The bottom middle panel shows the temperature at the end of reionization while the bottom right panel shows the redshift z_r at which different gas elements are reionized. Higher-density regions tracing the large-scale structure are generally reionized earlier than lower-density regions far from sources. At the end of reionization, regions that were last to be ionized and heated are still typically hotter because they have not yet had time to cool through the cosmic expansion. Courtesy of H. Trac and A. Loeb (private communication).
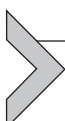
clustered than their smaller cousins. This means that scenarios where most star formation occurs inside large halos result in relatively few, but large, ionized bubbles, while scenarios in which most star formation occurs inside small dark matter halos have many small ionized bubbles (Furlanetto et al., 2006a).

Thus, measuring the distribution of these ionized bubbles provides information about both the progress of reionization and the dark matter halos in which early galaxies live. Although it is difficult to measure, there are several techniques now under development to observe

this distribution, most notably the spin–flip background described in Section 5. Fortunately, the physics behind these effects is relatively straightforward and well understood (Furlanetto et al., 2004).

2. **The web–dominated phase:** The overlap of bubbles surrounding clustered sources drives the early part of reionization. However, once the bubbles grow sufficiently large, the other half of the ionizing equation—the sinks—starts to become important (Furlanetto and Oh, 2005). Because the IGM is inhomogeneous, the overall recombination rate is dominated by a small fraction of the volume of the Universe, which contains the densest regions. So long as the ionized bubbles are small, a typical ionizing photon will hit the edge of the bubble—and therefore ionize fresh material—before hitting one of these dense regions. Recombinations can therefore be mostly ignored in the early stages. However, as the bubbles grow, more and more photons will find one of these recombining blobs before encountering the edge of their ionized bubbles. Once the bubbles are larger than the spacing between the dense regions, recombinations come to dominate the spatial distribution of the reionization process.

   The point at which this occurs is uncertain, as it depends sensitively on the (unobserved) small–scale structure of the IGM at $z > 6$. But it will regulate the transition to the highly ionized Universe that we see today, and it may have a dramatic effect on reionization (Choudhury et al., 2009). Some of these effects manifest themselves in the post–reionization IGM temperature, shown in the bottom middle panel of Fig. 16.

7. SUMMARY

Knowledge of AMO physics informs our understanding of the early Universe as it evolves from recombination to reionization. Upcoming observational advances described earlier are expected to enable us to more deeply probe this epoch of history. AMO processes imprint features on the observed spectra which can provide us with observational constraints for the physical conditions during this epoch. The evolution of the early Universe is also controlled, in part, by AMO physics. In this review, we have explored the many roles that AMO processes play in our understanding of this billion–year–long epoch.

One of the goals for AMO scientists working in this area of cosmology is to reduce uncertainties in our knowledge of the relevant AMO physics to the point where remaining differences between models and between models and observations can tell us something about the underlying astrophysics. Moreover, the focus of such AMO studies is on those AMO uncertainties which most limit our astrophysical understanding.

Taking this as a guide, there are a number of outstanding AMO issues which remain to be resolved. During cosmological recombination, the available recombination data for forming He I are lacking in completeness. It would be very useful to have j-resolved radiative transition rates, frequencies, and differential photoionization cross sections up to $n \sim 50$–100. Additionally, collisional transition rates are needed for Rydberg states in H I, He I, and He II. Important colliders include electrons and protons. Also important are data for changes of $\Delta l > \pm 1$. All these uncertainties affect the predicted recombination dynamics and associated spectral distortions. For pregalactic gas, vibrationally resolved data are needed, particularly for H_2^+, in order to model the final H_2 abundance and associated cooling. Moving on to modeling Population III star formation, particularly critical are data for three-body recombination forming H_2 and more reliable approximations used to treat optically thick H_2 cooling.

As for the AMO data for the physics of 21-cm emission, they appear to be adequately known for the upcoming generation of observatories. Meanwhile, for reionization of the Universe, though there are a couple of outstanding AMO issues, resolving those issues are of reduced importance given the yet larger uncertainties in the astrophysical context. Still, as we conclude this review, it almost goes without saying that as the observational capabilities of the field improve, enabling yet higher precision cosmological studies to be carried out, that will likely entail corresponding new AMO data needs beyond those highlighted here.

Appendix A. ACRONYMS

Table A1 List of Acronyms Used in the Text

Acronym	Meaning
AMO	Atomic, molecular, and optical
Brα	Brackett-α
CCC	Convergent close coupling
CDM	Cold dark matter
CIE	Collision–induced emission
CMB	Cosmic microwave background
GR	General relativity
Hα	Balmer-α
IGM	Intergalactic medium
ISM	Interstellar medium
LTE	Local thermodynamic equilibrium
Lyα	Lyman-α
Lyβ	Lyman-β
Pα	Paschen-α
RMS	Root mean square
ΛCDM	Λ cold dark matter
1D	One–dimensional
3D	Three–dimensional

Table B1 List of Symbols Used, Their Definitions, and the Sections Where They Are Used

Symbol	Definition	Sections					
A	Atomic weight	1	...	...	...	...	...
A_{He}	$4/(4 - 3Y_p) = 1.22$	...	...	...	...	5	6
A_{ji}	Spontaneous radiative transition rate from level j to level i	...	...	...	4	5	...
A_{2s1s}	Transition rate for the 2s–1s two photon decay in H I	...	2	...	...	...	...
A^*_{21}	Effective Lyα transition rate in H I	...	2	...	...	...	...
a	Cosmic scale factor $1/(1 + z)$ normalized to unity at $z = 0$	1	...	...	4	...	6
a_{em}	Cosmic scale for light emitted at a redshift z_{em}	1	...	...	...	...	...
a_Λ	Cosmic scale factor when the Universe becomes dominated by the cosmological constant	1	...	...	...	...	...
B_ν	CMB blackbody spectral intensity with frequency	...	2	...	...	...	...
C	Volume averaged clumping factor	...	...	...	...	...	6
C^i_{10}	Collisional de-excitation rate from singlet to triplet H due to collisions with species i	...	...	...	...	5	...
c	Speed of light	...	...	...	...	5	6
c_s	Sound speed	...	...	...	4	...	...
D_+	Linear growth factor	...	...	...	4	5	...
E	Energy	...	...	3	...	...	...
E'	Photoelectron energy	...	...	3	...	...	6
E_{det}	Detachment energy	...	...	3	...	...	6
E_{diss}	Dissociation energy	...	...	3	...	...	...

Continued

Table B1 List of Symbols Used, Their Definitions, and the Sections Where They Are Used—cont'd

Symbol	Definition	Sections				
$E_{H\,I}$	Ionization potential of H	...	...	...	...	6	...
$E_{JJ'}$	Energy separation between rotational levels J and J'	...	...	4	...	...	...
E_{ji}	Energy separation between levels j and i	...	...	4	...	...	...
e	Elementary charge	...	...	...	5	...	...
F	Quantum number obtained from adding J and I	...	...	...	5	...	...
$f(v)$	Relative electron–ion velocity distribution	...	...	...	...	6	...
f_{BH}	Fraction of collapsed baryonic mass inside of black holes	...	...	...	...	6	...
f_{coll}	Fraction of all baryons collapsed into halos	...	...	...	...	6	...
f_{esc}	Fraction of ionizing photons that escape a host galaxy into the IGM	...	...	...	5	6	...
f_{excite}	Fraction of energy deposition due to collisional excitation	...	...	...	...	6	...
f_{heat}	Fraction of initial photoelectron energy that goes into heating gas	...	...	...	...	6	...
f_{ion}	Fraction of initial photoelectron energy which ends up ionizing H	...	...	...	...	6	...
f_j	Fraction of H$_2$ molecules in level j	...	...	4	...	...	...
f_{UV}	Fraction of black hole energy emitted above H ionization threshold	...	...	...	...	6	...
f_X	X-ray emissivity	...	...	...	5	...	...
f_α	Lyα emissivity	...	...	...	5	...	...
f_α^{osc}	Oscillator strength of the Lyα transition	...	...	...	5	...	...
f_τ	Density-dependent suppression factor	...	...	4	...	...	...
$f_\star$	Fraction of baryonic material a galaxy can transform into stars.	...	...	...	...	6	...
G	Gravitational constant	1	...	4	...	...	...
g_i	Statistical weight of the i hyperfine level in ground state H	...	...	...	5	...	...
H	Hubble parameter as a function of a or z	1	3	4	5	6	...

		1	2	3	4	5	6	7
$\mathcal{H}$	Total radiative heating rate						6	
H'	H/H_0				4			
$\mathcal{H}_{\mathrm{ph}}$	Photoheating rate due to H I						6	
H_0	Hubble constant, i.e., present–day value of H	1	2		4	5		
h	$H_0/(100\,\mathrm{km\,s^{-1}\,Mpc^{-1}})$		2		4	5		
$\hbar$	Planck's constant divided by 2π					5	6	
I	Nuclear spin quantum number					5		
J	Total angular momentum of an atom		2		4	5		
J	Rotational quantum number of a molecule							
j	Total angular momentum of a bound electron		2		4			7
J_α	Specific (number) flux of Lyα photons					5		
J_α^{C}	Critical Lyα flux required to affect T_{S}					5		
J_ν	Mean flux number versus frequency ν					5		
K	Kinetic energy				4			
k_{B}	Boltzmann constant	1	2		4	5	6	
k_{ra}	Radiative association rate coefficient for e^- and H				4			
k_{rec}	Radiative recombination rate coefficient of H^+				4			
k_{X}	Rate coefficient for reaction number X			3				
L	Total orbital angular momentum of an atom		2			5	6	
L_ν	Monochromatic luminosity per unit frequency						6	
ℓ	Line length						6	
l	Orbital angular momentum quantum number		2					
M	Mass				4		6	

Continued

Table B1 List of Symbols Used, Their Definitions, and the Sections Where They Are Used—cont'd

Symbol	Definition	Sections
M_{BH}	Black hole mass	6
M_h	Halo mass	6
M_J	Jeans mass	4
$M_\star$	Stellar mass	6
$M_\odot$	Solar mass	4
m	Magnetic quantum number	2
m_X	Mass of species X	5, 6
N_e	Number density of free electrons	2
N_H	Number density of hydrogen nuclei	2
N_{He}	Number density of helium nuclei	2
N_i	Number density of species i	2
N_{ion}	Number of ionizing photons emitted per baryon inside stars or black holes	5, 6
N_n	Number density of H atoms with an electron in the n shell	2
N_{nl}	Number density of H atoms with an electron in the nl level	2
N_p	Number density of free protons	2
N_{rec}	Mean number of recombination per H atom	6
$N_{\gamma,0}$	Present-day CMB photon number density	2
N_{1s}	Number density of ground state H atoms	2
$N(M,z)$	Number density of halos in mass range M to $M+dM$	4, 5
n	Principle quantum number	2, 6, 7
n	Gas number density	4
n_{crit}	Critical gas density where internal excitation of a molecule approaches LTE	4
$\bar{n}_H$	Mean proper H number density	6

Symbol	Description						
$\bar{n}_H^0$	Mean comoving H number density	...	...	...	...	...	6
n_{Hn}	Number density of H nuclei	...	...	3	4	5	...
n_{max}	Highest n used in the recombination models	...	2	...	...	...	...
n_X	Number density of species X	...	...	3	4	5	6
n_γ	Photon number density	1	...	...	...	...	...
n_ν	Photon occupation number	...	...	...	...	5	...
n_0	Density at which the H_2 ro-vibrational lines start to become optically thick	...	...	...	4	...	...
$Q_{H_{II}}$	Fraction of the volume of the Universe inside bubbles of ionized H	...	...	...	...	...	6
r	Radius or distance	...	...	...	...	...	6
$R_{dest,X}$	Collisional destruction rate per unit volume of species X	...	...	3	...	...	...
$R_{form,X}$	Formation rate per unit volume of species X	...	...	3	...	...	...
r_{max}	Maximum radius of an ionized bubble	...	...	...	...	...	6
$R_{pd,X}$	Photodestruction rate of species X	...	...	3	...	...	...
R_X	Rate per unit time for reaction number X	...	...	3	...	...	...
S	Total electron spin of an atom	...	2	...	...	...	...
S_α	Correction factor	...	...	...	...	5	...
T	Gas temperature	1	...	3	4	...	6
T_b	Brightness temperature	...	...	...	...	5	...
T_{CMB}	CMB temperature	...	...	3	...	5	...
T_e	Electron temperature	...	2	...	...	...	...
T_K	Gas temperature	...	...	...	...	5	...

Table B1 List of Symbols Used, Their Definitions, and the Sections Where They Are Used—cont'd

Symbol	Definition	Sections						
T_R	Brightness temperature of a background source	...	...	...	...	5	...	...
T_r	Black body radiation field temperature	1	...	3	...	...	...	...
T_S	21-cm spin temperature	...	...	...	...	5	...	...
T_{vir}	Virial temperature	...	...	...	4	5	...	...
T_α	Color temperature of the radiation field at the Lyα frequency	...	2	...	...	5	...	...
T_γ	CMB temperature	...	2	...	...	...	...	...
T_0	Present-day CMB temperature	...	2	...	...	...	...	...
$T_\star$	$2\pi\hbar/k_B\lambda_{21\,cm}$	...	...	...	...	5	...	...
t	Time	1	...	...	4	...	6	...
t_C	Compton cooling time	...	...	...	...	...	6	...
$t_{cd,X}$	Time scale for collisional destruction per unit volume of species X	...	...	3	...	...	...	...
t_{cool}	Cooling time	...	...	...	4	...	...	...
$t_{form,X}$	Time scale for formation of species X	...	...	3	...	...	...	...
t_H	Hubble time, i.e., expansion timescale of the Universe	...	...	3	4	...	6	...
$t_{pd,X}$	Time scale for photodestruction of species X	...	...	3	...	...	...	...
t_{rec}	Time scale for recombination	...	...	...	4	...	6	...
u_{CMB}	CMB energy density	...	...	...	...	...	6	...
V	Volume	...	...	...	...	...	6	...
V_p	Proper volume	...	...	...	...	...	6	...
v	Vibrational quantum number	...	...	3	...	...	...	...
v	Velocity	...	...	...	...	...	6	...
v_{RMS}	RMS velocity of streaming motion	...	...	...	4	...	...	...
v_r	Velocity along the line of sight	...	...	...	...	5	...	...

Symbol	Description						
W	Potential energy	$\cdots$	$\cdots$	$\cdots$	4	$\cdots$	$\cdots$
x_c	Coupling coefficient due to atomic collisions	$\cdots$	$\cdots$	$\cdots$	$\cdots$	5	$\cdots$
x_c^i	Collisional coupling coefficient of H with species i	$\cdots$	$\cdots$	$\cdots$	$\cdots$	5	$\cdots$
$x_{e,0}$	Initial value of x_e	$\cdots$	$\cdots$	$\cdots$	4	$\cdots$	$\cdots$
x_i	Filling fraction of ionized bubbles	$\cdots$	$\cdots$	$\cdots$	$\cdots$	5	$\cdots$
x_{tot}	$x_c + x_\alpha$	$\cdots$	$\cdots$	$\cdots$	$\cdots$	5	$\cdots$
x_X	Fractional abundance of X relative to the number density of hydrogen nuclei	$\cdots$	$\cdots$	3	4	5	$\cdots$
x_X	Fractional abundance of ionization stage X relative to all nuclei of that element	$\cdots$	$\cdots$	$\cdots$	$\cdots$	$\cdots$	6
x_α	Coupling coefficient due to scattering of Lyα photons	$\cdots$	$\cdots$	$\cdots$	$\cdots$	5	$\cdots$
Y_p	Helium mass fraction from Big Bang Nucleosynthesis	$\cdots$	2	$\cdots$	$\cdots$	$\cdots$	6
Z	Metallicity	$\cdots$	$\cdots$	$\cdots$	$\cdots$	$\cdots$	6
$Z_\odot$	Solar metallicity	$\cdots$	$\cdots$	$\cdots$	$\cdots$	$\cdots$	6
z	Redshift	1	2	3	4	5	6
z_{em}	Redshift for light emitted at a scale factor of a_{em}	1	2	3	4	5	6
$z_{crit,X}$	z below which photodestruction becomes unimportant for species X	$\cdots$	$\cdots$	3	$\cdots$	$\cdots$	$\cdots$
z_{eq}	Redshift where matter and radiation contribute equally to H	1	$\cdots$	$\cdots$	$\cdots$	$\cdots$	$\cdots$
z_h	Redshift of strong X-ray heating	$\cdots$	$\cdots$	$\cdots$	$\cdots$	5	$\cdots$
z_r	Redshift of reionization	$\cdots$	$\cdots$	$\cdots$	$\cdots$	5	$\cdots$
z_α	Redshift where Lyα coupling saturates	$\cdots$	$\cdots$	$\cdots$	$\cdots$	5	$\cdots$
z_Λ	Redshift where the Universe becomes dominated by the cosmological constant	1	$\cdots$	$\cdots$	$\cdots$	$\cdots$	$\cdots$

Table B1 List of Symbols Used, Their Definitions, and the Sections Where They Are Used—cont'd

Symbol	Definition	Sections						
$z_\star$	Redshift of star formation	...	...	...	...	5	...	...
α	Recombination rate coefficient for H II forming H I	...	...	...	...	...	6	...
α_B	Case–B recombination rate coefficient for H II forming H I	...	...	...	...	...	6	...
α_{nL}	Recombination rate coefficient for H II forming H I in the nL level	...	...	...	...	...	6	...
α_ν	Absorption coefficient per unit length versus ν	...	...	...	...	...	6	...
$\Gamma_{H I}$	Ionization rate of H	...	...	...	...	5	6	...
ΔE	Energy separation between two levels	...	2	...	...	5	...	...
ΔI_ν	Distortion in the CMB intensity with frequency	...	2	...	...	...	...	...
Δl	Change in orbital angular momentum l	...	2	...	...	...	...	7
ΔN_e	Distortion in the number density of free electrons	...	2	...	...	...	...	...
ΔT_0	Variation in the present-day CMB temperature	...	2	...	...	...	...	...
Δt	Timestep	...	...	...	4	...	...	...
Δx	Spatial resolution element	...	...	...	4	...	...	...
Δz	Difference in redshift	...	2	...	...	...	...	...
$\Delta \nu$	Difference in transition frequencies	...	2	...	...	...	...	...
$\Delta \rho_\gamma$	Photon energy density released by recombination for a given element	...	2	...	...	...	...	...
δ	Plane wave perturbation	...	...	...	4	...	...	...
δ_b	Fractional overdensity in baryons	...	...	...	...	5	...	...
δ_c	Critical overdensity, typically taken to be $\delta_c = 1.69$	...	...	...	4	...	...	...
δT_b	Differential brightness temperature	...	...	...	...	5	...	...
ζ	Ionization efficiency	...	...	...	...	5	...	...
η	Baryon-to-photon ratio	1	...	...	...	...	6	...

η	Black hole efficiency for converting accreted rest energy of particles into radiation						6
$\kappa_{10}^{i,\mathrm{H}}$	Collisional de–excitation rate coefficient from singlet to triplet H due to collisions with species i					5	
Λ	Cosmological constant	1					
Λ	Radiative cooling rate						6
Λ_{Comp}	Compton cooling rate						6
$\Lambda_{\mathrm{H_2}}$	Radiative cooling rate per $\mathrm{H_2}$ molecule				4		
$\Lambda_{\mathrm{H_2,X}}$	Radiative cooling rate per $\mathrm{H_2}$ molecule in the optically X regime				4		
λ_{J}	Jeans length				4		
$\lambda_{21\,\mathrm{cm}}$	Wavelength of the H 21–cm transition					5	
μ	Dipole moment			3			
ν	Photon frequency		2			5	
$\nu_{\mathrm{H\,I}}$	Photon frequency corresponding to the ionization potential of H						6
$\nu(z)$	$\delta_{\mathrm{c}}/[D_+(z)\sigma(M)]$				4		6
ν_α	Lyα frequency					5	
ν_{3d1s}	Hydrogen 3d $\to$ 1s transition frequency		2				
$\overline{\rho}_{\mathrm{b}}$	Mean universal baryon mass density						6
ρ_{BH}	Mass density in black holes						6
ρ_{CMB}	CMB energy density	1		3			
ρ_{crit}	Critical density needed to halt the expansion of the Universe						
ρ_{g}	Mass density of the cosmological background gas			3			
ρ_{H}	Proton mass density						6
$\rho_{\mathrm{H\,II}}$	H II density normalized by the mean proton mass density						6

Continued

Table B1 List of Symbols Used, Their Definitions, and the Sections Where They Are Used—cont'd

Symbol	Definition	Sections					
ρ_m	Present-day mean mass density of nonrelativistic matter	1	⋯	⋯	⋯	⋯	⋯
ρ_r	Present-day mean density of relativistic matter and radiation	1	⋯	⋯	⋯	⋯	⋯
ρ_γ	Photon energy density	⋯	2	⋯	⋯	⋯	⋯
$\rho_0(z)$	Mean mass density of matter at a redshift of z	⋯	⋯	⋯	4	⋯	⋯
σ	Photoionization cross section	⋯	⋯	⋯	⋯	5	⋯
$\sigma(M)$	Standard deviation of the fluctuations in the linear density field	⋯	⋯	⋯	4	⋯	⋯
σ_{HI}	Photoionization cross section of H	⋯	⋯	⋯	⋯	⋯	6
σ_{nL}	Recombination cross section into the nL level of H	⋯	⋯	⋯	⋯	⋯	6
σ_T	Thomson cross section	⋯	⋯	⋯	⋯	⋯	6
σ_{1sc}	H I 1s photoionization cross section	⋯	⋯	⋯	⋯	5	⋯
τ	Optical depth	⋯	2	⋯	⋯	5	⋯
τ_ν	Optical depth at frequency ν	⋯	⋯	⋯	⋯	⋯	6
ϕ	Line shape function	⋯	2	⋯	⋯	⋯	⋯
$\chi_{He\,II}$	Ionization potential of hydrogenic helium	⋯	2	2	⋯	⋯	⋯
Ω_b	Present-day mean baryonic density of the Universe relative to ρ_{crit}	1	2	⋯	4	5	6
Ω_m	Present-day mean matter density normalized to ρ_{crit}	1	⋯	⋯	4	5	6
Ω_r	Present-day mean density of relativistic matter and radiation normalized to ρ_{crit}	1	⋯	⋯	⋯	⋯	⋯
$\Omega_{r,neutrinos}$	Contribution to Ω_r by neutrinos	1	⋯	⋯	⋯	⋯	⋯
$\Omega_{r,photons}$	Contribution to Ω_r by photons	1	⋯	⋯	⋯	⋯	⋯
Ω_{tot}	Total density of the Universe relative to ρ_{crit}	⋯	2	⋯	⋯	⋯	⋯
Ω_Λ	Present-day vacuum energy density relative to ρ_{crit}	1	⋯	⋯	⋯	⋯	⋯

REFERENCES

Abazajian, K. N., Arnold, K., Austermann, J., Benson, B. A., Bischoff, C., Bock, J., Bond, J. R., Borrill, J., Calabrese, E., Carlstrom, J. E., Carvalho, C. S., Chang, C. L., Chiang, H. C., Church, S., Cooray, A., Crawford, T. M., Dawson, K. S., Das, S., Devlin, M. J., Dobbs, M., Dodelson, S., Dore, O., Dunkley, J., Errard, J., Fraisse, A., Gallicchio, J., Halverson, N. W., Hanany, S., Hildebrandt, S. R., Hincks, A., Hlozek, R., Holder, G., Holzapfel, W. L., Honscheid, K., Hu, W., Hubmayr, J., Irwin, K., Jones, W. C., Kamionkowski, M., Keating, B., Keisler, R., Knox, L., Komatsu, E., Kovac, J., Kuo, C.-L., Lawrence, C., Lee, A. T., Leitch, E., Linder, E., Lubin, P., McMahon, J., Miller, A., Newburgh, L., Niemack, M. D., Nguyen, H., Nguyen, H. T., Page, L., Pryke, C., Reichardt, C. L., Ruhl, J. E., Sehgal, N., Seljak, U., Sievers, J., Silverstein, E., Slosar, A., Smith, K. M., Spergel, D., Staggs, S. T., Stark, A., Stompor, R., Vieregg, A. G., Wang, G., Watson, S., Wollack, E. J., Wu, W. L. K., Yoon, K. W., Zahn, O., Sep. 2013. Neutrino physics from the cosmic microwave background and large scale structure. ArXiv e-prints 1309.5383.

Abel, T., Anninos, P., Zhang, Y., Norman, M. L., Aug. 1997. Modeling primordial gas in numerical cosmology. New Astron. 2, 181–207.

Abel, T., Bryan, G. L., Norman, M. L., Jan. 2002. The formation of the first star in the universe. Science 295, 93–98.

Aldrovandi, S. M. V., Pequignot, D., May 1973. Radiative and dielectronic recombination coefficients for complex ions. Astron. Astrophys. 25, 137–140.

Ali-Haïmoud, Y., Jan. 2013. Effective conductance method for the primordial recombination spectrum. Phys. Rev. D 87 (2), 023526.

Ali-Haïmoud, Y., Hirata, C. M., Sep. 2010. Ultrafast effective multilevel atom method for primordial hydrogen recombination. Phys. Rev. D 82 (6), 063521.

Ali-Haïmoud, Y., Hirata, C. M., Feb. 2011. HyRec: a fast and highly accurate primordial hydrogen and helium recombination code. Phys. Rev. D 83 (4), 043513.

Ali-Haïmoud, Y., Grin, D., Hirata, C. M., Dec. 2010. Radiative transfer effects in primordial hydrogen recombination. Phys. Rev. D 82 (12), 123502.

Ali-Haïmoud, Y., Hirata, C. M., Kamionkowski, M., Apr. 2011. Metals at the surface of last scatter. Phys. Rev. D 83 (8), 083508.

Alizadeh, E., Hirata, C. M., Oct. 2011. Molecular hydrogen in the cosmic recombination epoch. Phys. Rev. D 84, 083011.

Allison, A. C., Dalgarno, A., Oct. 1969. Spin change in collisions of hydrogen atoms. Astrophys. J. 158, 423–425.

Alvarez, M. A., Pen, U.-L., Chang, T.-C., Nov. 2010. Enhanced detectability of pre-reionization 21 cm structure. Astrophys. J. Lett. 723, L17–L21.

André, P., Baccigalupi, C., Banday, A., Barbosa, D., Barreiro, B., Bartlett, J., Bartolo, N., Battistelli, E., Battye, R., Bendo, G., Benoît, A., Bernard, J.-P., Bersanelli, M., Béthermin, M., Bielewicz, P., Bonaldi, A., Bouchet, F., Boulanger, F., Brand, J., Bucher, M., Burigana, C., Cai, Z.-Y., Camus, P., Casas, F., Casasola, V., Castex, G., Challinor, A., Chluba, J., Chon, G., Colafrancesco, S., Comis, B., Cuttaia, F., D'Alessandro, G., Da Silva, A., Davis, R., de Avillez, M., de Bernardis, P., de Petris, M., de Rosa, A., de Zotti, G., Delabrouille, J., Désert, F.-X., Dickinson, C., Diego, J. M., Dunkley, J., Enßlin, T., Errard, J., Falgarone, E., Ferreira, P., Ferrière, K., Finelli, F., Fletcher, A., Fosalba, P., Fuller, G., Galli, S., Ganga, K., García-Bellido, J., Ghribi, A., Giard, M., Giraud-Héraud, Y., Gonzalez-Nuevo, J., Grainge, K., Gruppuso, A., Hall, A., Hamilton, J.-C., Haverkorn, M., Hernandez-Monteagudo, C., Herranz, D., Jackson, M., Jaffe, A., Khatri, R., Kunz, M., Lamagna, L., Lattanzi, M., Leahy, P., Lesgourgues, J., Liguori, M., Liuzzo, E., Lopez-Caniego, M., Macias-Perez, J., Maffei, B., Maino, D., Mangilli, A., Martinez-Gonzalez, E., Martins, C., Masi, S., Massardi, M., Matarrese, S.,

Melchiorri, A., Melin, J.-B., Mennella, A., Mignano, A., Miville-Deschênes, M.-A., Monfardini, A., Murphy, A., Naselsky, P., Nati, F., Natoli, P., Negrello, M., Noviello, F., O'Sullivan, C., Paci, F., Pagano, L., Paladino, R., Palanque-Delabrouille, N., Paoletti, D., Peiris, H., Perrotta, F., Piacentini, F., Piat, M., Piccirillo, L., Pisano, G., Polenta, G., Pollo, A., Ponthieu, N., Remazeilles, M., Ricciardi, S., Roman, M., Rosset, C., Rubino-Martin, J.-A., Salatino, M., Schillaci, A., Shellard, P., Silk, J., Starobinsky, A., Stompor, R., Sunyaev, R., Tartari, A., Terenzi, L., Toffolatti, L., Tomasi, M., Trappe, N., Tristram, M., Trombetti, T., Tucci, M., Van de Weijgaert, R., Van Tent, B., Verde, L., Vielva, P., Wandelt, B., Watson, R., Withington, S., Feb. 2014. PRISM (Polarized Radiation Imaging and Spectroscopy Mission): an extended white paper. J. Cosmol. Astropart. Phys. 2, 6.

Bagla, J. S., Loeb, A., May 2009. The hyperfine transition of $^3He^+$ as a probe of the intergalactic medium. ArXiv e-prints 0905.1698.

Barkana, R., Loeb, A., Jul. 2001. In the beginning: the first sources of light and the reionization of the universe. Phys. Rep. 349, 125–238.

Barkana, R., Loeb, A., Jul. 2004. Unusually large fluctuations in the statistics of galaxy formation at high redshift. Astrophys. J. 609, 474–481.

Barkana, R., Loeb, A., May 2005a. A method for separating the physics from the astrophysics of high-redshift 21 centimeter fluctuations. Astrophys. J. Lett. 624, L65–L68.

Barkana, R., Loeb, A., Jun. 2005b. Detecting the earliest galaxies through two new sources of 21 centimeter fluctuations. Astrophys. J. 626, 1–11.

Barkana, R., Loeb, A., Oct. 2005c. Probing the epoch of early baryonic infall through 21-cm fluctuations. Mon. Not. R. Astron. Soc. 363, L36–L40.

Bate, M. R., Bonnell, I. A., Price, N. M., Nov. 1995. Modelling accretion in protobinary systems. Mon. Not. R. Astron. Soc. 277, 362–376.

Belikov, A. V., Hooper, D., Aug. 2009. How dark matter reionized the universe. Phys. Rev. D 80 (3), 035007.

Bennett, C. L., Halpern, M., Hinshaw, G., Jarosik, N., Kogut, A., Limon, M., Meyer, S. S., Page, L., Spergel, D. N., Tucker, G. S., Wollack, E., Wright, E. L., Barnes, C., Greason, M. R., Hill, R. S., Komatsu, E., Nolta, M. R., Odegard, N., Peiris, H. V., Verde, L., Sep. 2003a. First-year Wilkinson Microwave Anisotropy Probe (WMAP) observations: preliminary maps and basic results. Astrophys. J. Suppl. Ser. 148, 1–27.

Bennett, O. J., Dickinson, A. S., Leininger, T., Gadéa, F. X., May 2003b. Radiative association in Li+H revisited: the role of quasi-bound states. Mon. Not. R. Astron. Soc. 341, 361–368.

Benoît, A., Ade, P., Amblard, A., Ansari, R., Aubourg, É., Bargot, S., Bartlett, J. G., Bernard, J.-P., Bhatia, R. S., Blanchard, A., Bock, J. J., Boscaleri, A., Bouchet, F. R., Bourrachot, A., Mar. 2003. Cosmological constraints from Archeops. Astron. Astrophys. 399, L25–L30.

Bharadwaj, S., Ali, S. S., Jul. 2004. The cosmic microwave background radiation fluctuations from H I PERTURBATIONS PRIOR TO REIONIZATION. Mon. Not. R. Astron. Soc. 352, 142–146.

Black, J. H., Nov. 1981. The physical state of primordial intergalactic clouds. Mon. Not. R. Astron. Soc. 197, 553–563.

Bond, J. R., Cole, S., Efstathiou, G., Kaiser, N., Oct. 1991. Excursion set mass functions for hierarchical Gaussian fluctuations. Astrophys. J. 379, 440–460.

Bougleux, E., Galli, D., Jul. 1997. Lithium hydride in the early universe and in protogalactic clouds. Mon. Not. R. Astron. Soc. 288, 638–648.

Boutsia, K., Grazian, A., Giallongo, E., Fontana, A., Pentericci, L., Castellano, M., Zamorani, G., Mignoli, M., Vanzella, E., Fiore, F., Lilly, S. J., Gallozzi, S., Testa, V., Paris, D., Santini, P., Jul. 2011. A low escape fraction of ionizing photons of $L > L^*$ Lyman break galaxies at $z = 3.3$. Astrophys. J. 736, 41.

Bouwens, R. J., Illingworth, G. D., González, V., Labbé, I., Franx, M., Conselice, C. J., Blakeslee, J., van Dokkum, P., Holden, B., Magee, D., Marchesini, D., Zheng, W., Dec. 2010a. $z \sim 7$ Galaxy candidates from NICMOS observations over the HDF-South and the CDF-South and HDF-North goods fields. Astrophys. J. 725, 1587–1599.

Bouwens, R. J., Illingworth, G. D., Oesch, P. A., Stiavelli, M., van Dokkum, P., Trenti, M., Magee, D., Labbé, I., Franx, M., Carollo, C. M., Gonzalez, V., Feb. 2010b. Discovery of $z \sim 8$ galaxies in the Hubble ultra deep field from ultra-deep WFC3/IR observations. Astrophys. J. Lett. 709, L133–L137.

Bovino, S., Tacconi, M., Gianturco, F. A., Oct. 2011a. Photon–induced evolutionary rates of LiHe$^+$ ($^1\Sigma^+$) in early universe from accurate quantum computations. Astrophys. J. 740, 101.

Bovino, S., Tacconi, M., Gianturco, F. A., Galli, D., May 2011b. Ion chemistry in the early universe. Revisiting the role of HeH$^+$ with new quantum calculations. Astron. Astrophys. 529, A140.

Bovino, S., Tacconi, M., Gianturco, F. A., Galli, D., Palla, F., Apr. 2011c. On the relative abundance of LiH and LiH$^+$ molecules in the early universe: new results from quantum reactions. Astrophys. J. 731, 107.

Bovino, S., Schleicher, D. R. G., Grassi, T., Jul. 2013. Primordial star formation: relative impact of H2 three-body rates and initial conditions. Astron. Astrophys. 561, 13.

Bowman, J. D., Rogers, A. E. E., Dec. 2010. A lower limit of $\Delta z \gtrsim 0.06$ for the duration of the reionization epoch. Nature 468, 796–798.

Brandenberger, R. H., Danos, R. J., Hernández, O. F., Holder, G. P., Dec. 2010. The 21 cm signature of cosmic string wakes. J. Cosmol. Astropart. Phys. 12, 28.

Bray, I., Fursa, D. V., Kheifets, A. S., Stelbovics, A. T., Aug. 2002. Electrons and photons colliding with atoms: development and application of the convergent close-coupling method. J. Phys. B 35, R117–R146.

Bromm, V., Nov. 2013. Formation of the first stars. Rep. Prog. Phys. 76 (11), 112901.

Bromm, V., Yoshida, N., Sep. 2011. The first galaxies. Annu. Rev. Astron. Astrophys. 49, 373–407.

Bromm, V., Kudritzki, R. P., Loeb, A., May 2001. Generic spectrum and ionization efficiency of a heavy initial mass function for the first stars. Astrophys. J. 552, 464–472.

Bromm, V., Coppi, P. S., Larson, R. B., Jan. 2002. The formation of the first stars. I. The primordial star-forming cloud. Astrophys. J. 564, 23–51.

Calabrese, E., Hlozek, R. A., Battaglia, N., Battistelli, E. S., Bond, J. R., Chluba, J., Crichton, D., Das, S., Devlin, M. J., Dunkley, J., Dünner, R., Farhang, M., Gralla, M. B., Hajian, A., Halpern, M., Hasselfield, M., Hincks, A. D., Irwin, K. D., Kosowsky, A., Louis, T., Marriage, T. A., Moodley, K., Newburgh, L., Niemack, M. D., Nolta, M. R., Page, L. A., Sehgal, N., Sherwin, B. D., Sievers, J. L., Sifón, C., Spergel, D. N., Staggs, S. T., Switzer, E. R., Wollack, E. J., May 2013. Cosmological parameters from pre-Planck cosmic microwave background measurements. Phys. Rev. D 87 (10), 103012.

Cantalupo, S., Porciani, C., Lilly, S. J., Jan. 2008. Mapping neutral hydrogen during reionization with the Lyα emission from quasar ionization fronts. Astrophys. J. 672, 48–58.

Carilli, C. L., Gnedin, N. Y., Owen, F., Sep. 2002. H I 21 centimeter absorption beyond the epoch of reionization. Astrophys. J. 577, 22–30.

Carlberg, R. G., Yee, H. K. C., Ellingson, E., Abraham, R., Gravel, P., Morris, S., Pritchet, C. J., May 1996. Galaxy cluster virial masses and omega. Astrophys. J. 462, 32.

Carlberg, R. G., Yee, H. K. C., Ellingson, E., Mar. 1997. The average mass and light profiles of galaxy clusters. Astrophys. J. 478, 462.

Chen, X., Kamionkowski, M., Aug. 2004. Particle decays during the cosmic dark ages. Phys. Rev. D 70 (4), 043502.

Chen, X., Miralda-Escudé, J., Feb. 2004. The spin-kinetic temperature coupling and the heating rate due to Lyα scattering before reionization: predictions for 21 centimeter emission and absorption. Astrophys. J. 602, 1–11.

Chen, X., Miralda-Escudé, J., Sep. 2008. The 21 cm signature of the first stars. Astrophys. J. 684, 18–33.

Chluba, J., Feb. 2010. Could the cosmological recombination spectrum help us understand annihilating dark matter? Mon. Not. R. Astron. Soc. 402, 1195–1207.

Chluba, J., Sunyaev, R. A., Nov. 2006a. Free-bound emission from cosmological hydrogen recombination. Astron. Astrophys. 458, L29–L32.

Chluba, J., Sunyaev, R. A., Jan. 2006b. Induced two-photon decay of the 2s level and the rate of cosmological hydrogen recombination. Astron. Astrophys. 446, 39–42.

Chluba, J., Sunyaev, R. A., Nov. 2007. Cosmological hydrogen recombination: Lyn line feedback and continuum escape. Astron. Astrophys. 475, 109–114.

Chluba, J., Sunyaev, R. A., Feb. 2008a. Is there a need and another way to measure the cosmic microwave background temperature more accurately? Astron. Astrophys. 478, L27–L30.

Chluba, J., Sunyaev, R. A., Mar. 2008b. Two-photon transitions in hydrogen and cosmological recombination. Astron. Astrophys. 480, 629–645.

Chluba, J., Sunyaev, R. A., Aug. 2009a. Cosmological hydrogen recombination: influence of resonance and electron scattering. Astron. Astrophys. 503, 345–355.

Chluba, J., Sunyaev, R. A., Jul. 2009b. Pre-recombinational energy release and narrow features in the CMB spectrum. Astron. Astrophys. 501, 29–47.

Chluba, J., Sunyaev, R. A., Mar. 2009c. Time-dependent corrections to the Lyα escape probability during cosmological recombination. Astron. Astrophys. 496, 619–635.

Chluba, J., Sunyaev, R. A., Feb. 2010a. Cosmological recombination: feedback of helium photons and its effect on the recombination spectrum. Mon. Not. R. Astron. Soc. 402, 1221–1248.

Chluba, J., Sunyaev, R. A., Mar. 2010b. Lyα escape during cosmological hydrogen recombination: the 3d-1s and 3s-1s two-photon processes. Astron. Astrophys. 512, A53.

Chluba, J., Sunyaev, R. A., Jan. 2012. The evolution of CMB spectral distortions in the early universe. Mon. Not. R. Astron. Soc. 419, 1294–1314.

Chluba, J., Thomas, R. M., Apr. 2011. Towards a complete treatment of the cosmological recombination problem. Mon. Not. R. Astron. Soc. 412, 748–764.

Chluba, J., Rubiño-Martín, J. A., Sunyaev, R. A., Feb. 2007. Cosmological hydrogen recombination: populations of the high-level substates. Mon. Not. R. Astron. Soc. 374, 1310–1320.

Chluba, J., Vasil, G. M., Dursi, L. J., Sep. 2010. Recombinations to the Rydberg states of hydrogen and their effect during the cosmological recombination epoch. Mon. Not. R. Astron. Soc. 407, 599–612.

Chluba, J., Fung, J., Switzer, E. R., Jul. 2012. Radiative transfer effects during primordial helium recombination. Mon. Not. R. Astron. Soc. 423, 3227–3242.

Choudhury, T. R., Haehnelt, M. G., Regan, J., Apr. 2009. Inside-out or outside-in: the topology of reionization in the photon-starved regime suggested by Lyα forest data. Mon. Not. R. Astron. Soc. 394, 960–977.

Chuzhoy, L., Shapiro, P. R., Feb. 2007. Heating and cooling of the early intergalactic medium by resonance photons. Astrophys. J. 655, 843–846.

Chuzhoy, L., Zheng, Z., Dec. 2007. Radiative transfer effect on ultraviolet pumping of the 21 cm line in the high-redshift universe. Astrophys. J. 670, 912–918.

Chuzhoy, L., Alvarez, M. A., Shapiro, P. R., Sep. 2006. Recognizing the first radiation sources through their 21 cm signature. Astrophys. J. Lett. 648, L1–L4.

Ciardi, B., Salvaterra, R., Di Matteo, T., Feb. 2010. Lyα versus X-ray heating in the high-zsD intergalactic medium. Mon. Not. R. Astron. Soc. 401, 2635–2640.

Clark, P. C., Glover, S. C. O., Smith, R. J., Greif, T. H., Klessen, R. S., Bromm, V., Feb. 2011. The formation and fragmentation of disks around primordial protostars. Science 331, 1040–1042.

Coppola, C. M., Longo, S., Capitelli, M., Palla, F., Galli, D., Mar. 2011. Vibrational level population of H_2 and H_2^+ in the early universe. Astrophys. J. Suppl. Ser. 193, 7.

Crill, B. P., Ade, P. A. R., Battistelli, E. S., Benton, S., Bihary, R., Bock, J. J., Bond, J. R., Brevik, J., Bryan, S., Contaldi, C. R., Doré, O., Farhang, M., Fissel, L., Golwala, S. R., Halpern, M., Hilton, G., Holmes, W., Hristov, V. V., Irwin, K., Jones, W. C., Kuo, C. L., Lange, A. E., Lawrie, C., MacTavish, C. J., Martin, T. G., Mason, P., Montroy, T. E., Netterfield, C. B., Pascale, E., Riley, D., Ruhl, J. E., Runyan, M. C., Trangsrud, A., Tucker, C., Turner, A., Viero, M., Wiebe, D., Aug. 2008. SPIDER: a balloon-borne large-scale CMB polarimeter. Proc. SPIE 7010, 70102P.

Cyburt, R. H., Fields, B. D., Olive, K. A., Aug. 2003. Primordial nucleosynthesis in light of WMAP. Phys. Lett. B 567, 227–234.

Cyburt, R. H., Fields, B. D., Olive, K. A., Nov. 2008. An update on the Big Bang nucleosynthesis prediction for ^{7}Li: the problem worsens. J. Cosmol. Astropart. Phys. 11, 12.

Dalgarno, A., Kirby, K., Stancil, P. C., Feb. 1996. The radiative association of Li^+ and H, Li and H^+, and Li and H. Astrophys. J. 458, 397–400.

Dalgarno, A., Yan, M., Liu, W., Nov. 1999. Electron energy deposition in a gas mixture of atomic and molecular hydrogen and helium. Astrophys. J. Suppl. Ser. 125, 237–256.

Das, S., Marriage, T. A., Ade, P. A. R., Aguirre, P., Amiri, M., Appel, J. W., Barrientos, L. F., Battistelli, E. S., Bond, J. R., Brown, B., Burger, B., Chervenak, J., Devlin, M. J., Dicker, S. R., Bertrand Doriese, Mar. 2011. The Atacama Cosmology Telescope: a measurement of the cosmic microwave background power spectrum at 148 and 218 GHz from the 2008 southern survey. Astrophys. J. 729, 62.

Defazio, P., Petrongolo, C., Gamallo, P., González, M., Jun. 2005. Product distributions, rate constants, and mechanisms of LiH+H reactions. J. Chem. Phys. 122 (21), 214303.

Dickinson, A. S., Dec. 2005. Radiative association of H and D. J. Phys. B 38, 4329–4334.

Dijkstra, M., Haiman, Z., Loeb, A., Oct. 2004a. A limit from the X-ray background on the contribution of quasars to reionization. Astrophys. J. 613, 646–654.

Dijkstra, M., Haiman, Z., Rees, M. J., Weinberg, D. H., Feb. 2004b. Photoionization feedback in low-mass galaxies at high redshift. Astrophys. J. 601, 666–675.

Dodelson, S., 2003. Modern cosmology.

Drake, G. W. F., 2006. Springer Handbook of Atomic, Molecular, and Optical Physics. Springer, Berlin.

Drake, G. W. F., Morton, D. C., May 2007. A multiplet table for neutral helium (^{4}He I) with transition rates. Astrophys. J. Suppl. Ser. 170, 251–260.

Dubrovich, V. K., Oct. 1975. Hydrogen recombination lines of cosmological origin. Sov. Astron. Lett. 1, 196.

Dubrovich, V. K., Grachev, S. I., Jun. 2005. Recombination dynamics of primordial hydrogen and helium (He I) in the universe. Astron. Lett. 31, 359–364.

Dunkley, J., Hlozek, R., Sievers, J., Acquaviva, V., Ade, P. A. R., Aguirre, P., Amiri, M., Appel, J. W., Barrientos, L. F., Battistelli, E. S., Bond, J. R., Brown, B., Burger, B., Chervenak, J., Das, S., Devlin, M. J., Dicker, S. R., Bertrand Doriese, W., Dünner, R., Essinger-Hileman, T., Fisher, R. P., Fowler, J. W., Hajian, A., Halpern, M., Hasselfield, M., Hernández-Monteagudo, C., Hilton, G. C., Hilton, M., Hincks, A. D., Huffenberger, K. M., Hughes, D. H., Hughes, J. P., Infante, L., Irwin, K. D., Juin, J. B., Kaul, M., Klein, J., Kosowsky, A., Lau, J. M., Limon, M., Lin, Y.-T., Lupton, R. H., Marriage, T. A., Marsden, D., Mauskopf, P., Menanteau, F., Moodley, K., Moseley, H., Netterfield, C. B., Niemack, M. D., Nolta, M. R., Page, L. A., Parker, L., Partridge, B., Reid, B., Sehgal, N., Sherwin, B., Spergel, D. N., Staggs, S. T., Swetz, D. S.,

Switzer, E. R., Thornton, R., Trac, H., Tucker, C., Warne, R., Wollack, E., Zhao, Y., Sep. 2011. The Atacama Cosmology Telescope: cosmological parameters from the 2008 power spectrum. Astrophys. J. 739, 52.

Efstathiou, G., May 1992. Suppressing the formation of dwarf galaxies via photoionization. Mon. Not. R. Astron. Soc. 256, 43–47. http://adsabs.harvard.edu/cgi-bin/nph-bib_query?bibcode=1992MNRAS.256P..43E&db_key=AST

Ewen, H. I., Purcell, E. M., Sep. 1951. Observation of a line in the galactic radio spectrum: radiation from galactic hydrogen at 1,420 Mc./sec. Nature 168, 356.

Fan, X., Hennawi, J. F., Richards, G. T., Strauss, M. A., Schneider, D. P., Donley, J. L., Young, J. E., Annis, J., Lin, H., Lampeitl, H., Lupton, R. H., Gunn, J. E., Knapp, G. R., Brandt, W. N., Anderson, S., Bahcall, N. A., Brinkmann, J., Brunner, R. J., Fukugita, M., Szalay, A. S., Szokoly, G. P., York, D. G., Aug. 2004. A survey of $z > 5.7$ quasars in the Sloan Digital Sky Survey. III. Discovery of five additional quasars. Astron. J. 128, 515–522.

Fan, X., Carilli, C. L., Keating, B., Sep. 2006. Observational constraints on cosmic reionization. Annu. Rev. Astron. Astrophys. 44, 415–462.

Fendt, W. A., Chluba, J., Rubiño-Martín, J. A., Wandelt, B. D., Apr. 2009. RICO: a new approach for fast and accurate representation of the cosmological recombination history. Astrophys. J. Suppl. Ser. 181, 627–638.

Ferland, G. J., Peterson, B. M., Horne, K., Welsh, W. F., Nahar, S. N., Mar. 1992. Anisotropic line emission and the geometry of the broad-line region in active galactic nuclei. Astrophys. J. 387, 95–108.

Fernandez, E. R., Komatsu, E., Iliev, I. T., Shapiro, P. R., Feb. 2010. The cosmic near-infrared background. II. Fluctuations. Astrophys. J. 710, 1089–1110.

Field, G. B., 1958. Excitation of the hydrogen 21cm line. Proc. Inst. Radio Eng. 46, 240–250.

Field, G. B., May 1959. The time relaxation of a resonance-line profile. Astrophys. J. 129, 551–564.

Finkbeiner, D. P., Padmanabhan, N., Weiner, N., Sep. 2008. CMB and 21-cm signals for dark matter with a long-lived excited state. Phys. Rev. D 78 (6), 063530.

Fixsen, D. J., Mather, J. C., Dec. 2002. The spectral results of the far-infrared absolute spectrophotometer instrument on COBE. Astrophys. J. 581, 817–822.

Fixsen, D. J., Kogut, A., Levin, S., Limon, M., Lubin, P., Mirel, P., Seiffert, M., Singal, J., Wollack, E., Villela, T., Wuensche, C. A., Jun. 2011. ARCADE 2 measurement of the absolute sky brightness at 3-90 GHz. Astrophys. J. 734, 5.

Forrey, R. C., Aug. 2013. Rate of formation of hydrogen molecules by three-body recombination during primordial star formation. Astrophys. J. Lett. 773, L25.

Frommhold, L., 1993. Collision-Induced Absorption in Gases. Cambridge University Press, Cambridge.

Fukugita, M., Peebles, P. J. E., Dec. 2004. The cosmic energy inventory. Astrophys. J. 616, 643–668.

Furlanetto, S. R., Sep. 2006. The global 21-centimeter background from high redshifts. Mon. Not. R. Astron. Soc. 371, 867–878.

Furlanetto, S. R., Furlanetto, M. R., Jan. 2007a. Spin-exchange rates in electron-hydrogen collisions. Mon. Not. R. Astron. Soc. 374, 547–555.

Furlanetto, S. R., Furlanetto, M. R., Jul. 2007b. Spin exchange rates in proton-hydrogen collisions. Mon. Not. R. Astron. Soc. 379, 130–134.

Furlanetto, S. R., Johnson Stoever, S., Jun. 2010. Secondary ionization and heating by fast electrons. Mon. Not. R. Astron. Soc. 404, 1869–1878.

Furlanetto, S. R., Loeb, A., Nov. 2002. The 21 centimeter forest: radio absorption spectra as probes of minihalos before reionization. Astrophys. J. 579, 1–9.

Furlanetto, S. R., Loeb, A., Aug. 2004. Large-scale structure shocks at low and high redshifts. Astrophys. J. 611, 642–654.

Furlanetto, S. R., Oh, S. P., Nov. 2005. Taxing the rich: recombinations and bubble growth during reionization. Mon. Not. R. Astron. Soc. 363, 1031–1048.

Furlanetto, S. R., Oh, S. P., Dec. 2006. Redshifted 21 cm emission from minihalos before reionization. Astrophys. J. 652, 849–856.

Furlanetto, S. R., Oh, S. P., Jul. 2008. The history and morphology of helium reionization. Astrophys. J. 681, 1–17.

Furlanetto, S. R., Pritchard, J. R., Nov. 2006. The scattering of Lyman-series photons in the intergalactic medium. Mon. Not. R. Astron. Soc. 372, 1093–1103.

Furlanetto, S. R., Stoever, S. J., Jun. 2010. Secondary ionization and heating by fast electrons. Mon. Not. R. Astron. Soc. 404, 1869–1878.

Furlanetto, S. R., Zaldarriaga, M., Hernquist, L., Sep. 2004. The growth of H II regions during reionization. Astrophys. J. 613, 1–15.

Furlanetto, S. R., McQuinn, M., Hernquist, L., 2006a. Characteristic scales during reionization. Mon. Not. R. Astron. Soc. 365, 115–126.

Furlanetto, S. R., Oh, S. P., Briggs, F. H., Oct. 2006b. Cosmology at low frequencies: the 21 cm transition and the high-redshift universe. Phys. Rep. 433, 181–301.

Furlanetto, S. R., Oh, S. P., Pierpaoli, E., Nov. 2006c. Effects of dark matter decay and annihilation on the high-redshift 21cm background. Phys. Rev. D 74 (10), 103502.

Galli, D., Palla, F., Jul. 1998. The chemistry of the early universe. Astron. Astrophys. 335, 403–420.

Galli, D., Palla, F., Oct. 2002. Deuterium chemistry in the primordial gas. Planet. Space Sci. 50, 1197–1204.

Galli, D., Palla, F., Aug. 2013. The dawn of chemistry. Annu. Rev. Astron. Astrophys. 51, 163–206.

Geil, P. M., Wyithe, J. S. B., Nov. 2009. Modification of the 21-cm power spectrum by quasars during the epoch of reionization. Mon. Not. R. Astron. Soc. 399, 1877–1887.

Gerlich, D., Horning, S., Nov. 1992. Experimental investigation of radiative association processes as related to interstellar chemistry. Chem. Rev. 92, 1509–1539.

Gianturco, F. A., Gori Giorgi, P., Nov. 1996. Radiative association of LiH($X^1\Sigma^+$) from electronically excited lithium atoms. Phys. Rev. A 54, 4073–4077.

Gianturco, F. A., Gori Giorgi, P., Apr. 1997. Radiative association rates and structure of resonances for Li and Li^+ colliding with H and H^+. Astrophys. J. 479, 560–567.

Giovanardi, C., Palla, F., Feb. 1989. Revision and extension to low temperature of numerical estimates of the electron collisional rates for atomic hydrogen. Astron. Astrophys. Suppl. Ser. 77, 157–160.

Giovanardi, C., Natta, A., Palla, F., Aug. 1987. Numerical fits to the electron impact transition rate coefficients for atomic hydrogen as a function of electron temperature. Astron. Astrophys. Suppl. Ser. 70, 269–280.

Glover, S., Mar. 2008. Chemistry and cooling in metal-free and metal-poor gas. In: O'Shea, B. W., Heger, A. (Eds.), First Stars III, American Institute of Physics, Melville, pp. 25–29.

Glover, S., 2013. The first stars. In: Wiklind, T., Mobasher, B., Bromm, V. (Eds.), Astrophysics and Space Science Library, vol. 396, p. 103.

Glover, S. C. O., Abel, T., 2008. Uncertainties in H_2 and HD chemistry and cooling and their role in early structure formation. Mon. Not. R. Astron. Soc. 388, 1627–1651.

Glover, S. C. O., Brand, P. W. J. L., Mar. 2003. Radiative feedback from an early X-ray background. Mon. Not. R. Astron. Soc. 340, 210–226.

Glover, S., Savin, D. W., Nov. 2006. H_3^+ cooling in primordial gas. Philos. Trans. R. Soc. Lond. Ser. A 364, 3107–3112.

Glover, S. C. O., Savin, D. W., Mar. 2009. Is H_3^+ cooling ever important in primordial gas? Mon. Not. R. Astron. Soc. 393, 911–948.

Gnedin, N. Y., Kravtsov, A. V., Chen, H.-W., Jan. 2008. Escape of ionizing radiation from high-redshift galaxies. Astrophys. J. 672, 765–775.

Goldenberg, H. M., Kleppner, D., Ramsey, N. F., Oct 1960. Atomic hydrogen maser. Phys. Rev. Lett. 5 (8), 361–362.

Göppert-Mayer, M., 1931. Über Elementarakte mit zwei Quantensprüngen. Ann. Phys. 9, 273.

Grachev, S. I., Dubrovich, V. K., Jul. 2008. Primordial hydrogen recombination dynamics with recoil upon scattering in the Ly-α line. Astron. Lett. 34, 439–444.

Green, A. M., Hofmann, S., Schwarz, D. J., Aug. 2005. The first WIMPy halos. J. Cosmol. Astropart. Phys. 8, 3.

Greif, T. H., Johnson, J. L., Klessen, R. S., Bromm, V., Jul. 2008. The first galaxies: assembly, cooling and the onset of turbulence. Mon. Not. R. Astron. Soc. 387, 1021–1036.

Greif, T. H., Springel, V., White, S. D. M., Glover, S. C. O., Clark, P. C., Smith, R. J., Klessen, R. S., Bromm, V., Aug. 2011. Simulations on a moving mesh: the clustered formation of population III protostars. Astrophys. J. 737, 75.

Greif, T. H., Bromm, V., Clark, P. C., Glover, S. C. O., Smith, R. J., Klessen, R. S., Yoshida, N., Springel, V., Jul. 2012. Formation and evolution of primordial protostellar systems. Mon. Not. R. Astron. Soc. 424, 399–415.

Grin, D., Hirata, C. M., Apr. 2010. Cosmological hydrogen recombination: the effect of extremely high-n states. Phys. Rev. D 81 (8), 083005.

Gültekin, K., Richstone, D. O., Gebhardt, K., Lauer, T. R., Tremaine, S., Aller, M. C., Bender, R., Dressler, A., Faber, S. M., Filippenko, A. V., Green, R., Ho, L. C., Kormendy, J., Magorrian, J., Pinkney, J., Siopis, C., Jun. 2009. The $M - \sigma$ and $M - L$ relations in galactic bulges, and determinations of their intrinsic scatter. Astrophys. J. 698, 198–221.

Hajian, A., Acquaviva, V., Ade, P. A. R., Aguirre, P., Amiri, M., Appel, J. W., Barrientos, L. F., Battistelli, E. S., Bond, J. R., Brown, B., Burger, B., Chervenak, J., Das, S., Devlin, M. J., Dicker, S. R., Bertrand Doriese, W., Dunkley, J., Dünner, R., Essinger-Hileman, T., Fisher, R. P., Fowler, J. W., Halpern, M., Hasselfield, M., Hernández-Monteagudo, C., Hilton, G. C., Hilton, M., Hincks, A. D., Hlozek, R., Huffenberger, K. M., Hughes, D. H., Hughes, J. P., Infante, L., Irwin, K. D., Baptiste Juin, J., Kaul, M., Klein, J., Kosowsky, A., Lau, J. M., Limon, M., Lin, Y.-T., Lupton, R. H., Marriage, T. A., Marsden, D., Mauskopf, P., Menanteau, F., Moodley, K., Moseley, H., Netterfield, C. B., Niemack, M. D., Nolta, M. R., Page, L. A., Parker, L., Partridge, B., Reid, B., Sehgal, N., Sherwin, B. D., Sievers, J., Spergel, D. N., Staggs, S. T., Swetz, D. S., Switzer, E. R., Thornton, R., Trac, H., Tucker, C., Warne, R., Wollack, E., Zhao, Y., Oct. 2011. The Atacama Cosmology Telescope: calibration with the Wilkinson Microwave Anisotropy Probe using cross-correlations. Astrophys. J. 740, 86.

Halverson, N. W., Leitch, E. M., Pryke, C., Kovac, J., Carlstrom, J. E., Holzapfel, W. L., Dragovan, M., Cartwright, J. K., Mason, B. S., Padin, S., Pearson, T. J., Readhead, A. C. S., Shepherd, M. C., Mar. 2002. Degree angular scale interferometer first results: a measurement of the cosmic microwave background angular power spectrum. Astrophys. J. 568, 38–45.

Hamilton, A. J. S., Apr. 2001. Formulae for growth factors in expanding universes containing matter and a cosmological constant. Mon. Not. R. Astron. Soc. 322, 419–425.

Hanany, S., Ade, P., Balbi, A., Bock, J., Borrill, J., Boscaleri, A., de Bernardis, P., Ferreira, P. G., Hristov, V. V., Jaffe, A. H., Lange, A. E., Lee, A. T., Mauskopf, P. D., Netterfield, C. B., Oh, S., Pascale, E., Rabii, B., Richards, P. L., Dec. 2000. MAXIMA-1: a measurement of the cosmic microwave background anisotropy on angular scales of 10^{-5} deg. Astrophys. J. Lett. 545, L5–L9.

Hinshaw, G., Larson, D., Komatsu, E., Spergel, D. N., Bennett, C. L., Dunkley, J., Nolta, M. R., Halpern, M., Hill, R. S., Odegard, N., Page, L., Smith, K. M., Weiland, J. L., Gold, B., Jarosik, N., Kogut, A., Limon, M., Meyer, S. S., Tucker, G. S., Wollack, E., Wright, E. L., Oct. 2013. Nine-year Wilkinson Microwave Anisotropy Probe (WMAP) observations: cosmological parameter results. Astrophys. J. Suppl. Ser. 208, 19.

Hirata, C. M., Mar. 2006. Wouthuysen-Field coupling strength and application to high-redshift 21-cm radiation. Mon. Not. R. Astron. Soc. 367, 259–274.

Hirata, C. M., Jul. 2008. Two-photon transitions in primordial hydrogen recombination. Phys. Rev. D 78 (2), 023001.

Hirata, C. M., Forbes, J., Jul. 2009. Lyman-α transfer in primordial hydrogen recombination. Phys. Rev. D 80 (2), 023001.

Hirata, C. M., Padmanabhan, N., Nov. 2006. Cosmological production of H_2 before the formation of the first galaxies. Mon. Not. R. Astron. Soc. 372, 1175–1186.

Hirata, C. M., Sigurdson, K., Mar. 2007. The spin-resolved atomic velocity distribution and 21-cm line profile of dark-age gas. Mon. Not. R. Astron. Soc. 375, 1241–1264.

Hirata, C. M., Switzer, E. R., Apr. 2008. Primordial helium recombination. II. Two-photon processes. Phys. Rev. D 77 (8), 083007.

Hosokawa, T., Omukai, K., Yoshida, N., Yorke, H. W., Dec. 2011. Protostellar feedback halts the growth of the first stars in the universe. Science 334, 1250–1253.

Hutchins, J. B., Apr. 1976. The thermal effects of H_2 molecules in rotating and collapsing spheroidal gas clouds. Astrophys. J. 205, 103–121.

Iliev, I. T., Shapiro, P. R., Ferrara, A., Martel, H., Jun. 2002. On the direct detectability of the cosmic dark ages: 21 centimeter emission from minihalos. Astrophys. J. Lett. 572, L123–L126.

Iliev, I. T., Scannapieco, E., Martel, H., Shapiro, P. R., May 2003. Non-linear clustering during the cosmic Dark Ages and its effect on the 21-cm background from minihaloes. Mon. Not. R. Astron. Soc. 341, 81–90.

Iwata, I., Inoue, A. K., Matsuda, Y., Furusawa, H., Hayashino, T., Kousai, K., Akiyama, M., Yamada, T., Burgarella, D., Deharveng, J.-M., Feb. 2009. Detections of Lyman continuum from star-forming galaxies at $z \sim 3$ through Subaru/Suprime-Cam narrow-band imaging. Astrophys. J. 692, 1287–1293.

Johnson, L. C., May 1972. Approximations for collisional and radiative transition rates in atomic hydrogen. Astrophys. J. 174, 227.

Johnson, J. L., Bromm, V., Feb. 2006. The cooling of shock-compressed primordial gas. Mon. Not. R. Astron. Soc. 366, 247–256.

Jones, B. J. T., Wyse, R. F. G., Aug. 1985. The ionisation of the primeval plasma at the time of recombination. Astron. Astrophys. 149, 144–150.

Karpas, Z., Anicich, V., Huntress, W. T., Mar. 1979. An ion cyclotron resonance study of reactions of ions with hydrogen atoms. J. Chem. Phys. 70, 2877–2881.

Karzas, W. J., Latter, R., May 1961. Electron radiative transitions in a Coulomb field. Astrophys. J. Suppl. Ser. 6, 167–212.

Kholupenko, E. E., Ivanchik, A. V., Dec. 2006. Two-photon $2s \leftrightarrow 1s$ transitions during hydrogen recombination in the universe. Astron. Lett. 32, 795–803.

Kholupenko, E. E., Ivanchik, A. V., Varshalovich, D. A., 2005. CMBR distortion concerned with recombination of the primordial hydrogen plasma. Gravitation Cosmol. 11, 161–165.

Kholupenko, E. E., Ivanchik, A. V., Varshalovich, D. A., Jun. 2007. Rapid He II $\rightarrow$ He I recombination and radiation arising from this process. Mon. Not. R. Astron. Soc. 378, L39–L43.

Kholupenko, E. E., Ivanchik, A. V., Varshalovich, D. A., Apr. 2010. Effect of radiative feedbacks for resonant transitions during cosmological recombination. Phys. Rev. D 81 (8), 083004.

Kogut, A., Fixsen, D. J., Chuss, D. T., Dotson, J., Dwek, E., Halpern, M., Hinshaw, G. F., Meyer, S. M., Moseley, S. H., Seiffert, M. D., Spergel, D. N., Wollack, E. J., Jul. 2011. The Primordial Inflation Explorer (PIXIE): a nulling polarimeter for cosmic microwave background observations. J. Cosmol. Astropart. Phys. 7, 25.

Komatsu, E., Smith, K. M., Dunkley, J., Bennett, C. L., Gold, B., Hinshaw, G., Jarosik, N., Larson, D., Nolta, M. R., Page, L., Spergel, D. N., Halpern, M., Hill, R. S., Kogut, A., Limon, M., Meyer, S. S., Odegard, N., Tucker, G. S., Weiland, J. L., Wollack, E., Wright, E. L., Feb. 2011. Seven-year Wilkinson Microwave Anisotropy Probe (WMAP) observations: cosmological interpretation. Astrophys. J. Suppl. Ser. 192, 18.

Kreckel, H., Bruhns, H., Čížek, M., Glover, S. C. O., Miller, K. A., Urbain, X., Savin, D. W., Jul. 2010. Experimental results for H_2 formation from H^- and H and implications for first star formation. Science 329, 69–71.

Kuhlen, M., Madau, P., Montgomery, R., Jan. 2006. The spin temperature and 21 cm brightness of the intergalactic medium in the pre-reionization era. Astrophys. J. Lett. 637, L1–L4.

Labzowsky, L. N., Shonin, A. V., Solovyev, D. A., Feb. 2005. QED calculation of E1M1 and E1E2 transition probabilities in one-electron ions with arbitrary nuclear charge. J. Phys. B 38, 265–278.

Leitherer, C., Schaerer, D., Goldader, J. D., González Delgado, R. M., Robert, C., Kune, D. F., de Mello, D. F., Devost, D., Heckman, T. M., Jul. 1999. Starburst99: synthesis models for galaxies with active star formation. Astrophys. J. Suppl. Ser. 123, 3–40.

Lepp, S., Shull, J. M., May 1984. Molecules in the early universe. Astrophys. J. 280, 465–469.

Lepp, S., Stancil, P. C., Dalgarno, A., May 2002. Atomic and molecular processes in the early Universe. J. Phys. B 35, 57–80.

Lewis, A., Challinor, A., Lasenby, A., Aug. 2000. Efficient computation of cosmic microwave background anisotropies in closed Friedmann-Robertson-Walker models. Astrophys. J. 538, 473–476.

Lewis, A., Weller, J., Battye, R., Dec. 2006. The cosmic microwave background and the ionization history of the universe. Mon. Not. R. Astron. Soc. 373, 561–570.

Liszt, H., May 2001. The spin temperature of warm interstellar H I. Astron. Astrophys. 371, 698–707.

Loeb, A., Jul. 2001. Probing the universe after cosmological recombination through the effect of neutral lithium on the microwave background anisotropies. Astrophys. J. Lett. 555, L1–L5.

Loeb, A., Furlanetto, S. R., 2013. The First Galaxies in the Universe. Princeton University Press, Princeton.

Loeb, A., Zaldarriaga, M., May 2004. Measuring the small-scale power spectrum of cosmic density fluctuations through 21cm tomography prior to the epoch of structure formation. Phys. Rev. Lett. 92 (21), 211301.

Lueker, M., Reichardt, C. L., Schaffer, K. K., Zahn, O., Ade, P. A. R., Aird, K. A., Benson, B. A., Bleem, L. E., Carlstrom, J. E., Chang, C. L., Cho, H., Crawford, T. M., Crites, A. T., de Haan, T., Dobbs, M. A., George, E. M., Hall, Aug. 2010. Measurements of secondary cosmic microwave background anisotropies with the South Pole Telescope. Astrophys. J. 719, 1045–1066.

Lyubarsky, Y. E., Sunyaev, R. A., Jul. 1983. The spectral features in the microwave background spectrum due to energy release in the early universe. Astron. Astrophys. 123, 171–183.

Mack, K. J., Wesley, D. H., May 2008. Primordial black holes in the Dark Ages: observational prospects for future 21cm surveys. ArXiv e-prints 0805.1531.

Madau, P., Meiksin, A., Rees, M. J., Feb. 1997. 21 Centimeter tomography of the intergalactic medium at high redshift. Astrophys. J. 475, 429–444.

Mao, Y., Shapiro, P. R., Mellema, G., Iliev, I. T., Koda, J., Ahn, K., May 2012. Redshift-space distortion of the 21-cm background from the epoch of reionization—I. Methodology re-examined. Mon. Not. R. Astron. Soc. 422, 926–954.

Mashonkina, L. J., 1996. Accurate collisional cross sections: important input data in non-LTE calculations. In: Adelman, S. J., Kupka, F., Weiss, W. W. (Eds.), Model Atmospheres and Spectrum Synthesis. Astronomical Society of the Pacific, Provo, pp. 140–153.

Matsumura, T., Akiba, Y., Borrill, J., Chinone, Y., Dobbs, M., Fuke, H., Ghribi, A., Hasegawa, M., Hattori, K., Hattori, M., Hazumi, M., Holzapfel, W., Inoue, Y., Ishidoshiro, K., Ishino, H., Ishitsuka, H., Karatsu, K., Katayama, N., Kawano, I., Kibayashi, A., Kibe, Y., Kimura, K., Kimura, N., Koga, K., Kozu, M., Komatsu, E., Lee, A., Matsuhara, H., Mima, S., Mitsuda, K., Mizukami, K., Morii, H., Morishima, T., Murayama, S., Nagai, M., Nagata, R., Nakamura, S., Naruse, M., Natsume, K., Nishibori, T., Nishino, H., Noda, A., Noguchi, T., Ogawa, H., Oguri, S., Ohta, I., Otani, C., Richards, P., Sakai, S., Sato, N., Sato, Y., Sekimoto, Y., Shimizu, A., Shinozaki, K., Sugita, H., Suzuki, T., Suzuki, A., Tajima, O., Takada, S., Takakura, S., Takei, Y., Tomaru, T., Uzawa, Y., Wada, T., Watanabe, H., Yamasaki, N., Yoshida, M., Yoshida, T., Yotsumoto, K., Nov. 2013. Mission design of LiteBIRD. ArXiv e-prints 1311.2847.

Mayer, M., Duschl, W. J., Jan. 2005. Stationary population III accretion discs. Mon. Not. R. Astron. Soc. 356, 1–11.

McGreer, I. D., Bryan, G. L., Sep. 2008. The impact of HD cooling on the formation of the first stars. Astrophys. J. 685, 8–20.

McKee, C. F., Tan, J. C., Jul. 2008. The formation of the first stars. II. Radiative feedback processes and implications for the initial mass function. Astrophys. J. 681, 771–797.

McLure, R. J., Dunlop, J. S., de Ravel, L., Cirasuolo, M., Ellis, R. S., Schenker, M., Robertson, B. E., Koekemoer, A. M., Stark, D. P., Bowler, R. A. A., Dec. 2011. A robust sample of galaxies at redshifts $6.0 < z < 8.7$: stellar populations, star formation rates and stellar masses. Mon. Not. R. Astron. Soc. 418, 2074–2105.

McMahon, J. J., Aird, K. A., Benson, B. A., Bleem, L. E., Britton, J., Carlstrom, J. E., Chang, C. L., Cho, H. S., de Haan, T., Crawford, T. M., Crites, A. T., Datesman, A., Dobbs, M. A., Everett, W., Halverson, N. W., Holder, G. P., Holzapfel, W. L., Hrubes, D., Irwin, K. D., Joy, M., Keisler, R., Lanting, T. M., Lee, A. T., Leitch, E. M., Loehr, A., Lueker, M., Mehl, J., Meyer, S. S., Mohr, J. J., Montroy, T. E., Niemack, M. D., Ngeow, C. C., Novosad, V., Padin, S., Plagge, T., Pryke, C., Reichardt, C., Ruhl, J. E., Schaffer, K. K., Shaw, L., Shirokoff, E., Spieler, H. G., Stadler, B., Stark, A. A., Staniszewski, Z., Vanderlinde, K., Vieira, J. D., Wang, G., Williamson, R., Yefremenko, V., Yoon, K. W., Zhan, O., Zenteno, A., Dec. 2009. SPTpol: an instrument for CMB polarization. In: Young, B., Cabrera, B., Miller, A. (Eds.), The Thirteenth International Workshop on Low Temperature Detectors—LTD13. American Institute of Physics, Melville, pp. 511–514.

McQuinn, M., Switzer, E. R., Sep. 2009. Redshifted intergalactic $^3He^+$ 8.7 GHz hyperfine absorption. Phys. Rev. D 80 (6), 063010.

McQuinn, M., Lidz, A., Zahn, O., Dutta, S., Hernquist, L., Zaldarriaga, M., May 2007. The morphology of H ɪɪ regions during reionization. Mon. Not. R. Astron. Soc. 377, 1043–1063.

McQuinn, M., Lidz, A., Zaldarriaga, M., Hernquist, L., Hopkins, P. F., Dutta, S., Faucher-Giguère, C.-A., Apr. 2009. He ɪɪ reionization and its effect on the intergalactic medium. Astrophys. J. 694, 842–866.

Mellema, G., Iliev, I. T., Pen, U.-L., Shapiro, P. R., Oct. 2006. Simulating cosmic reionization at large scales—II. The 21-cm emission features and statistical signals. Mon. Not. R. Astron. Soc. 372, 679–692.

Mesinger, A., Sep. 2010. Was reionization complete by $z \, 5 - 6$? Mon. Not. R. Astron. Soc. 407, 1328–1337.

Miller, S., Achilleos, N., Ballester, G. E., Geballe, T. R., Joseph, R. D., Prangé, R., Rego, D., Stallard, T., Tennyson, J., Trafton, L. M., Waite, Jr., J. H., 2000. The role of H_3^+ in planetary atmospheres. Philos. Trans. R. Soc. Lond. Ser. A 358, 2485–2502.

Miralda-Escudé, J., Nov. 2003. On the evolution of the ionizing emissivity of galaxies and quasars required by the hydrogen reionization. Astrophys. J. 597, 66–73.

Miyake, S., Stancil, P. C., Sadeghpour, H. R., Dalgarno, A., McLaughlin, B. M., Forrey, R. C., Feb. 2010. Resonant H^- photodetachment: enhanced photodestruction and consequences for radiative feedback. Astrophys. J. Lett. 709, L168–L171.

Mizusawa, H., Omukai, K., Nishi, R., Dec. 2005. Primordial molecular emission in population III galaxies. Publ. Astron. Soc. Japan 57, 951–967.

Morales, M. F., Wyithe, J. S. B., Sep. 2010. Reionization and cosmology with 21-cm fluctuations. Annu. Rev. Astron. Astrophys. 48, 127–171.

Nagakura, T., Omukai, K., Dec. 2005. Formation of population III stars in fossil H ii regions: significance of HD. Mon. Not. R. Astron. Soc. 364, 1378–1386.

Nakamura, F., Umemura, M., Apr. 2002. The stellar initial mass function in primordial galaxies. Astrophys. J. 569, 549–557.

Naoz, S., Barkana, R., Sep. 2005. Growth of linear perturbations before the era of the first galaxies. Mon. Not. R. Astron. Soc. 362, 1047–1053.

Naoz, S., Barkana, R., Mar. 2008. Detecting early galaxies through their 21-cm signature. Mon. Not. R. Astron. Soc. 385, L63–L67.

Nestor, D. B., Shapley, A. E., Steidel, C. C., Siana, B., Jul. 2011. Narrowband imaging of escaping Lyman-continuum emission in the SSA22 field. Astrophys. J. 736, 18.

Netterfield, C. B., Ade, P. A. R., Bock, J. J., Bond, J. R., Borrill, J., Boscaleri, A., Coble, K., Contaldi, C. R., Crill, B. P., de Bernardis, P., Farese, P., Ganga, K., Giacometti, M., Hivon, E., Hristov, V. V., Iacoangeli, A., Jaffe, A. H., Jun. 2002. A measurement by BOOMERANG of multiple peaks in the angular power spectrum of the cosmic microwave background. Astrophys. J. 571, 604–614.

Niemack, M. D., Ade, P. A. R., Aguirre, J., Barrientos, F., Beall, J. A., Bond, J. R., Britton, J., Cho, H. M., Das, S., Devlin, M. J., Dicker, S., Dunkley, J., Dünner, R., Fowler, J. W., Hajian, A., Halpern, M., Hasselfield, M., Hilton, G. C., Hilton, M., Hubmayr, J., Hughes, J. P., Infante, L., Irwin, K. D., Jarosik, N., Klein, J., Kosowsky, A., Marriage, T. A., McMahon, J., Menanteau, F., Moodley, K., Nibarger, J. P., Nolta, M. R., Page, L. A., Partridge, B., Reese, E. D., Sievers, J., Spergel, D. N., Staggs, S. T., Thornton, R., Tucker, C., Wollack, E., Yoon, K. W., Jul. 2010. ACTPol: a polarization-sensitive receiver for the Atacama Cosmology Telescope. Proc. SPIE 7741, 77411S.

Oh, S. P., Jun. 2001. Reionization by hard photons. I. X-rays from the first star clusters. Astrophys. J. 553, 499–512.

Olive, K. A., Steigman, G., Walker, T. P., Aug. 2000. Primordial nucleosynthesis: theory and observations. Phys. Rep. 333, 389–407.

Omukai, K., Nishi, R., Nov. 1998. Formation of primordial protostars. Astrophys. J. 508, 141–150.

Omukai, K., Palla, F., Jun. 2003. Formation of the first stars by accretion. Astrophys. J. 589, 677–687.

Omukai, K., Nishi, R., Uehara, H., Susa, H., May 1998. Evolution of primordial protostellar clouds—quasi-static analysis. Prog. Theo. Phys 99, 747–761.

Opal, C. B., Peterson, W. K., Beaty, E. C., Oct. 1971. Measurements of secondary-electron spectra produced by electron impact ionization of a number of simple gases. J. Chem. Phys. 55, 4100–4106.

O'Shea, B. W., Norman, M. L., Jan. 2007. Population III star formation in a ΛCDM universe. I. The effect of formation redshift and environment on protostellar accretion rate. Astrophys. J. 654, 66–92.

Padmanabhan, N., Finkbeiner, D. P., Jul. 2005. Detecting dark matter annihilation with CMB polarization: signatures and experimental prospects. Phys. Rev. D 72 (2), 023508.

Page, L., Nolta, M. R., Barnes, C., Bennett, C. L., Halpern, M., Hinshaw, G., Jarosik, N., Kogut, A., Limon, M., Meyer, S. S., Peiris, H. V., Spergel, D. N., Tucker, G. S., Wollack, E., Wright, E. L., Sep. 2003. First-year Wilkinson Microwave Anisotropy Probe (WMAP) observations: interpretation of the TT and TE angular power spectrum peaks. Astrophys. J. Suppl. Ser. 148, 233–241.

Palla, F., Salpeter, E. E., Stahler, S. W., Aug. 1983. Primordial star formation—the role of molecular hydrogen. Astrophys. J. 271, 632–641.

Pawlik, A. H., Schaye, J., van Scherpenzeel, E., Apr. 2009. Keeping the universe ionized: photoheating and the clumping factor of the high-redshift intergalactic medium. Mon. Not. R. Astron. Soc. 394, 1812–1824.

Peacock, J. A., Jan. 1999. Cosmological physics.

Pearson, T. J., Mason, B. S., Readhead, A. C. S., Shepherd, M. C., Sievers, J. L., Udomprasert, P. S., Cartwright, J. K., Farmer, A. J., Padin, S., Myers, S. T., Bond, J. R., Contaldi, C. R., Pen, U.-L., Jul. 2003. The anisotropy of the microwave background to $l = 3500$: mosaic observations with the cosmic background imager. Astrophys. J. 591, 556–574.

Peebles, P. J. E., Jul. 1968. Recombination of the primeval plasma. Astrophys. J. 153, 1–11.

Peebles, P. J. E., Yu, J. T., Dec. 1970. Primeval adiabatic perturbation in an expanding universe. Astrophys. J. 162, 815–836.

Peebles, P. J. E., Seager, S., Hu, W., Aug. 2000. Delayed recombination. Astrophys. J. Lett. 539, L1–L4.

Planck Collaboration, Ade, P. A. R., Aghanim, N., Armitage-Caplan, C., Arnaud, M., Ashdown, M., Atrio-Barandela, F., Aumont, J., Baccigalupi, C., Banday, A. J., et al., Mar. 2013. Planck 2013 results. XVI. Cosmological parameters. ArXiv e-prints 1303.5076.

Porter, R. L., Ferland, G. J., MacAdam, K. B., Storey, P. J., Feb. 2009. Uncertainties in theoretical HeI emissivities: HII regions, primordial abundance and cosmological recombination. Mon. Not. R. Astron. Soc. 393, L36–L40.

Pospelov, M., Pradler, J., Nov. 2010. Big Bang nucleosynthesis as a probe of new physics. Annu. Rev. Nucl. Part. Sci. 60, 539–568.

Press, W. H., Schechter, P., Feb. 1974. Formation of galaxies and clusters of galaxies by self-similar gravitational condensation. Astrophys. J. 187, 425–438.

Pritchard, J. R., Furlanetto, S. R., Apr. 2006. Descending from on high: Lyman-series cascades and spin-kinetic temperature coupling in the 21-cm line. Mon. Not. R. Astron. Soc. 367, 1057–1066.

Pritchard, J. R., Furlanetto, S. R., Apr. 2007. 21-cm fluctuations from inhomogeneous X-ray heating before reionization. Mon. Not. R. Astron. Soc. 376, 1680–1694.

Pritchard, J. R., Loeb, A., Nov. 2008. Evolution of the 21cm signal throughout cosmic history. Phys. Rev. D 78 (10), 103511.

Pritchard, J., Loeb, A., Dec. 2010. Cosmology: hydrogen was not ionized abruptly. Nature 468, 772–773.

Pritchard, J. R., Loeb, A., Aug. 2012. 21 cm cosmology in the 21st century. Rep. Prog. Phys. 75 (8), 086901.

Puy, D., Alecian, G., Le Bourlot, J., Leorat, J., Pineau Des Forets, G., Jan. 1993. Formation of primordial molecules and thermal balance in the early universe. Astron. Astrophys. 267, 337–346.

QUIET Collaboration, Bischoff, C., Brizius, A., Buder, I., Chinone, Y., Cleary, K., Dumoulin, R. N., Kusaka, A., Monsalve, R., Nss, S. K., Newburgh, L. B., Reeves, R., Smith, K. M., Wehus, I. K., Zuntz, J. A., Zwart, J. T. L., Bronfman, L., Bustos, R., Church, S. E., Dickinson, C., Eriksen, H. K., Ferreira, P. G., Gaier, T., Gundersen, J. O.,

Hasegawa, M., Hazumi, M., Huffenberger, K. M., Jones, M. E., Kangaslahti, P., Kapner, D. J., Lawrence, C. R., Limon, M., May, J., McMahon, J. J., Miller, A. D., Nguyen, H., Nixon, G. W., Pearson, T. J., Piccirillo, L., Radford, S. J. E., Readhead, A. C. S., Richards, J. L., Samtleben, D., Seiffert, M., Shepherd, M. C., Staggs, S. T., Tajima, O., Thompson, K. L., Vanderlinde, K., Williamson, R., Winstein, B., Nov. 2011. First season QUIET observations: measurements of cosmic microwave background polarization power spectra at 43 GHz in the multipole range $25 \leq \ell \leq 475$. Astrophys. J. 741, 111.

Reed, D. S., Bower, R., Frenk, C. S., Jenkins, A., Theuns, T., Jan. 2007. The halo mass function from the dark ages through the present day. Mon. Not. R. Astron. Soc. 374, 2–15.

Ricotti, M., Ostriker, J. P., Mack, K. J., Jun. 2008. Effect of primordial black holes on the cosmic microwave background and cosmological parameter estimates. Astrophys. J. 680, 829–845.

Ripamonti, E., Abel, T., Mar. 2004. Fragmentation and the formation of primordial protostars: the possible role of collision-induced emission. Mon. Not. R. Astron. Soc. 348, 1019–1034.

Ripamonti, E., Haardt, F., Ferrara, A., Colpi, M., Aug. 2002. Radiation from the first forming stars. Mon. Not. R. Astron. Soc. 334, 401–418.

Rubiño-Martin, J. A., Rebolo, R., Carreira, P., Cleary, K., Davies, R. D., Davis, R. J., Dickinson, C., Grainge, K., Gutiérrez, C. M., Hobson, M. P., Jones, M. E., Kneissl, R., Lasenby, A., Maisinger, K., Jun. 2003. First results from the Very Small Array—IV. Cosmological parameter estimation. Mon. Not. R. Astron. Soc. 341, 1084–1092.

Rubiño-Martín, J. A., Chluba, J., Sunyaev, R. A., Oct. 2006. Lines in the cosmic microwave background spectrum from the epoch of cosmological hydrogen recombination. Mon. Not. R. Astron. Soc. 371, 1939–1952.

Rubiño-Martín, J. A., Chluba, J., Sunyaev, R. A., Jul. 2008. Lines in the cosmic microwave background spectrum from the epoch of cosmological helium recombination. Astron. Astrophys. 485, 377–393.

Rubiño-Martín, J. A., Chluba, J., Fendt, W. A., Wandelt, B. D., Mar. 2010. Estimating the impact of recombination uncertainties on the cosmological parameter constraints from cosmic microwave background experiments. Mon. Not. R. Astron. Soc. 403, 439–452.

Rybicki, G. B., Aug. 2006. Improved Fokker-Planck equation for resonance-line scattering. Astrophys. J. 647, 709–718.

Ryden, B., 2003. Introduction to cosmology.

Santos, M. G., Amblard, A., Pritchard, J., Trac, H., Cen, R., Cooray, A., Dec. 2008. Cosmic reionization and the 21 cm signal: comparison between an analytical model and a simulation. Astrophys. J. 689, 1–16.

Schaerer, D., Jan. 2002. On the properties of massive population III stars and metal-free stellar populations. Astron. Astrophys. 382, 28–42.

Seager, S., Sasselov, D. D., Scott, D., Sep. 1999. A new calculation of the recombination epoch. Astrophys. J. Lett. 523, L1–L5.

Seager, S., Sasselov, D. D., Scott, D., Jun. 2000. How exactly did the universe become neutral? Astrophys. J. Suppl. Ser. 128, 407–430.

Seaton, M. J., Zeippen, C. J., Tully, J. A., Pradhan, A. K., Mendoza, C., Hibbert, A., Berrington, K. A., Mar. 1992. The opacity project—computation of atomic data. Rev. Mexicana Astron. Astrof. 23, 19.

Seljak, U., Zaldarriaga, M., Oct. 1996. A line-of-sight integration approach to cosmic microwave background anisotropies. Astrophys. J. 469, 437.

Semelin, B., Combes, F., Baek, S., Nov. 2007. Lyman-alpha radiative transfer during the epoch of reionization: contribution to 21-cm signal fluctuations. Astron. Astrophys. 474, 365–374.

Shapiro, P. R., Giroux, M. L., Oct. 1987. Cosmological H II regions and the photoionization of the intergalactic medium. Astrophys. J. Lett. 321, L107–L112.

Shapiro, P. R., Iliev, I. T., Raga, A. C., Mar. 2004. Photoevaporation of cosmological minihaloes during reionization. Mon. Not. R. Astron. Soc. 348, 753–782.

Shapiro, P. R., Ahn, K., Alvarez, M. A., Iliev, I. T., Martel, H., Ryu, D., Aug. 2006. The 21 cm background from the cosmic dark ages: minihalos and the intergalactic medium before reionization. Astrophys. J. 646, 681–690.

Shapley, A. E., Steidel, C. C., Pettini, M., Adelberger, K. L., Erb, D. K., Nov. 2006. The direct detection of Lyman continuum emission from star-forming galaxies at $z \sim 3$. Astrophys. J. 651, 688–703.

Shaw, J. R., Chluba, J., Aug. 2011. Precise cosmological parameter estimation using COSMOREC. Mon. Not. R. Astron. Soc. 415, 1343–1354.

Shaw, J. R., Lewis, A., Nov. 2008. Nonlinear redshift-space power spectra. Phys. Rev. D 78 (10), 103512.

Sheth, R. K., Tormen, G., Jan. 2002. An excursion set model of hierarchical clustering: ellipsoidal collapse and the moving barrier. Mon. Not. R. Astron. Soc. 329, 61–75.

Shull, J. M., van Steenberg, M. E., Nov. 1985. X-ray secondary heating and ionization in quasar emission-line clouds. Astrophys. J. 298, 268–274.

Sigurdson, K., Furlanetto, S. R., Sep. 2006. Measuring the primordial deuterium abundance during the cosmic dark ages. Phys. Rev. Lett. 97 (9), 091301.

Slatyer, T. R., Padmanabhan, N., Finkbeiner, D. P., Aug. 2009. CMB constraints on WIMP annihilation: energy absorption during the recombination epoch. Phys. Rev. D 80 (4), 043526.

Smith, R. J., Glover, S. C. O., Clark, P. C., Greif, T., Klessen, R. S., Jul. 2011. The effects of accretion luminosity upon fragmentation in the early universe. Mon. Not. R. Astron. Soc. 414, 3633–3644.

Smoot, G. F., Bennett, C. L., Kogut, A., Wright, E. L., Aymon, J., Boggess, N. W., Cheng, E. S., de Amici, G., Gulkis, S., Hauser, M. G., Hinshaw, G., Jackson, P. D., Janssen, M., Kaita, E., Kelsall, T., Keegstra, P., Sep. 1992. Structure in the COBE differential microwave radiometer first-year maps. Astrophys. J. Lett. 396, L1–L5.

Sobolev, V. V., 1960. Moving Envelopes of Stars. Harvard University Press, Cambridge.

Sofue, Y., Rubin, V., 2001. Rotation curves of spiral galaxies. Annu. Rev. Astron. Astrophys. 39, 137–174.

Spitzer, Jr., L., Greenstein, J. L., Nov. 1951. Continuous emission from planetary nebulae. Astrophys. J. 114, 407.

Stacy, A., Greif, T. H., Bromm, V., Mar. 2010. The first stars: formation of binaries and small multiple systems. Mon. Not. R. Astron. Soc. 403, 45–60.

Stacy, A., Greif, T. H., Bromm, V., May 2012. The first stars: mass growth under protostellar feedback. Mon. Not. R. Astron. Soc. 422, 290–309.

Stahler, S. W., Palla, F., Salpeter, E. E., Mar. 1986. Primordial stellar evolution—the protostar phase. Astrophys. J. 302, 590–605.

Stancil, P. C., Dalgarno, A., Apr. 1997a. Stimulated radiative association of Li and H in the early universe. Astrophys. J. 479, 543–546.

Stancil, P. C., Dalgarno, A., Nov. 1997b. The radiative association of H and D. Astrophys. J. 490, 76–78.

Stancil, P., Dalgarno, A., 1998. Chemical processes in astrophysical radiation fields. Faraday Discuss. 109, 61–69.

Stancil, P. C., Lepp, S., Dalgarno, A., Feb. 1996. The lithium chemistry of the early universe. Astrophys. J. 458, 401–406.

Stancil, P. C., Lepp, S., Dalgarno, A., Dec. 1998. The deuterium chemistry of the early universe. Astrophys. J. 509, 1–10.

Stancil, P. C., Loeb, A., Zaldarriaga, M., Dalgarno, A., Lepp, S., Nov. 2002. Cosmological recombination of lithium and its effect on the microwave background anisotropies. Astrophys. J. 580, 29–35.

Storey, P. J., Hummer, D. G., Jul. 1991. Fast computer evaluation of radiative properties of hydrogenic systems. Comput. Phys. Commun. 66, 129–141.

Sunyaev, R. A., Chluba, J., 2009. Signals from the epoch of cosmological recombination. Astron. Nachr. 330, 657–674.

Sunyaev, R. A., Zeldovich, Y. B., 1970a. Small-scale fluctuations of relic radiation. Astrophys. Space Sci. 7, 3–19.

Sunyaev, R. A., Zeldovich, Y. B., Apr. 1970b. The interaction of matter and radiation in the hot model of the universe, II. Astrophys. Space Sci. 7, 20–30.

Switzer, E. R., Hirata, C. M., Oct. 2005. Ionizing radiation from hydrogen recombination strongly suppresses the lithium scattering signature in the CMB. Phys. Rev. D 72 (8), 083002.

Switzer, E. R., Hirata, C. M., Apr. 2008a. Primordial helium recombination. I. Feedback, line transfer, and continuum opacity. Phys. Rev. D 77 (8), 083006.

Switzer, E. R., Hirata, C. M., Apr. 2008b. Primordial helium recombination. III. Thomson scattering, isotope shifts, and cumulative results. Phys. Rev. D 77 (8), 083008.

Tan, J. C., Blackman, E. G., Mar. 2004. Protostellar disk dynamos and hydromagnetic outflows in primordial star formation. Astrophys. J. 603, 401–413.

Tan, J. C., McKee, C. F., Mar. 2004. The formation of the first stars. I. Mass infall rates, accretion disk structure, and protostellar evolution. Astrophys. J. 603, 383–400.

Tegmark, M., Silk, J., Rees, M. J., Blanchard, A., Abel, T., Palla, F., Jan. 1997. How small were the first cosmological objects? Astrophys. J. 474, 1.

The Planck Collaboration, Apr. 2006. The scientific programme of Planck. ArXiv e-prints astro-ph/0604069.

The Polarbear Collaboration, Errard, J., Ade, P. A. R., Anthony, A., Arnold, K., Aubin, F., Boettger, D., Borrill, J., Cantalupo, C., Dobbs, M. A., Flanigan, D., Ghribi, A., Halverson, N., Hazumi, M., Holzapfel, W. L., Howard, J., Hyland, P., Jaffe, A., Keating, B., Kisner, T., Kermish, Z., Lee, A. T., Linder, E., Lungu, M., Matsumura, T., Miller, N., Meng, X., Myers, M., Nishino, H., O'Brient, R., O'Dea, D., Reichardt, C., Schanning, I., Shimizu, A., Shimmin, C., Shimon, M., Spieler, H., Steinbach, B., Stompor, R., Suzuki, A., Tomaru, T., Tran, H. T., Tucker, C., Quealy, E., Richards, P. L., Zahn, O., Nov. 2010. The new generation CMB B-mode polarization experiment: POLARBEAR. ArXiv e-prints 1011.0763.

Tseliakhovich, D., Hirata, C., Oct. 2010. Relative velocity of dark matter and baryonic fluids and the formation of the first structures. Phys. Rev. D 82 (8), 083520.

Tseliakhovich, D., Barkana, R., Hirata, C., Dec. 2011. Suppression and spatial variation of early galaxies and minihalos. Mon. Not. R. Astron. Soc. 418, 906–915.

Turk, M. J., Abel, T., O'Shea, B., Jul. 2009. The formation of population III binaries from cosmological initial conditions. Science 325, 601–605.

Turk, M. J., Clark, P., Glover, S. C. O., Greif, T. H., Abel, T., Klessen, R., Bromm, V., Jan. 2011. Effects of varying the three-body molecular hydrogen formation rate in primordial star formation. Astrophys. J. 726, 55.

Valdés, M., Ferrara, A., Jun. 2008. The energy cascade from warm dark matter decays. Mon. Not. R. Astron. Soc. 387, L8–L12.

Valdés, M., Ferrara, A., Mapelli, M., Ripamonti, E., May 2007. Constraining dark matter through 21-cm observations. Mon. Not. R. Astron. Soc. 377, 245–252.

van de Hulst, H., 1945. Radiogolven uit het Wereldruim (Radio waves from space). Ned. Tijdschr. Natuurk. 11, 210–221.

Vanderlinde, K., Crawford, T. M., de Haan, T., Dudley, J. P., Shaw, L., Ade, P. A. R., Aird, K. A., Benson, B. A., Bleem, L. E., Brodwin, M., Carlstrom, J. E., Chang, C. L.,

Crites, A. T., Desai, S., Dobbs, M. A., Foley, R. J., George, E. M., Gladders, M. D., Oct. 2010. Galaxy clusters selected with the Sunyaev–Zel'dovich effect from 2008 South Pole Telescope observations. Astrophys. J. 722, 1180–1196.

Venkatesan, A., Giroux, M. L., Shull, J. M., Dec. 2001. Heating and ionization of the intergalactic medium by an early X-ray background. Astrophys. J. 563, 1–8.

Verner, D. A., Ferland, G. J., Apr. 1996. Atomic data for astrophysics. I. Radiative recombination rates for H-like, He-like, Li-like, and Na-like ions over a broad range of temperature. Astrophys. J. Suppl. Ser. 103, 467–473.

Verner, D. A., Ferland, G. J., Korista, K. T., Yakovlev, D. G., Jul. 1996. Atomic data for astrophysics. II. New analytic fits for photoionization cross sections of atoms and ions. Astrophys. J. 465, 487–498.

Vrinceanu, D., Onofrio, R., Sadeghpour, H. R., Mar. 2012. Angular momentum changing transitions in proton–Rydberg hydrogen atom collisions. Astrophys. J. 747, 56.

Walker, T. P., Steigman, G., Kang, H.-S., Schramm, D. M., Olive, K. A., Jul. 1991. Primordial nucleosynthesis redux. Astrophys. J. 376, 51–69.

Wang, X., Hu, W., Jun. 2006. Redshift space 21 cm power spectra from reionization. Astrophys. J. 643, 585–597.

Whalen, D., Abel, T., Norman, M. L., Jul. 2004. Radiation hydrodynamic evolution of primordial H II regions. Astrophys. J. 610, 14–22.

Willott, C. J., Delorme, P., Reylé, C., Albert, L., Bergeron, J., Crampton, D., Delfosse, X., Forveille, T., Hutchings, J. B., McLure, R. J., Omont, A., Schade, D., Mar. 2010. The Canada-France high-z quasar survey: nine new quasars and the luminosity function at redshift 6. Astron. J. 139, 906–918.

Wong, W. Y., Scott, D., Mar. 2007. The effect of forbidden transitions on cosmological hydrogen and helium recombination. Mon. Not. R. Astron. Soc. 375, 1441–1448.

Wouthuysen, S. A., 1952. On the excitation mechanism of the 21-cm (radio–frequency) interstellar hydrogen emission line. Astron. J. 57, 31–32.

Xu, Y., McCray, R., Jul. 1991. Energy degradation of fast electrons in hydrogen gas. Astrophys. J. 375, 190–201.

Yoshida, N., Omukai, K., Hernquist, L., Abel, T., Nov. 2006. Formation of primordial stars in a ΛCDM universe. Astrophys. J. 652, 6–25.

Yoshida, N., Oh, S. P., Kitayama, T., Hernquist, L., Jul. 2007. Early cosmological H II/He III regions and their impact on second-generation star formation. Astrophys. J. 663, 687–707.

Yoshida, N., Omukai, K., Hernquist, L., Aug. 2008. Protostar formation in the early universe. Science 321, 669–671.

Zahn, O., Lidz, A., McQuinn, M., Dutta, S., Hernquist, L., Zaldarriaga, M., Furlanetto, S. R., Jan. 2007. Simulations and analytic calculations of bubble growth during hydrogen reionization. Astrophys. J. 654, 12–26.

Zahn, O., Mesinger, A., McQuinn, M., Trac, H., Cen, R., Hernquist, L. E., Jun. 2011. Comparison of reionization models: radiative transfer simulations and approximate, seminumeric models. Mon. Not. R. Astron. Soc. 414, 727–738.

Zaldarriaga, M., Loeb, A., Jan. 2002. The imprint of lithium recombination on the microwave background anisotropies. Astrophys. J. 564, 52–59.

Zaroubi, S., Thomas, R. M., Sugiyama, N., Silk, J., Mar. 2007. Heating of the intergalactic medium by primordial miniquasars. Mon. Not. R. Astron. Soc. 375, 1269–1279.

Zeldovich, Y. B., Kurt, V. G., Syunyaev, R. A., Jul. 1968. Recombination of hydrogen in the hot model of the universe. Zh. Eksp. Teor. Fiz. 55, 278–286, [Sov. Phys. JETP 28, 146–150 (1969)].

Zemke, W. T., Stwalley, W. C., Dec. 1980. Radiative transition probabilities, lifetimes, and dipole moments for all vibrational levels in the $X^1\Sigma^+$ state of ^{7}LiH. J. Chem. Phys. 73, 5584–5590.

Zwicky, F., 1933. Die Rotverschiebung von extragalaktischen Nebeln. Helv. Phys. Acta 6, 110–127.

Zwicky, F., Oct. 1937. On the masses of nebulae and of clusters of nebulae. Astrophys. J. 86, 217.

Zygelman, B., Apr. 2005. Hyperfine level-changing collisions of hydrogen atoms and tomography of the dark age universe. Astrophys. J. 622, 1356–1362.

Zygelman, B., Stancil, P. C., Dalgarno, A., Nov. 1998. Stimulated radiative association of He and H^+. Astrophys. J. 508, 151–156.